TWO-PARTICLE CORRELATIONS AT SMALL RELATIVE MOMENTA, MEASURED FOR THE REACTIONS ^{14}N+Au AT E/A=35 MeV AND ^{16}O+Au AT E/A=94 MeV

By

Ziping Chen

A DISSERTATION

Submitted to

Michigan State University

in partial fulfillment of the requirements

for the degree of

DOCTOR OF PHILOSOPHY

Department of Physics and Astronomy

1988

To My Mother

Mao-Hua Wang

ABSTRACT

TWO-PARTICLE CORRELATIONS AT SMALL RELATIVE MOMENTA, MEASURED FOR THE REACTIONS ^{14}N+Au AT E/A=35 MeV AND ^{16}O+Au AT E/A=94 MeV

BY

Ziping Chen

Single- and two-particle inclusive cross sections for light nuclei (p, d, t, ^{3,4}He, $^{6\text{-}9}$Li, ^{7,8,10}Be) were measured for the reactions ^{14}N + ^{197}Au at E/A=35 MeV and ^{16}O + ^{197}Au at E/A=94 MeV. Two-particle correlation functions support the picture of formation and decay of a localized subsystem of high excitation. Kinetic temperature parameters, τ, extracted from the slopes of the kinetic energy spectra of the particles emitted from intermediate rapidity sources show a systematic trend with respect to the incident energy ($\tau\approx$10-12 MeV for ^{14}N + ^{197}Au at E/A=35 MeV, $\tau\approx$17-20 MeV for ^{16}O + ^{197}Au at E/A=94 MeV). In contrast, the relative populations of states of light nuclei do not depend sensitively on incident energy and are consistent with emission temperatures of T$\approx$5$\pm$1 MeV. For the ^{14}N+Au reaction, quasi-elastic peripheral reactions and more violent fusion collisions were discriminated by measuring the folding angle between two coincident fission fragments resulting from the decay of the heavy reaction residue. Two-particle correlation

functions, measured at $\theta_{av} \approx 20°$, are more pronounced and more sensitive to the total kinetic energy of the coincident particles for fusion-like collisions as compared to peripheral collisions. Temporal effects could account for this observation. No dependence of relative populations of excited states on the folding angle was established.

Statistical calculations were performed to evaluate the sequential decay of highly excited primary reaction products and the resulting perturbations of the relative populations of widely separated particle unbound states in light nuclei. Previous calculations were improved upon by including more states in the primary distribution and constraining the element distribution by that measured experimentally. Emission temperatures of about 5 MeV, extracted from the relative populations of states in ^{4}He, ^{5}Li, and ^{8}Be nuclei emitted in the ^{16}O+Au reaction at E/A=94 MeV, are not likely due to sequential feeding from an ensemble of primary fragments characterized by much higher initial temperatures.

ACKNOWLEDGMENTS

My stay at Michigan State University will always be remembered in my life. For the friendship I shared, for the education I received, I thank all the staff, students and faculty members of the Physics Department and the NSCL.

In particular, I would like to thank my advisor Prof. Claus-Konrad Gelbke, to whom I owe my deepest gratitude for his patience, support, encouragement, and supervision. I have great respects for his competence in research, his understanding of people, and his sense of responsibility. His effort in my education and his concern for my career have been appreciated and are acknowledged.

I wish to thank other members in my committee. Prof. Sam. M. Austin was my former advisor, and I thank him for the education and for the freedom he gave me to pursue my interests in research. Prof. George Bertsch was very patient in discussing questions in his class, and generous in offering opinions on problems I had in my research. I thank him for all the fruitful discussions I had with him. Prof. S. Mahanti was also very interested in my research and warm in discussing.

During my research, I received tremendous helps from the members in our group. Especially, I would like to thank Prof. W.G. Lynch for his advice. His numerous suggestions, and criticisms had a profound

influence on my graduate career. I thank Dr. M.Y. Tsang for her friendship and unselfish help in my work. Dr. Tetsuya Murakami is acknowledged for his patience in educating me in physics, for numerous conversations on various subjects, and for his friendship which I value so highly. I wish to thank Dr. Josef Pochodzalla for his help in my work. I acknowdge the assistance provided by W.G. Gong and Y.D. Kim in data analysis. I thank my other fellow graduate students, T. Nayak, H. Xu, and F. Zhu, for the pleasure of living and working together.

Finally, I am very proud of the deep understanding and love within my family. To my beloved wife, Xiao-dong Zhang, I am greatly indebted for her affection, respect, understanding and love.

TABLE OF CONTENTS

LIST OF TABLES

LIST OF FIGURES

Figure

page

CHAPTER 1. INTRODUCTION

Since the original proposition of Bohr's compound nucleus reaction model [Bohr 1936], nuclear reaction mechanisms have been studied extensively both theoretically and experimentally. Traditionally, studies have been concentrated on reactions at energies only a few MeV per nucleon above the Coulomb barriers between the colliding nuclei. Recent developments in accelerator technology made it possible to explore nuclear collisions at intermediate and relativistic energies.

At low incident energies, the relative velocity between the colliding ions is smaller than the Fermi velocity. As a consequence, the Pauli exclusion principle strongly suppresses individual nucleon-nucleon collisions and mean field effects dominate the reaction dynamics. Nuclear collisions at small impact parameters lead to complete fusion reactions [Birk 1983, Mose 1984]. Due to the complexity of the coupling between internal degrees of freedom of the nuclei, nearly complete equilibration of excitation energy between the various degrees of freedom can be achieved. The reaction can then be described to proceed via the two independent stages of formation and decay of compound nuclei [Weis 1937, Haus 1952]. Peripheral collisions, on the other hand, are dominated by processes in which the two nuclei essentially retain their identities with varying amounts of mass and energy being transferred between them [Schr 1984].

For nucleus-nucleus collisions at relativistic energies, the velocity between the colliding ions is much larger than the Fermi velosities of the ions. The Pauli exclusion principle is less important and the effects of individual nucleon-nucleon collisions dominate the reaction, leading to rapid equilibration in the interaction volume corresponding to the region of the geometric overlap between projectile and target nuclei. To a good approximation, the system can be divided into participants and spectators. The concept of local statistical equilibrium is often applied and thermodynamic quantities, such as temperature, pressure, and entropy, are used to characterize the system [Naga 1984, Stoc 1986].

The transition from the low energy domain characterized by mean field effects to the high energy domain dominated by individual nucleon-nucleon collisions can be expected at intermediate energies, E/A=20-200 MeV. At these energies, neither pure mean field theories nor simple nucleon-nucleon collision models suffice to describe the dynamics of the reaction. Proper descriptions must incorporate both effects simultaneously [Gelb 1987].

With increasing incident energy above the Coulomb barrier, particle emission sets in before the achievement of global equilibrium, as opposed to the predominant particle emission from fully equilibrated reaction products at lower energies [Gelb 1987]. These fast emission processes were identified experimentally by the shapes of light particle kinetic energy spectra for reactions in which the nearly entire projectile and target nuclei have fused [Awes 1981, Back 1980].

Current theoretical treatments of the reaction dynamics have been focused on the numerical solutions of transport equations which include

nucleon-nucleon collision terms, the Pauli exclusion principle, and mean field effects. Unfortunately, the predictive power of these models is still limited. For instance, calculations based on Boltzmann-Uehling-Uhlenbeck equation [Bert 1980] can predict the energy spectra of nucleons emitted at the early, noncompound stages of the reaction. It is, however, not yet possible to calculate particle correlations or the production of clusters.

In the absence of detailed dynamical treatments of the spatial and temporal evolution of the collision process, recourse is often taken in models based on the assumption of statistical particle emission from nuclear subsets characterized by their average velocity, space time extent, and excitation energy or "temperature" [West 1979, Jaca 1983, Aich 1984]. In fact, the concept of energy localization and consequent heat dissipation was proposed as early as 1938; the effect should be detected by deviations of the particle spectra from those expected for emission from equilibrated compound nuclei [Beth 1938]. If the initial excitation of the target would be localized and thermalized within a finite sub-volume (hot spot), the heated volume should expand into the surrounding cold nuclear matter. Qualitatively, such hot spot models have received support from the comparisons of inclusive kinetic energy spectra of light particles, p, d, and t emitted in high energy nucleus-nucleus collisions [Mekj 1980, Kapu 1980]. More detailed experimental information about the space-time evolution and the temperatures of such subsystems is clearly of interest.

Due to sensitivities to final-state interactions [Koon 1977, Boal 1986, Jenn 1986] and quantum statistics [Kopy 1974a, Kopy 1974b, Yano 1978], two-particle correlation functions for light nuclei at small

relative momenta contain information about the space-time characteristics of the emitting source. Previous measurements of two-particle correlation functions revealed that the magnitude of the measured correlation depends on the sum of the kinetic energies of the detected particles: enhanced correlation functions (indicating smaller source radii) were observed for more energetic particles [Lync 1983, Chit 1986b, Poch 1986a, Poch 1987]. This observation has been interpreted to be consistent with the picture of formation and decay of a localized excited subsystem: high energy protons have large contributions from the early stage of the reaction characterized by a rather small space-time extent and high excitation; low energy protons, on the other hand, are primarily emitted at later stages of the reaction when the excitation is dissipated to a larger volume comparable with the compound nucleus [Lync 1983].

A different explanation, however, was put forward by Bond and Meijer [Bond 1984]. They proposed that the coincident particles were emitted, initially uncorrelated, from two sources: one with approximately beam velocity (projectile-like source); the other nearly at rest (target-like source). Because of the different source velocities, the laboratory energy spectra and angular distributions of particles emitted from these sources were different. High energy particles were associated with the fast-moving projectile-like source whose radius should be small; low energy particles were associated with the target-like source which was almost of the same size as the compound nucleus. In this interpretation, the energy dependence of the correlation functions and the deduced sizes of the emitting source would not require emission from a localized region of high excitation. To

resolve this discrepancy experimentally, one should measure the correlation functions at more backward angles where contributions from the projectile-like source would be suppressed. Contributions from projectile fragments can also be suppressed by measuring light particle correlation functions in coincidence with two fission fragments. The folding angle between the two coincident fission fragments depends on the linear momentum transfer to the fissioning system [Sikk 1962]. Appropriate gates make it possible to select fusion-like reactions with no projectile residues in the exit channel [Back 1980].

Motivated by these considerations, we decided to perform an experiment to measure the correlation functions for ^{14}N induced reactions on ^{197}Au at different average emission angles, and in coincidence with fission fragments.

At the moment when particles leave a system in thermal equilibrium, the relative populations of the individual quantum states carry the information about the excitation energy or "temperature" of the emitting system [Morr 1984, Poch 1985]. If the populations of states could be described in terms of thermal equilibrium distributions corresponding to a single emission temperature, this temperature could be unambiguously determined by measuring the relative populations of two states. On the other hand, the degree of equilibration of the emitting source and the consistency of the statistical treatment can only be investigated by measuring relative populations of a larger number of states.

The relative populations of a number of particle bound states of light nuclei were investigated by particle-Y-ray coincidence measurements [Morr 1984, Bloc 1986, and Xu 1986]. For ^{14}N induced reactions on Ag at 35 MeV per nucleon, surprisingly few ^{7}Li, ^{8}Li, and

^{7}Be nuclei were observed to be emitted in excited states as compared to the respective ground states. These first measurements were initially interpreted to imply temperatures of less than 1 MeV, much lower than the temperatures of the compound nucleus or the kinetic temperatures extracted from the slopes of the kinetic energy spectra of the emitted particles. However, the relative populations of states can be altered by sequential feeding from higher lying excited states [Morr 1984, Poch 1985a]. It was suggested that better temperature determinations could be achieved by measuring the ratios of states largely separated in excitation energy [Poch 1987].

High lying states are particle unbound. Populations for widely separated states were measured for ^{14}N induced reactions on ^{197}Au at E/A = 35 MeV [Chit 1986b] and for ^{40}Ar induced reactions on ^{197}Au at E/A = 60 MeV [Poch 1985] by particle-particle coincidence experiments using a close-packed array of 13 ΔE-E telescopes. The emission temperatures extracted from these two experiments are surprisingly close, about 5 MeV, irrespective of the large difference in projectile-target combination and incident energy.

In order to further investigate the energy dependence of emission temperatures, we measured the relative populations of states in light fragments emitted in the reaction ^{16}O + ^{197}Au at E/A=94 MeV.

In the next chapter, I will review the theoretical concepts which were used for the analysis and interpretation of our experiments. The experimental setups will be described in Chapter 3. Chapter 4 will give details of our analysis. Single particle energy spectra, inclusive two particle correlation functions, emission temperatures, and results gated by linear momentum transfer, will be discussed in Chapters 5, 6, 7, and

8, respectively. In Chapter 9, I will present statistical calculations to assess uncertainties due to sequential feeding. Chapter 10 gives a summary.

CHAPTER 2. CORRELATION FUNCTIONS AND TEMPERATURES

The intensity interferometry technique of Hanbury-Brown and Twiss made it possible to determine the size of a star from the measurement of two-photon correlation functions [Brow 1956]. Similarly, two-pion correlation functions have been used to measure the size of the hadronic fireball produced by proton-proton collisions at high energies [Ezel 1977]. In both methods, the quantum statistical symmetry of the bosons gives rise to correlations between incoherently emitted particles of nearly equal momenta. For photons and, to a good approximation, for pions, the interactions between the emitted particles are negligible.

In addition to effects of quantum statistical symmetries, both Coulomb and nuclear interactions can modify the wave functions of relative motion between light nuclei. The Coulomb interaction is of long range and repulsive between two positively charged particles, suppressing correlations at very small relative momenta. The strong interaction, on the other hand, is attractive and of short range, producing various structures in the correlation functions.

The technique was generalized to correlations between coincident protons [Koon 1977] for which the attractive S-wave interaction leads to a pronounced maximum in the correlation functions at small relative momenta, $q \approx 20$ MeV/c. It was used to investigate the spatial dimensions of emission sources formed in nucleus-nucleus collision [Zarb 1981, Lync

1983, Poch 1986a, Poch 1986c]. The correlation function technique was further generalized and applied to the cases of d-d, p-α, d-α correlations [Chit 1985, Poch 1985a, Poch 1986a, Poch 1986c, Chit 1986b, Chen 1987c].

Experimentally, the two-particle correlation function, R(q), is defined in terms of the singles yields, $Y_1(\vec{p}_1)$ and $Y_2(\vec{p}_2)$, and the coincidence yield, $Y_{12}(\vec{p}_1,\vec{p}_2)$, of particles 1 and 2:

$$\sum Y_{12}(\vec{p}_1,\vec{p}_2) = C_{12}\cdot[1+R(\vec{q})]\cdot\sum Y_1(\vec{p}_1)Y_2(\vec{p}_2) \ . \qquad \text{(II.1)}$$

Here, $\vec{p}_1$ and $\vec{p}_2$ are the momenta of the two detected particles, $\vec{q}$ is the momentum of relative motion, and C_{12} is a normalization constant which is chosen such that the average correlation function, $\langle R(q)\rangle$, vanishes for sufficiently large q, where correlations due to final state interactions become negligible.

The sensitivity of the two-particle correlation function, R(q), to the spatial dimensions of the emitting system can be understood most easily in the thermal model [Jenn 1986]. For a system contained in a volume V, the two-particle density of states can be approximated as:

$$\rho(p_1,p_2)=\rho(P,q) \approx \rho_0(P)\cdot\rho(q), \qquad \text{(II.2)}$$

where P is the total momentum of the two particles and $\rho_0(P) = VP^2/2\pi^2$ denotes the density of states associated with the motion of the center-of-mass of these particles. The factorization on the right hand side of the equation is a good approximation when the interaction of the two particles with the rest of the matter is weak. To first order, the

density of states for the relative motion of the two particles can be approximated as:

$$\rho(q) = \rho_o(q) + \Delta\rho(q). \qquad \text{(II.3)}$$

Here, the plane wave density of states for particles with spin s_i (i=1,2) is given by:

$$\rho_o(q) = (2s_1+1)(2s_2+1)\frac{V \cdot q^2}{2 \cdot \pi^2}. \qquad \text{(II.4)}$$

For non-identical particles, the interaction term, $\Delta\rho$, can be written as [Huan 1963]:

$$\Delta\rho(q) = \frac{1}{\pi} \cdot \sum_{J,\alpha} (2J+1) \cdot \frac{\partial \delta_{J,\alpha}}{\partial q} . \qquad \text{(II.5)}$$

Here, $\delta_{J,\alpha}$ is the scattering phase shift for total angular momentum J and channel quantum numbers α. In contrast to the plane wave density of states, the interaction term does not depend on the volume of the system. Introducing the plane wave density of states, $\rho_o(p_i) = (2s_i+1) \cdot V p_i^2/2 \cdot \pi^2$, for particles i =1 and 2, one obtains:

$$\rho(P,q) \approx \rho_o(P)\rho_o(q) \cdot [1+R(q)]$$

$$= \rho_o(p_1)\rho_o(p_2)[1+R(q)], \qquad \text{(II.6)}$$

where the correlation function, R(q), is given by:

$$R(q) = \frac{2\pi}{(2s_1+1)(2s_2+1)\cdot Vq^2}\cdot \sum_{J,\alpha}(2J+1)\cdot\frac{\partial\delta_{J,\alpha}}{\partial q}. \qquad (II.7)$$

If one assumes that the singles and coincidence yields are given by thermal distributions:

$$Y_i(p_i) \propto \rho_o(p_i)\cdot e^{-E_i/T}, \quad (i=1, 2), \qquad (II.8)$$

$$Y_{12}(p_1,p_2) \propto \rho(P,q)\cdot e^{-(E_1+E_2)/T}, \qquad (II.9)$$

one can see immediately that R(q) in Eq. II.6 agrees with the definition of Eq. II.1. At this level of approximation in the thermal model, the two-particle correlation function depends only on the volume of the emitting source. It is independent of the temperature.

Historically, sensitivity of two-particle correlation function to the space-time extent of the emitting source was derived from a final state interaction model [Koon 1977, Sato 1980]. For simplicity, we neglect the temporal evolution of the emitting source; i.e. we neglect effects due to non-simultaneous emissions. The correlation function can then be expressed in terms of the relative wave function for the two particles, $\psi(\vec{r}_1, \vec{r}_2)$, and single particle spatial source function, $\rho(\vec{r})$ [Koon 1977]:

$$R(q) = \int d^3\vec{r}_1\cdot d^3\vec{r}_2\ \{|\psi_{\Delta\vec{p}}(\vec{r}_1, \vec{r}_2)|^2-1\}\cdot\rho(\vec{r}_1)\cdot\rho(\vec{r}_2)\times$$

$$\left[\int d^3\vec{r}\cdot\rho(\vec{r})\right]^{-2}. \qquad (II.10)$$

The equivalence of Eq. II.10 to Eq. II.7 was shown by Jennings [Jenn 1986]. The theoretical two-particle correlation functions presented in following chapters are calculated from Eq. II.10 assuming a source of Gaussian spatial density,

$$\rho(r) = \frac{1}{\pi^{3/2} \cdot r_0^3} e^{-r^2/r_0^2}. \qquad (II.11)$$

After some elementary manipulation, two-particle correlation function can then be as:

$$R(q) = \frac{1}{(2\pi)^{3/2} r_0^3} \int d\vec{r} \cdot \exp(-r^2/2r_0^2) \{ |\psi_{\Delta\vec{p}}(\vec{r})|^2 - 1 \}. \qquad (II.12)$$

For fixed spatial source dimensions, the magnitude of two-particle correlation functions is expected to decrease when the particles are emitted in larger time intervals [Koon 1977]. The simplifying assumption of negligible lifetime can, therefore, only provide upper limits for the spatial dimension of the emitting source.

Information about the temperature of a thermal system can be obtained by investigating the relative populations of states. In the thermal model, the probabilities for nuclei to be emitted at an excited state of energy E can be written as (see also Eq. II.8-II.9):

$$\frac{dn(E)}{dE} = N \cdot e^{-E/T} \cdot \Delta\rho(E). \qquad (II.13)$$

where N is a normalization constant and $\Delta\rho(E)$ is the density of states. For the continuum states, this density of states is given by Eqs. II.3-II.5. If the energy dependence of the phase shift is dominated by series

of resonance interactions, the density of unbound states can be further approximated as a sum over Breit-Wigner terms:

$$\Delta\rho(E) = \sum_i \frac{(2J_i+1)\ \Gamma_i/2\pi}{(E-E_i)^2+(\Gamma_i/2)^2}, \qquad \text{(II.14)}$$

Bound excited states will decay by Y-ray emission. Unbound states will decay predominantly by particle emission, and the population of states decaying into the channel c can be written as:

$$\left[\frac{dn(E)}{dE}\right]_c = N \cdot e^{-E/T} \cdot \sum_i \frac{(2J_i+1)\Gamma_i/2\pi}{(E-E_i)^2+(\Gamma_i/2)^2} \cdot \frac{\Gamma_{c,i}}{\Gamma_i}, \qquad \text{(II.15)}$$

where $\Gamma_{c,i}/\Gamma_i$ denotes the branching ratio for the decay into channel c. In the limit of two sharp states separated by an energy $\Delta E=E_1-E_2$, the primary relative population, R_{12}, of states, 1 and 2, reduces to the simple expression [Morr 1984]:

$$R_{12} = \frac{(2J_2+1)}{(2J_1+1)} \cdot \exp(-\Delta E/T), \qquad \text{(II.16)}$$

CHAPTER 3. EXPERIMENTAL DETAILS

3.1 $^{14}N + ^{197}Au$ at E/A = 35 MeV

The experiment was performed at the National Superconducting Cyclotron Laboratory at Michigan State University. Gold targets of 1.1, 10, and 19 mg/cm^2 areal density were irradiated with ^{14}N ions of E/A=35 MeV incident energy. A hodoscope and a pair of fission detectors were set up in the 60" Chamber of NSCL. The schematic view of the complete experiment is shown in Figure III.1. Correlation functions at larger angles were measured by moving the hodoscope to these angles and disconnecting the fission detectors.

Single and two-particle inclusive measurements were performed with the center of the hodoscope positioned at the angles of Θ_{av}= 20°, 35° and 50° with respect to the beam axis; for these measurements a thick (19 mg/cm^2) gold target was used. Measurements in coincidence with two fission fragments were performed with the center of the hodoscope positioned at Θ_{av}= 20°; for these measurements a thin (1.1 mg/cm^2) gold target was used.

Light particles (Z≤3) were detected by a close packed hexagonal array of 13 ΔE-E telescopes. Each telescope subtended a solid angle of 0.94 msr; the angular separation between adjacent detectors was 6.1°. The front view of the hodoscope is shown in Figure III.2. Every telescope consists of a 400 μm thick Si detector and a 10 cm thick NaI

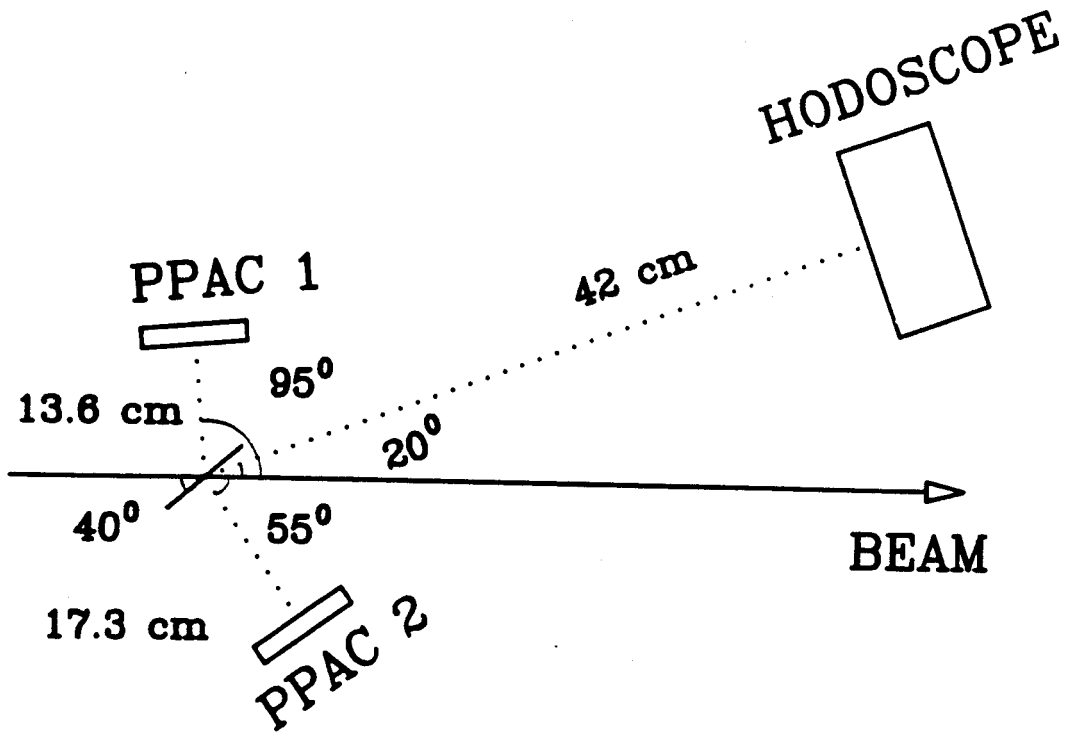

Figure III.1 Schematic view of the experimental setup. The average detection angle for light particles, Θ_{av}, is 20°, and the hodoscope is placed 42 cm from the target which is mounted with an angle of 40° with respect to the beam direction. The fission detectors are mounted at the distances d_1=13.6 cm and d_2= 17.3 cm, and the angles Θ_1= 95° and Θ_2= 55°, respectively.

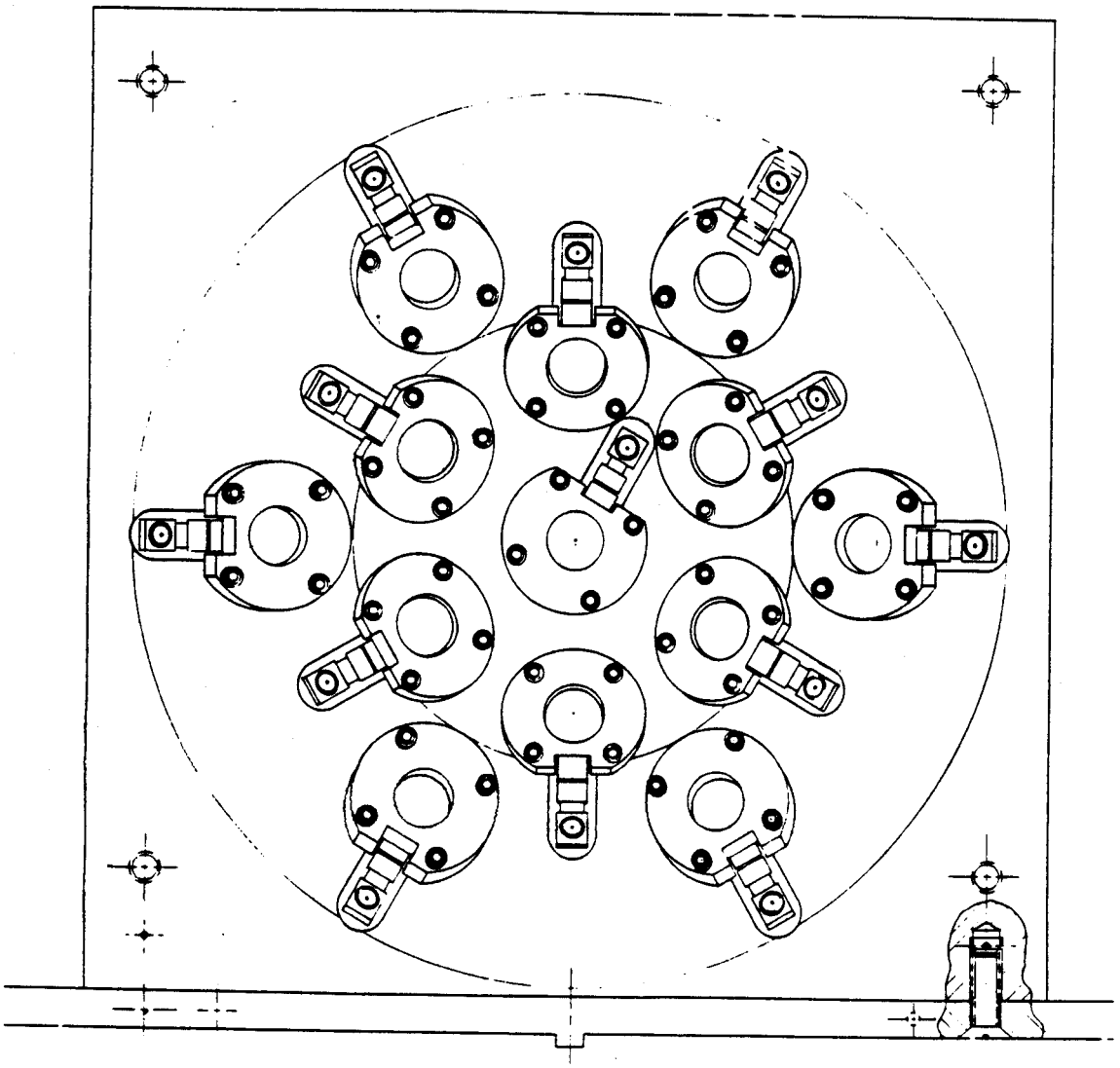

Figure III.2 Schematic view of the front face for the 13-element hodoscope.

detector. The NaI crystals were canned in aluminum cases with a thin Harvor foil as an entrance window, and the light produced by the crystal was detected by a photomultiplier on the back of the crystal. An optical fiber was inserted into the detector; the other end of the fiber was connected to a light pulser system. Two highly stable PIN diodes were used to monitor the magnitude of light pulsers on a pulse by pulse basis. For each light pulse, the signals from the PIN diodes and all the photomultipliers were digitized and recorded on magnetic tape. Gain shifts of the photomultipliers were detected by comparing their outputs to that of the PIN diodes in each pulse. In front of each telescope was a 1/2" thick copper collimator covered with a 2.4 mg/cm^2 gold foil to shield the Si-detector from low energy electrons, X-rays, and fission fragments. A supply voltage of 800 V was applied to the photomultipliers, and energy signals of the detected particles were extracted from the 6th dynode of the photomultiplier.

Coincident fission fragments were detected with two X-Y-position sensitive parallel plate detectors with individual active areas of 11×11 cm^2. These detectors were mounted in the plane defined by the center of the light particle hodoscope and the beam axis. They were positioned at the distances of d_1= 13.6 cm and d_2= 17.3 cm from the target and at the polar angles with respect to the beam axis of Θ_1= 95° and Θ_2= 55°, respectively. Each of the parallel plate detectors has two layers of cathodes made of 12 conducting stripes, separated by 0.2" from each other. The directions of the stripes on the two cathodes are perpendicular to each other to allow two-dimensional position measurements. The stripes were connected to tapped delay line chips with 0.2 ns delays for adjacent taps. The time needed for a signal to

propagate to each end of the delay line was measured with respect to the prompt signal from the anode. The position of the ionization in the detector can then be obtained from the time difference of the time signals from the two ends in each dimension.

Single particle inclusive cross sections for Li and Be fragments were measured in a separate run using two ΔE-ΔE-E silicon detector telescopes consisting of detectors of 75 μm, 400 μm, and 5 mm thickness. The solid angles of these telescopes were 2.1 and 4.1 msr; the target thickness was 10 mg/cm^2.

The energy calibrations of silicon detectors were performed by injecting known amounts of charge into the preamplifier inputs. The energy calibrations of the NaI detectors were established by scattering alpha particles of 60 and 100 MeV energy from a polyethylene target and detecting the scattered alpha particles and recoil protons at various scattering angles.

The block diagram of the electronics is shown in Figure III-3. The analog signals from the NaI and Si detectors were preamplified, shaped and amplified, and then recorded by peak sensing ADCs. Logic signals were extracted from fast signals derived from the Si detectors and photomultiplier anodes. The anode signal, after one stage of fast amplification, was divided into two channels, providing two different thresholds, E_{low} and E_{high}. A valid telescope event was defined as: $E_{low} \cdot (E_{high} + E_{si})$. The condition $(E_{high} + E_{si})$ avoids recording low energy Y-rays and neutrons, while accepting high energy protons for which the ΔE-signals might be too low to generate an E_{si} trigger. The time was determined by the E_{low} signal. The E_{low} thresholds were set during the experiment to accept protons of about 7 MeV. The valid

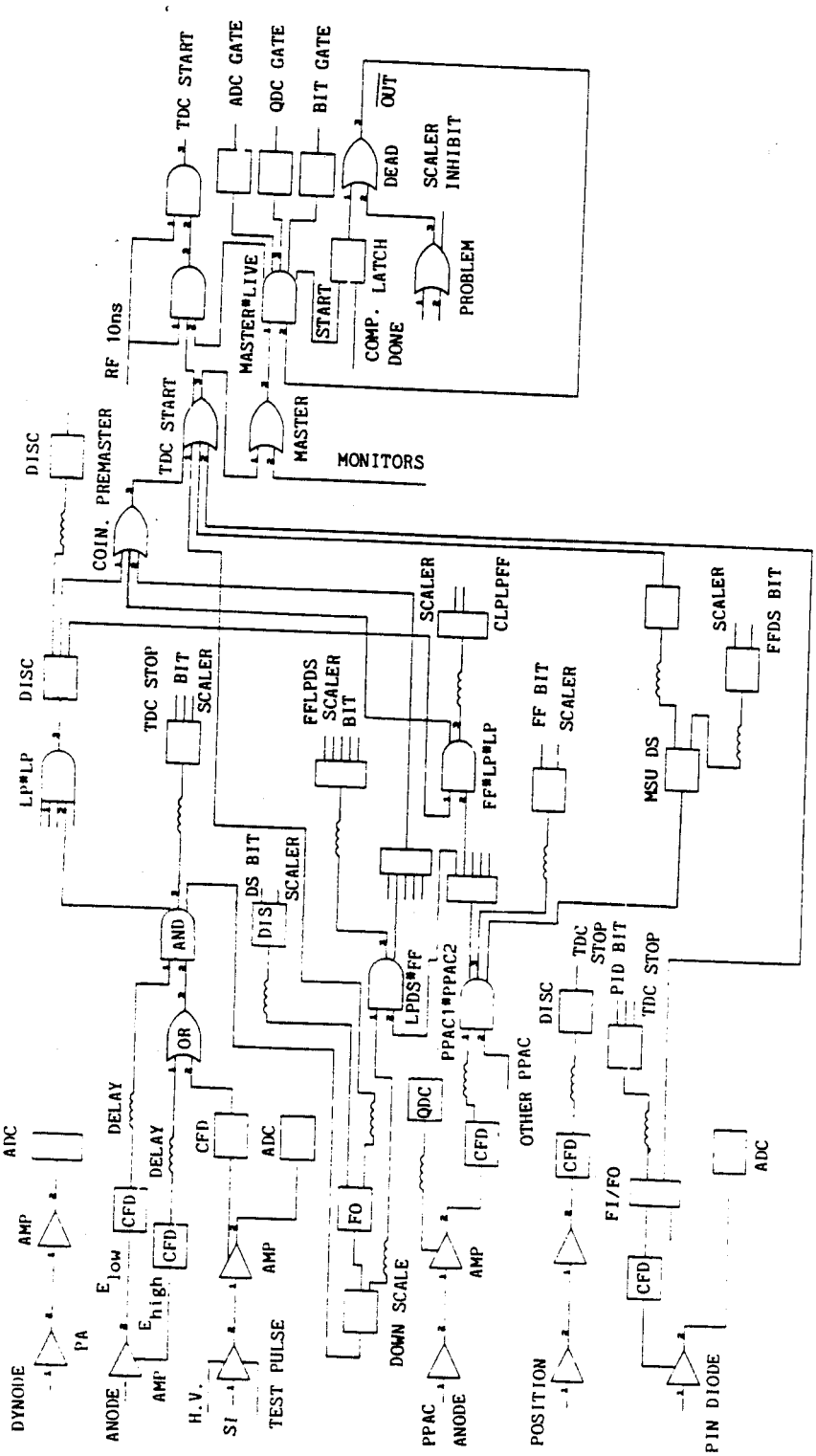

Figure III.3 Block diagram of the electronics used in the experiment ^{14}N + ^{197}Au at E/A=35 MeV.

telescope signals, with time being determined by the low energy threshold channel, were sent to a coincidence multiplicity unit, and to TDC stops, bit registers, scalers, and downscale units. A fission event was defined by the coincidence of the anode signals from the two gas counters and sent to coincidence units, TDC stop, downscale, and bit register. The following types of event were defined to trigger the computer: two coincident light particles, downscaled light particle singles, two coincident light particles in coincidence with two fission fragments, downscaled light particle singles detected in coincidence with two fission fragments, downscaled fission events, and light pulser signals. A dead time circuit was used after the master trigger unit to inhibit further events during computer busy time.

3.2 ^{16}O + ^{197}Au at E/A = 94 MeV

The experiment was performed at the Laboratoire Grand Accélérateur National d'Ions Lourds (GANIL) at Caen. A gold target of 3 mg/cm^2 areal density was irradiated by an ^{16}O beam of E/A = 94 MeV incident energy. Light particles ($Z \leq 3$) were detected by a close-packed hexagonal array of 18 ΔE-E telescopes, each consisting of a 300 μm thick planar surface barrier detector of 450 mm^2 active area and a 10 cm thick NaI(Tl) scintillator. The NaI detectors were already described in Section 3.1. The front view of this hodoscope is shown in Figure III.4. The angular separation between the centers of adjacent telescopes was Θ_{min}=2.7°; the maximum relative angle was 11.9°. Each telescope subtended a solid angle of 0.44 msr corresponding to a resolution in relative angle of $\Delta\Theta_{fwhm} \approx$ 1.2°. The detectors were located at a distance of 102 cm from the target; the center of the hodoscope was positioned at a laboratory angle

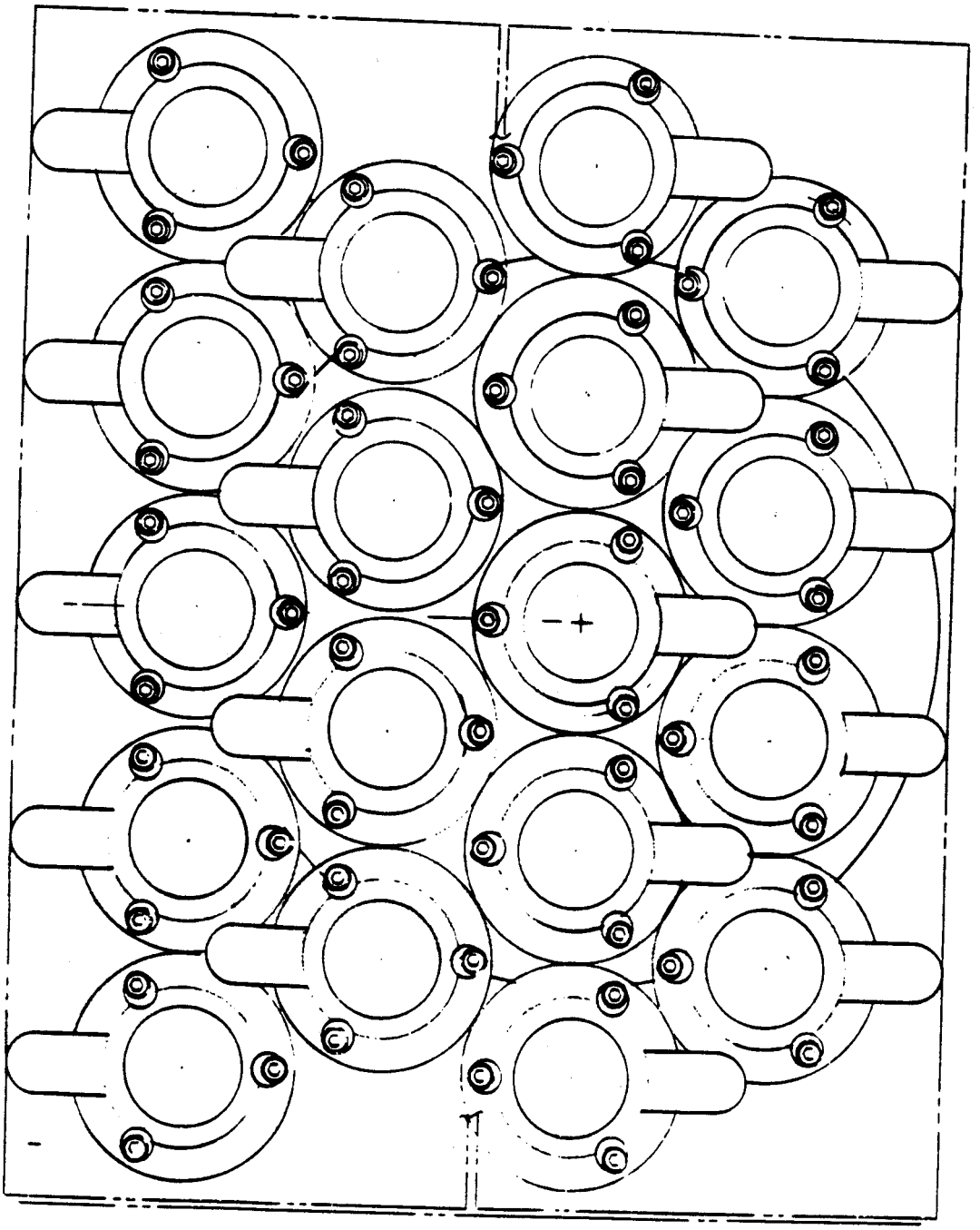

Figure III.4 Schematic view of the front face for the 18-element hodoscope.

of Θ_{av}= 45°. At this large angle, contributions from peripheral projectile breakup reactions are negligible. Complete isotopic separation of Z=1-3 nuclei was achieved with these telescopes. As an example, Figure III.5 shows a two-dimensional plot of the particle identification function, PID, versus N_{NaI} for telescope #2. Because of insufficient statistics for Z=3, only light particles with Z≤2, in which we are mainly interested, are plotted. Here the particle identification function was generated [Goul 1975] as:

$$PID \propto (N_{NaI} + 0.18 \cdot N_{si})^{1.75} - N_{NaI}^{1.75} \qquad (III.1)$$

As in the previous experiment, the energy calibrations of the silicon detectors were performed by injecting known amounts of charge into the preamplifier inputs. The energy calibration and energy resolution for NaI detectors were established by the following procedure. Secondary particles, produced by bombarding a thick carbon target with ^{16}O ions, were analysed according to the magnetic rigidity with a 270° beam transport system and injected into the telescopes by moving each telescope to Θ = 0°, into the beam of secondary particles. Several settings of the magnetic rigidities, B•ρ, were used to get a span in energy range of interest (shown in Table 1). This method has the distinct advantage of allowing the simultaneous calibration for a large number of different particles.

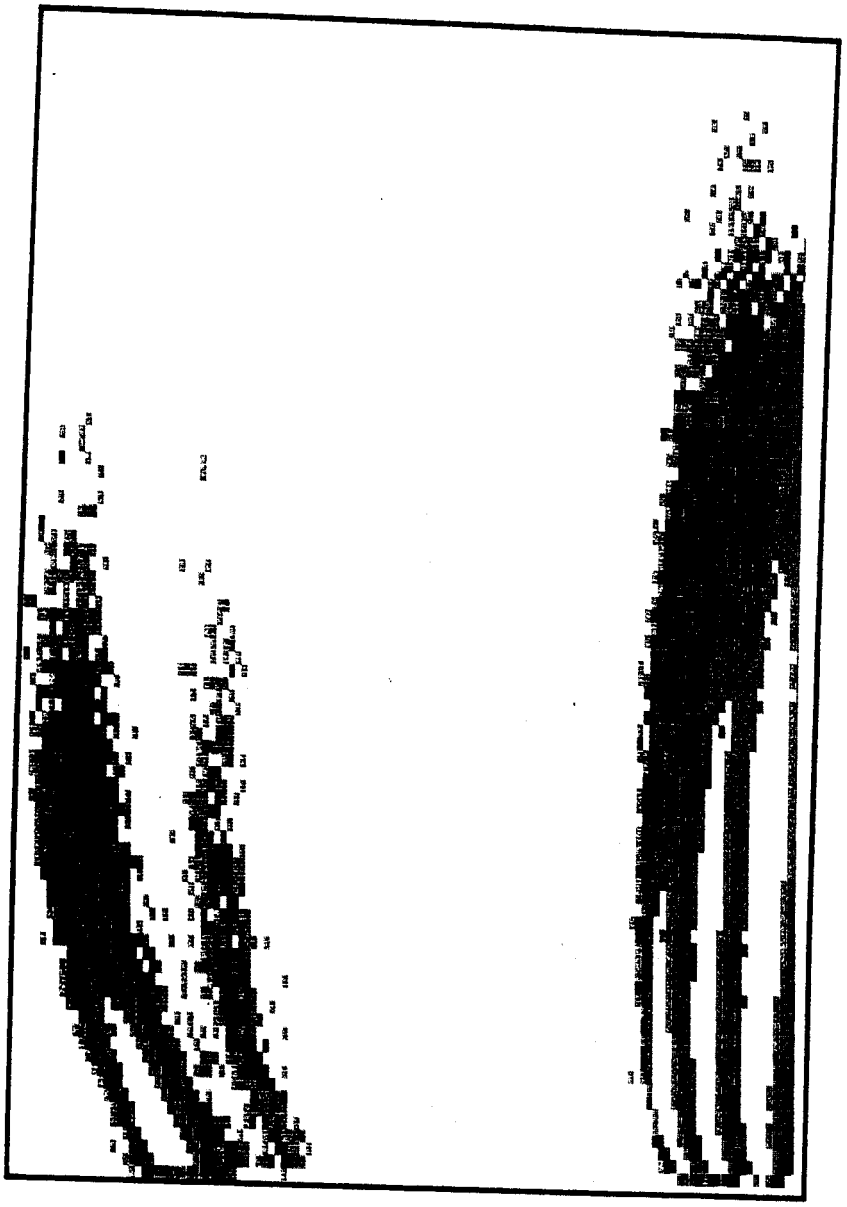

Figure III.5 Particle identification function for telescope #2.

TABLE 1

Magnetic rigidities used for energy calibration and corresponding energies for different light nuclei.

Rigidity (Tm)	Proton (MeV)	Deuteron (MeV)	Triton (MeV)	^{3}He (MeV)	^{4}He (MeV)	^{6}Li (MeV)
0.5000	11.89	5.98	4.00	15.95	12.03	18.02
0.7162	24.24	12.25	8.19	32.63	24.65	36.90
0.9001	38.01	19.31	12.93	51.37	38.86	58.18
1.0140	47.99	24.47	16.40	65.03	49.24	73.73
1.2435	71.31	36.66	24.62	97.25	73.81	110.52
1.5289	105.93	55.18	37.15	145.79	111.05	166.27
1.8395	149.99	79.37	53.61	208.75	159.72	239.15
2.2648	219.80	119.08	80.88	310.98	239.60	358.77

CHAPTER 4. ANALYSIS

4.1 ENERGY CALIBRATIONS

The ΔE detectors were calibrated by injecting known amounts of charge, Q, into Si detector preamplifiers. The pulse positions were fitted linearly,

$$\Delta E = a \cdot N_{si} + b. \qquad \text{(IV.1)}$$

where ΔE denotes the energy related to the injected charge via $\Delta E = 2.25 \cdot 10^{13}$ (MeV/C)•Q, N_{si} is the ADC channel number, and a and b are calibration constants (see Table 3).

A more elaborate procedure was used for the energy calibration of the NaI detectors. Previous investigations [Tayl 1951] indicate that the reduced light output of a scintillator, L/AZ^2, primarily depends on the reduced energy deposited in the material, E/AZ^2, where A and Z are the mass and charge of the ion stopped in the detector. When the incident energy is large so that the amount of energy lost in the dead layer at the front of detecting material is negligible, it is a good approximation to represent the energy deposited in the NaI detector as follows:

$$E/(AZ^2) = a_1 + a_2 \cdot (L/AZ^2) + a_3 \cdot (L/AZ^2)^2 \qquad \text{(IV.2)}$$

where, the coefficients a_i (i=1,3) were adjusted to fit the calibration points. The amount of light produced in the scintillator, L, is assumed to be the ADC channel number, N_{ch}, corrected for the electronic offset, N_{off}, via $L=N_{ch}-N_{off}$, where N_{off} was determined from the pulser calibrations.

At low energies, when the energy loss in dead layers becomes comparable to the energy deposited in the active volume, deviations from Eq. IV.2 become large. At these low energies, we applied a correction using the energy loss, ΔE, measured with the Si detector.

For this purpose, we first selected high energy points in the calibration, and used Eq. IV.2 to fit the parameters a_i. The residual energy, E_r, which is the difference between the true energy, E_{tot}, and that calculated from Eq. IV.2, is then fit by the expression:

$$E_r = b_0 + b_1 \cdot \Delta E + b_2 \cdot \Delta E^2 \qquad \text{(IV.3)}$$

The coefficients, b_i (i=0,1,2), were fit for each detector and for each type particle. For protons, deuterons, ^{3}He, and ^{4}He, the energy deposited in the NaI detector is finally expressed as

$$E_{NaI} = C_1 + C_2 \cdot \Delta E + C_3 \cdot \Delta E^2 + C_4 \cdot L + C_5 \cdot L^2 \quad . \qquad \text{(IV.4)}$$

Here, ΔE is the energy in Si detector, and L is the channel number from the NaI detector corrected for offset. As an example, the coefficients C_i for telescope #2 are listed in Table 3 for these particles.

For lithium isotopes and beryllium isotopes, we used one set of parameters for each element, and the resulting formula reads

$$E_{NaI}/AZ^2 = C_1 + C_2 \cdot \Delta E + C_3 \cdot \Delta E^2$$

$$+ C_4 \cdot (L/AZ^2) + C_5 \cdot (L/AZ^2)^2. \qquad \text{(IV.5)}$$

Here, A and Z are the mass and charge number of the individual isotopes, and the coefficients C_i for telescope #2 are tabulated in Table 3.

For tritons, no high energy calibration points were available due to their small charge to mass ratio ($B\rho=mv/q$). The calibration at higher energies was obtained by the information from protons and deuterons taking advantage of Eq. IV.2. The final expression for this case is

$$E_{NaI}/AZ^2 = C_1 + C_2 \cdot (L/AZ^2) + C_3 \cdot (L/AZ^2)^2$$

$$+ C_4 \cdot E' + C_5 \cdot E'^2 + C_6 \cdot E'^3, \qquad \text{(IV.6)}$$

where

$$E' = \begin{cases} \Delta E - E_0 & \text{when } \Delta E > E_0, \\ 0 & \text{when } \Delta E < E_0. \end{cases} \qquad \text{(IV.7)}$$

Here, A and Z are the mass and charge number for tritons, and the coefficients C_i and E_0 for telescope #2 are tabulated in Table 3.

For illustration, Table 2 lists the raw data and calibrated energies for telescope #2. The quality of this calibration can be appreciated by the relative deviation of calculated and measured energies. Figure IV.1 compares the result of the calibration with the data graphically.

TABLE 2

Total energies and channel numbers for the calibration points for telescope #2. N_{Si} and N_{NaI} are the channel numbers for Si and NaI detectors, respectively; E_{tot} and E_{cal} are respectively the measured and fitted energies.

Particle	N_{Si} (channel)	N_{NaI} (channel)	E_{tot} (MeV)	E_{cal} (MeV)	$(E_{tot} - E_{cal})/E_{tot}$ [%]
Proton	151.5	77.72	11.89	11.90	-0.06
Proton	80.37	193.7	24.24	24.15	0.36
Proton	58.1	305.4	38.01	38.08	-0.18
Proton	48.7	381.9	47.99	48.22	-0.47
Proton	37.5	542.7	71.31	70.92	0.54
Proton	29.5	770.89	105.93	106.15	-0.21
Proton	23.6	1028.0	149.99	149.93	0.04
Deuteron	266.6	54.9	12.25	12.25	0.00
Deuteron	169.3	133.2	19.31	19.35	-0.20
Deuteron	100.7	291.0	36.68	36.58	0.26
Deuteron	133.1	183.6	24.47	24.39	0.30
Deuteron	74.3	444.6	55.18	55.53	-0.63
Deuteron	56.0	620.9	79.37	79.09	0.35
Deuteron	42.7	893.5	119.08	119.14	-0.05
Triton	356.0	41.2	12.93	12.925	0.04
Triton	276.8	85.1	16.40	16.43	-0.19
Triton	190.7	170.4q	24.62	24.51	0.45
Triton	136.9	288.7	37.15	37.33	-0.47
Triton	101.7	425.9	53.61	53.50	0.21
Triton	75.1	638.8	80.88	80.90	-0.03
^{3}He	679.88	106.6	32.63	32.61	0.04
^{3}He	426.5	293.6	51.37	51.43	-0.13
^{3}He	348.7	416.9	65.03	65.10	-0.11
^{3}He	249.3	687.4	97.25	96.78	0.48
^{3}He	180.6	1085.3	145.79	146.47	-0.47
^{3}He	137.8	1552.0	208.75	208.34	0.20
^{3}He	100.2	2275.2	310.98	311.05	-0.02
^{4}He	723.7	135.8	38.86	38.83	0.08
^{4}He	567.0	239.2	49.24	49.38	-0.28
^{4}He	393.0	458.0	73.81	73.48	0.45
^{4}He	280.5	776.8	111.05	111.49	-0.40
^{4}He	209.0	1158.2	159.72	159.46	0.16
^{4}He	153.6	1761.8	239.60	239.65	-0.02
^{6}Li	1853.0	54.6	58.18	57.63	0.93
^{6}Li	1366.8	204.9	73.73	73.49	0.32
^{6}Li	903.5	513.5	110.52	109.77	0.68
^{6}Li	630.1	959.5	166.27	166.86	-0.35
^{6}Li	339.7	2391.2	358.77	358.90	-0.04
^{7}Li	1934.9	67.7	63.32	63.88	-0.88
^{7}Li	1195.7	349.0	95.00	95.63	-0.66
^{7}Li	815.9	736.4	143.10	143.6	-0.35
^{7}Li	959.8	1213.3	206.15	205.66	0.24
^{7}Li	427.1	1988.3	310.08	309.41	0.22

TABLE 3

Energy calibration constants for telescope # 2

Particle	C_1	C_2	C_3	$C_4(10^{-2})$	$C_5(10^{-4})$	C_6
Proton[1)]	1.14097	-0.21278	0.26402	11.31251	0.32333	
Deuteron[1)]	0.82073	1.29395	-0.16518	10.98137	0.25883	
Triton[3)]	0.8161	0.1176	0.00003	13.64	257.0	-0.00655
^{3}He[1)]	11.68106	0.18912	-0.02268	11.46453	0.07427	
^{4}He[1)]	9.96222	0.76891	-0.04702	11.99371	0.05191	
Li[2)]	0.42761	0.00871	-0.00030	13.84165	-0.07328	
Be[2)]	0.69707	-0.01503	0.00015	13.54057	1.37476	

N_{off}=9.377

Constants for Si: a= 0.01533, b=-0.116

1) Coefficients for Eq. IV.4
2) Coefficients for Eq. IV.5
3) Coefficients for Eq. IV.6

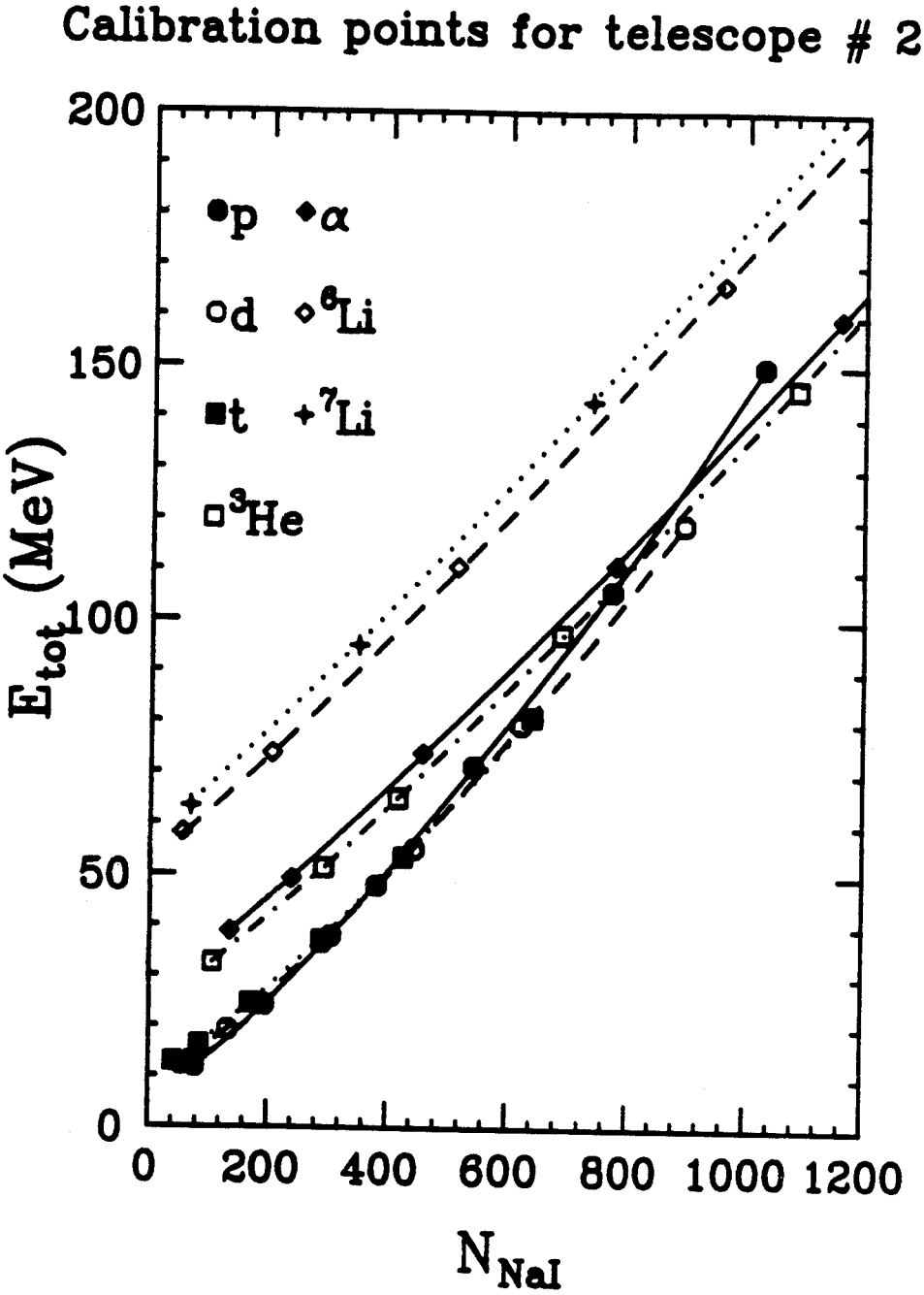

Figure IV.1 Energy calibrations for telescope #2. The horizontal scale gives the channel number, and the vertical scale gives the energy determined from the rigidity of the analyzing magnet.

Gain shifts of the photomultipliers and the electronics were monitored by a light pulser. Since the individual light pulses were detected by the two PIN diodes and by all photomultipliers of the hodoscope, we evaluated the ratio P_{tel}/P_{pin}, where P_{tel} and P_{pin} denote the pulse heights from the photomultiplier and the PIN diode, respectively, and created a spectrum of this quantity for each photomultiplier. The shifts of the peak position in the P_{tel}/P_{pin} spectrum are due to gain shifts of the photomultiplier, since the stability for the PIN diode is high. The stability of the PIN diodes was cross checked by forming the ratio P_{pin1}/P_{pin2}, which was constant within 0.5%.

When the hodoscope was physically moved, the curvature of the optical fibers and the contact in the optical connectors was generally changed and the light pulser gain stabilization had to be renormalized. In such cases, a different technique was employed. This technique made use of the high stability of the Si detectors. For this purpose, the raw data were first sorted into standard ΔE-E spectra, and narrow gates parallel to the E axis were chosen across the ridges of a number of particle lines. A gaussian fitting procedure was performed to determine the centroids, P_i, for the peaks in the individual gates. The relative gain shift, ξ, was extracted by minimizing the function $f(\xi)$,

$$f(\xi) = \sum_i [\xi \cdot P_i - P_{oi}]^2 / P_{oi}^2 \qquad \text{(IV.8)}$$

with respect to ξ, where i runs over the number of peaks, and P_{oi} are the peak locations for the calibration run. Shifts of the order of 1% could be detected with this technique. This technique was applied for

matching gains between the calibration runs and data-taking runs, and when the detectors were moved.

4.2 RANDOM CORRECTIONS FOR 3-FOLD COINCIDENCES

Although parts of the experiment were performed in four-fold coincidence, we checked that the random coincidence rate between two fission fragments was negligible. Hence, the effective number of relevant time signals reduces to three: two time signals, t_1 and t_2, for the light particles, 1 and 2, and the overlap timing of two fission detectors, denoted as t_3.

For the analysis, we calibrated the time spectra, so that the individual peaks in the time difference spectra between telescopes and fission detectors, $t_{i3} = t_i - t_3$, were aligned for all telescopes, i.

Time differences of telescopes with respect to fission detectors, t_{13} and t_{23} for particles 1 and 2 in a given telescope pair, were sorted into a two-dimensional spectrum. An example is given in Figure IV.2a; a schematic identification of the peaks is given in Figure IV.2b. The random peaks, denoted as R, comprise three signals in random coincidence from different beam bursts. This background contributes to every peak in the map with approximately the same magnitude (slight differences can arise from beam intensity fluctuations). Double coincident peaks, denoted as D, correspond to two signals in real coincidence and the third in a random coincidence. The interesting component of real triple coincidences is contained in the central peak, T. Mathematically, these peaks can be decomposed as follows:

$$T = P_{123} + P_{12} \cdot P_3 + P_{23} \cdot P_1 + P_{13} \cdot P_2 + P_1 \cdot P_2 \cdot P_3, \qquad \text{(IV.9)}$$

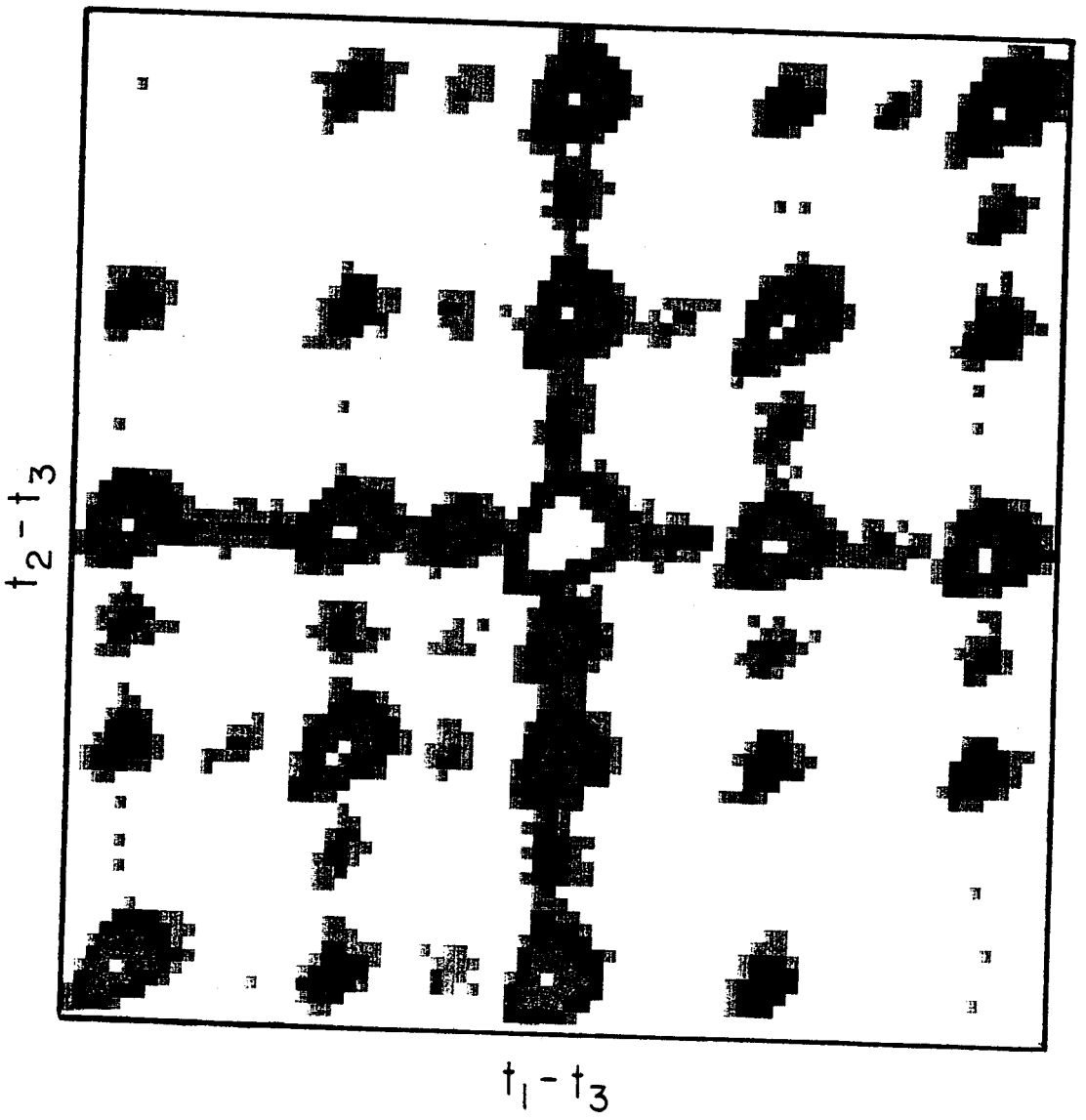

Figure IV.2a Time difference of two telescopes, 1 and 2, with respect to fission detectors, t_{13} vs. t_{23}, for the 3-fold coincidence experiment. Peaks of different intensity are observed.

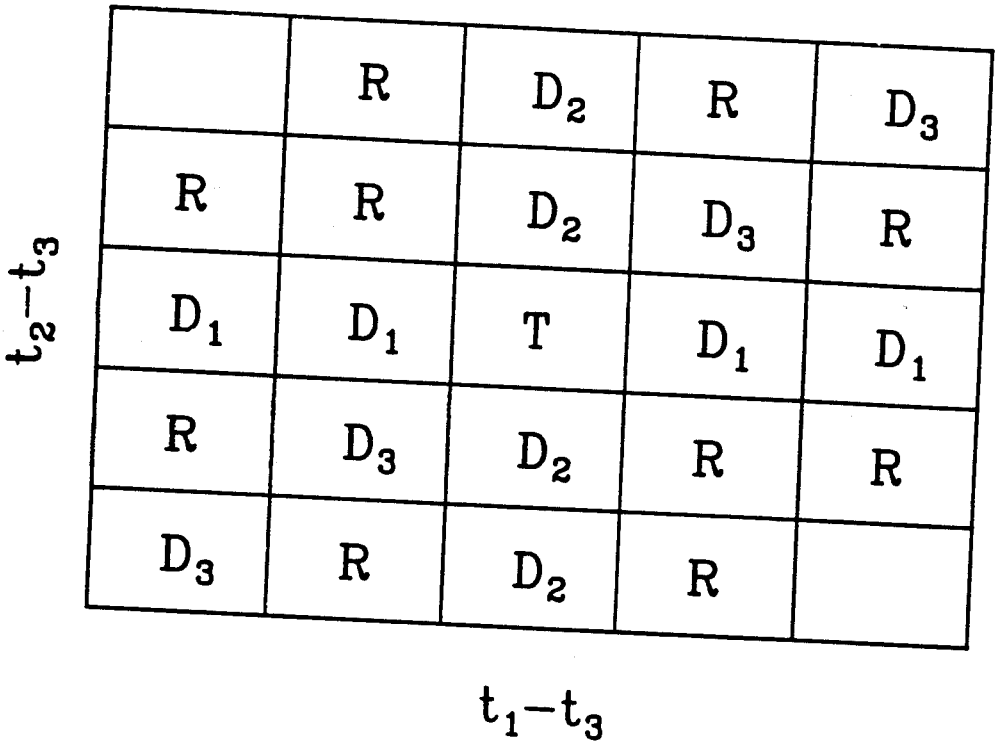

Figure IV.2b Schematic identification of the peaks in the spectrum, t_{13} vs. t_{23}. The random peaks, denoted as R, comprise three signals in random coincidence from different beam bursts. Double coincident peaks, denoted as D, correspond to two signals in real coincidence and the third in a random coincidence. The interesting component of real triple coincidences is contained in the central peak, T. see text for the decomposition.

$$D_1 = P_{23} \cdot P_1 + P_1 \cdot P_2 \cdot P_3, \tag{IV.10}$$

$$D_2 = P_{13} \cdot P_2 + P_1 \cdot P_2 \cdot P_3, \tag{IV.11}$$

$$D_3 = P_{12} \cdot P_3 + P_1 \cdot P_2 \cdot P_3, \tag{IV.12}$$

$$R = P_1 \cdot P_2 \cdot P_3. \tag{IV.13}$$

Here P_i is the probability for observing single signal within a given beam burst, P_{ij} is the true two-fold coincidence probability for particles i and j generated in the same nuclear interaction, and P_{123} is the true triple coincidence probability for three signals generated in the same interaction. Other satellites between the peaks are due to misfiring of about 1% in intensity.

For each telescope combination, E_1 vs. E_2 spectra were created for a pair of coincident light particles gated by different peaks, respectively. The random corrected spectra were obtained by evaluating for each point the sum:

$$P_{123} = T - (D_1 + D_2 + D_3) + 2 \cdot R \tag{IV.14}$$

Random corrections are also performed on the light particle kinetic energy spectra for simple particle-fission coincidences. This correction is standard.

4.3 CORRELATION FUNCTIONS AND EXPERIMENTAL YIELDS FOR UNBOUND STATES

Experimentally, the two-particle correlation function is defined in Eq. II.1. In most cases, the sum in the equation was extended over all the possible particle momenta in a given relative momentum bin, $q = |\vec{q}|$, regardless to the vector nature of relative momentum. The normalization range in the relative momentum was chosen for each pair of particles to correspond to a region of large relative momenta free of distinct structure in R(q).

Intermediate files were created for the two dimensional energy spectra, E_i vs. E_k, for all telescope combinations, i and k, for both real and random coincidences, where E_i and E_k are the measured energies of the two coincident particles. Once a particle is recorded in a detector, its direction of motion is assumed to be along the centre angle of that detector. Relativistic kinematics is used to calculate the momentum of this particle, $\vec{p}_i$. Given a pair of telescopes, the coincidence yield, $Y_{12}(\vec{p}_1, \vec{p}_2)$, is created by subtracting the random coincidence from the total coincidence at each location in the two dimensional spectra. The product of the single yields, $Y(\vec{p}_1) \cdot Y(\vec{p}_2)$, is generated from the random spectra.

The momentum vectors in the laboratory frame are transformed into the momentum for the motion of center of mass, $\vec{P}$, and the momentum for relative motion, $\vec{q}$. They can be written as

$$P_\mu = p_{1\mu} + p_{2\mu}, \qquad \text{(IV.15)}$$

$$\vec{q} = \vec{p}_1 + \frac{\gamma-1}{\beta^2}(\vec{\beta}\cdot\vec{p}_1)\vec{\beta} - \gamma p_{1_0}\cdot\vec{\beta}, \qquad \text{(IV.16)}$$

where $p_{i\mu}$ (i=1,2) are the four-momentum for the i-th particle, $\vec{\beta}$ is the velocity for the motion of center of mass, $\frac{\vec{P}}{P_0}$, and $\gamma=(1-\beta^2)^{-1/2}$.

Angular variables, Θ_R and Φ_R, between these two vectors are calculated, using the definitions:

$$\cos(\Theta_R) = [\vec{P}\cdot\vec{q}]/[|\vec{P}|\cdot|\vec{q}|], \tag{IV.17}$$

$$\cos(\phi_R) = [(\vec{n}_b\times\vec{P})\cdot\vec{q}]/[|\vec{n}_b\times\vec{P}|\cdot|\vec{q}|]. \tag{IV.18}$$

Here, $\vec{n}_b$ is normal to the reaction plane defined by the beam direction and the direction of $\vec{P}$.

Summations are performed over $\vec{P}$, the direction of $\vec{q}$, and all the telescope combinations, $\sum Y_{12}(\vec{p}_1, \vec{p}_2)$. The same procedure of transformation and summation is also performed over the random coincidence spectra which are proportional to the singles products, $\sum Y_1(\vec{p}_1)\cdot Y_2(\vec{p}_2)$. The average ratio of these two spectra, as indicated in Eq. II.1, is then normalized to unity at large relative momenta.

The experimental yield, Y_c, for a particle unbound state is assumed to be the difference between the coincidence yield, Y_{12}, and the background yield, Y_b, due to nonresonant particle emissions. Uncertainties exist for the determination of background emission. To visualize this contribution, we define a background correlation function, $R_b(q)$, whose exact shape might lie within some limits we estimate to be reasonable. In this way, the yield due to resonant decays can be written as:

$$Y_c(\vec{p}_1,\vec{p}_2) = Y_{12}(\vec{p}_1,\vec{p}_2) - C_{12}\cdot Y_1(\vec{p}_1)\cdot Y_2(\vec{p}_2)[1+R_b(q)] \quad , \quad \text{(IV.19)}$$

where C_{12} is defined in Eq. II.1.

4.4 EXTRACTION OF EMISSION TEMPERATURES

Under the assumption of thermal equilibrium, the relative populations of two states are determined by the temperature of the emitting system at the moment when the particles leave the system. The coincidence yields of particle unbound states can be written as:

$$Y_c(E') = \int dE\cdot\varepsilon_c(E',E)\times\left\{\frac{N}{\pi}\cdot e^{-E/T}\cdot\sum_i\left[\frac{(2J_i+1)\cdot\Gamma_i/2}{(E-E_i)^2+\Gamma_i^2/4}\cdot\frac{\Gamma_{c,i}}{\Gamma_i}\right]\right\} \quad \text{(IV.20)}$$

where, E_i, J_i and Γ_i are the resonance energy, spin and total width of state i; $\frac{\Gamma_{c,i}}{\Gamma_i}$ is the branching ratio for the decay channel c; T is the "emission temperature" of the source; $\varepsilon_c(E',E)$, is the efficiency function of the hodoscope; E and E' are the actual and measured excitation energies, respectively. (The excitation energy E and the relative kinetic energy, $T_{c.m.}$, are related to the separation energy, Q_s, via: $E=T_{c.m.}+Q_s$.) The efficiency functions for our hodoscope were determined by detailed Monte Carlo calculations. These calculations take into account the precise geometry of the hodoscope, the angular straggling in the target, the measured detector energy resolutions, and the constraints on the particle energies. The decays of the parent nuclei were assumed to be isotropic in their center-of-mass frames. The laboratory energy spectra and angular distributions of the parent nuclei were described by simple moving-source parametrizations (see Chapter 5).

In cases where stable parent nuclei exist (e.g. α-particles and ^{6}Li nuclei) these parametrizations were constrained to reproduce the experimental distributions. For parent nuclei with particle unstable ground states (e.g. ^{5}Li, ^{8}Be) source parameters of neighboring stable nuclei (α, ^{6}Li and ^{7}Li) were used (see Chapter 7 and 8). This procedure may be justified by the similarity of the source parameters for different fragments (see Chapter 5). Since emission temperatures were determined from the relative populations of states, only relative efficiencies had to be known. The extracted emission temperatures are, therefore, not very sensitive to details of the parent distributions (see Chapter 7 and 8).

In principle, the formal width of the level $\Gamma_i = 2 \cdot P_{\ell i} \gamma_i^2$ and the resonance energy $E_i = E_R + \Delta_{\ell i}$ are functions of the excitation energy, E. Their energy dependence is expressed in terms of the penetrability, $P_{\ell i}$, and shift function, $\Delta_{\ell i}$. Since we want to extract the yields over the range of energies which enclose the resonant states, the integration should not, to the first order, sensitive to the detailed shape of the states. Unless stated, we set $\Delta_{\ell i}=0$ and disregard the energy dependence of Γ_i; in all cases, the branching ratio, $\Gamma_{c,i}/\Gamma_i$, is assumed to be energy independent.

The spectroscopic information for the energy levels used to extract temperatures is listed in Table 4. In cases where penetrability effects are included [Lane 1958], the resonance energy, E_r, the reduced width, γ^2, the interaction distance, a, and the relative orbital angular momentum, ℓ, are listed.

TABLE 4

Spectroscopic information for energy levels which were used to extract emission temperatures.

nucleus	E^* [MeV]	Γ [keV]	J^π	c	Γ_c/Γ [%]	E_r [MeV]	a [fm]	γ^2 [keV]	ℓ
^{4}He	20.1	200	0^+	p-t	100	0.5	4.57	2000	0
	21.1	1000	0^-	p-t	50	1.28	4.00	2800	1
	22.1	1000	2^-	p-t	50	2.24	4.00	4500	1
^{5}Li	g.s.	1500	$3/2^-$	p-α	100	1.637	7.0	646	1
	7.5	5000	$1/2^-$	p-α	100	--	--	--	--
	16.66	300	$3/2^+$	d-^{3}He	86	0.45	7.0	780	0
^{6}Li	2.186	24	3^+	d-α	100	--	--	--	--
	4.312	1320	2^+	d-α	96.7	--	--	--	--
	5.65	1900	1^+	d-α	74	--	--	--	--
^{8}Be	g.s	6.8eV	0^+	α-α	100	0.092	4.57	450	0
	3.04	1500	2^+	α-α	100	2.94	5.35	580	2
	11.4	3500	4^+	α-α	100	11.4	5.40	850	4
	17.64	10.7	1^+	p-^{7}Li	100	--	--	--	--
	18.15	138	1^+	p-^{7}Li	96[#]	--	--	--	--
	18.91	48	2^-	p-^{7}Li	50	--	--	--	--
	19.07	270	3^+	p-^{7}Li	100	--	--	--	--
	19.24	230	3^+	p-^{7}Li	50	--	--	--	--
	19.40	650	1^-	p-^{7}Li	50	--	--	--	--
	19.86	700	4^+	p-^{7}Li	4	--	--	--	--

[#] Γ_c/Γ = 0.04 for ^{8}Be → p + ^{7}Li$^*_{0.478}$ [Ajze 1987].

CHAPTER 5. SINGLE PARTICLE INCLUSIVE CROSS SECTIONS

The differential cross sections presented in this section have an uncertainty of the absolute normalization of about 15%. The error bars in Figures V.1-V.4 show only statistical uncertainties.

In reactions at low energies, energy spectra for particles emitted from compound nucleus are often described in terms of Maxwellian distributions, the slopes of which are closely related to the temperature of the emitting compound nucleus [Weis 1937]. In nucleus-nucleus collisions at intermediate energies, particle emission becomes significant already at the early stages of the reaction [Awes 1981a, Back 1980]. For the present reactions, the single particle energy spectra could not be described by a single emitting source over the entire angular range. In order to bring these data into context with previous measurements and to provide extrapolations to unmeasured scattering angles and particle energies, the data were fitted by a parametrization employing the superposition of Maxwellian distributions ("moving sources"):

$$\frac{d^2\sigma}{d\Omega dE} = \sum_i N_i \sqrt{E-V_c} \cdot \exp\left(-[E-V_c+E_i-2\sqrt{E_i(E-V_c)}\cdot\cos\Theta]/\tau_i\right) . \qquad (V\text{-}1)$$

Here, V_c is the kinetic energy gained by the Coulomb repulsion from the heavy reaction residue assumed to be stationary in the laboratory

system; N_i is a normalization constant; τ_i is the "kinetic temperature" parameter of the i-th source; $E_i = \frac{1}{2}mv_i^2$, where m is the mass of the emitted particle and v_i is the velocity of the i-th source in the laboratory system.

5.1 $^{14}N + ^{197}Au$ at E/A = 35 MeV

Single particle inclusive cross sections for light particles (p, d, t, α) are shown in Fig. V.1. These cross sections exhibit the characteristic features established for a large number of heavy ion induced reactions at intermediate energies (see [Gelb 1987] for a recent review). At forward angles, the energy spectra exhibit a broad maximum located close to the beam velocity. This peak could be attributed to peripheral break-up reactions. At larger angles, the energy spectra exhibit rather structureless, nearly exponential slopes which are considerably less steep than expected for compound nucleus evaporation. Qualitatively, similar energy spectra were observed for the emission of Li and Be fragments, see Figures V.2-V.3.

In order to reduce the number of free parameters, the parameters of one source were kept fixed at v_1=0.0185c and T_1=5 MeV. These parameters are consistent with evaporation from fully equilibrated heavy reaction residues formed in incomplete fusion reactions. This "compound-like" source contributes significantly at backward angles. The remaining parameters were fit to the data. A fast, "projectile-like" source is responsible for the structures at forward angles. The resulting fits are shown by the solid lines in Figures V.1-V.3; the parameters are listed in Table 5. In addition to the slow, "target-like", and fast, "projectile-like", sources, an intermediate rapidity source is required

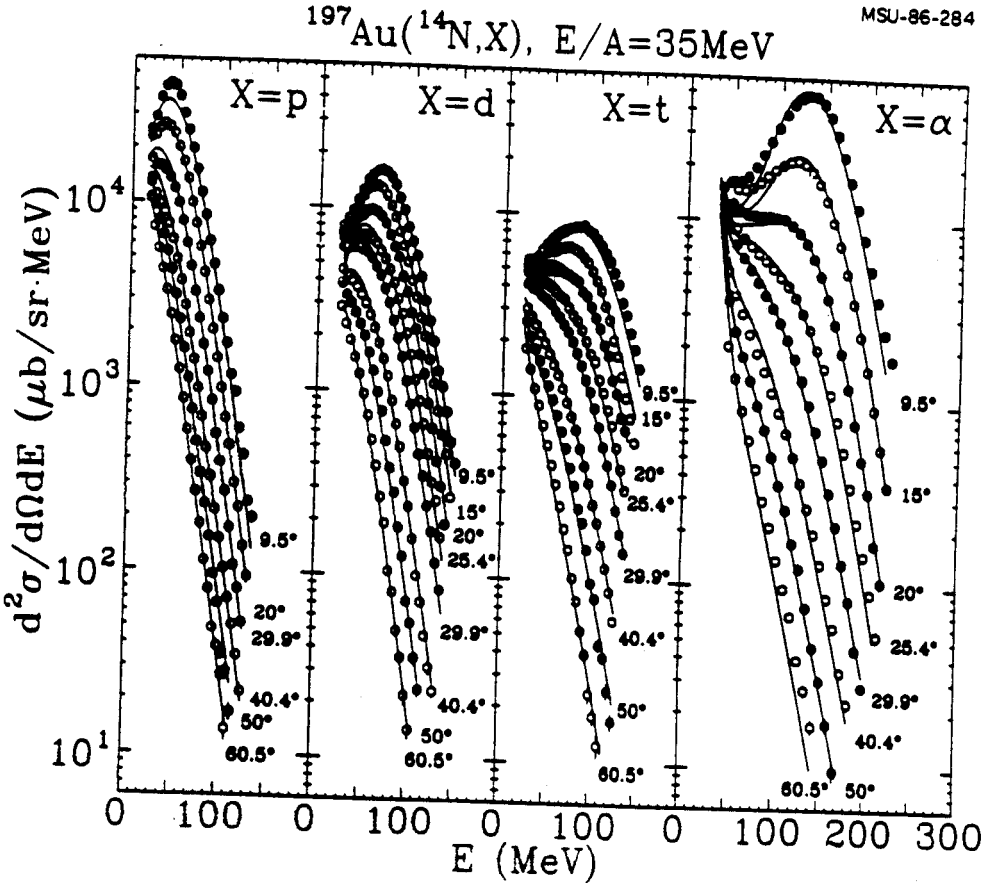

Figure V.1 Differential cross sections for p, d, t, and α-particles. The solid curves show fits with Eq. V.1. The fit parameters are listed in Table 5.

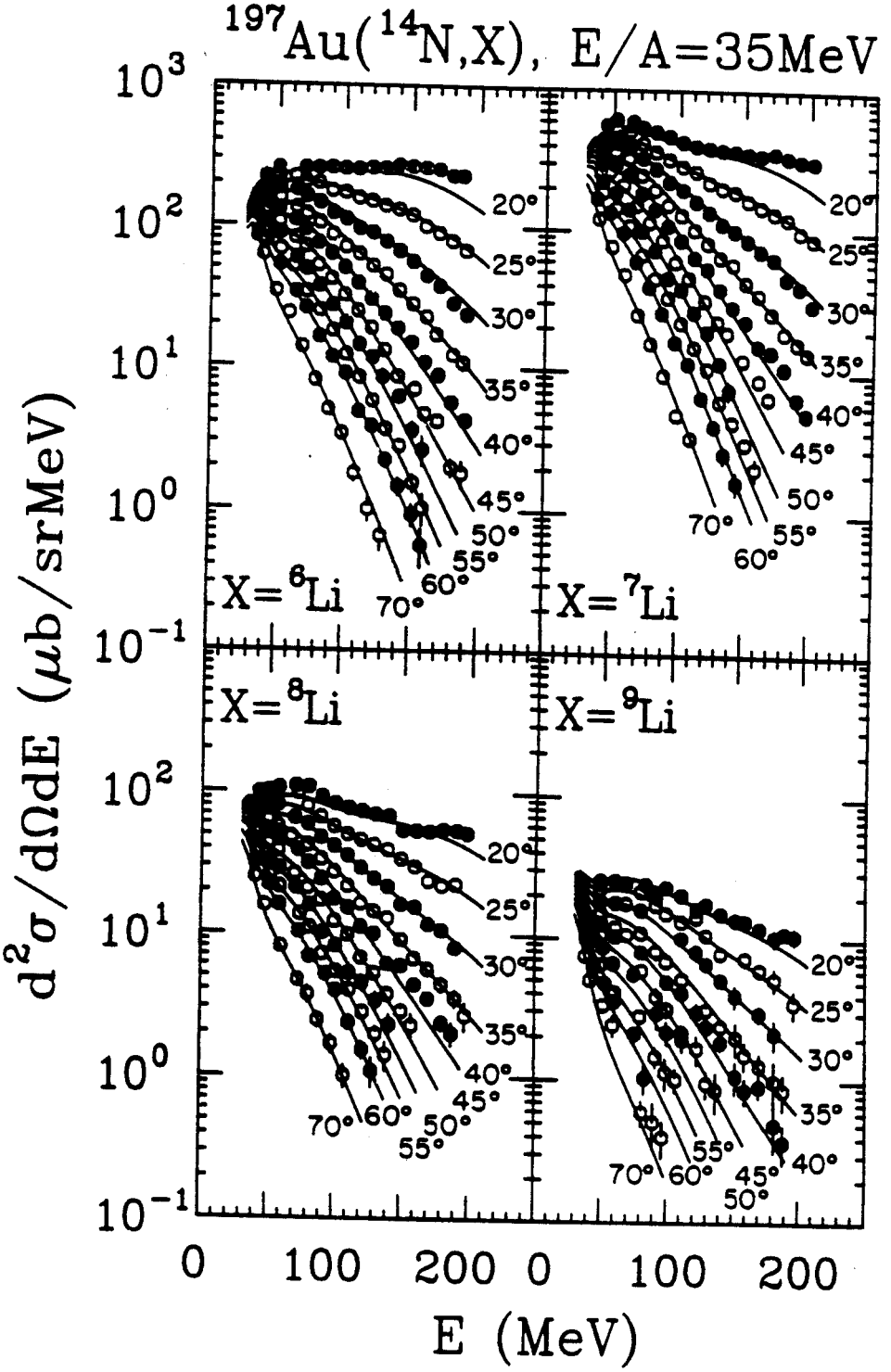

Figure V.2 Differential cross sections for lithium isotopes. The solid curves show fits with Eq. V.1. The fit parameters are listed in Table 5.

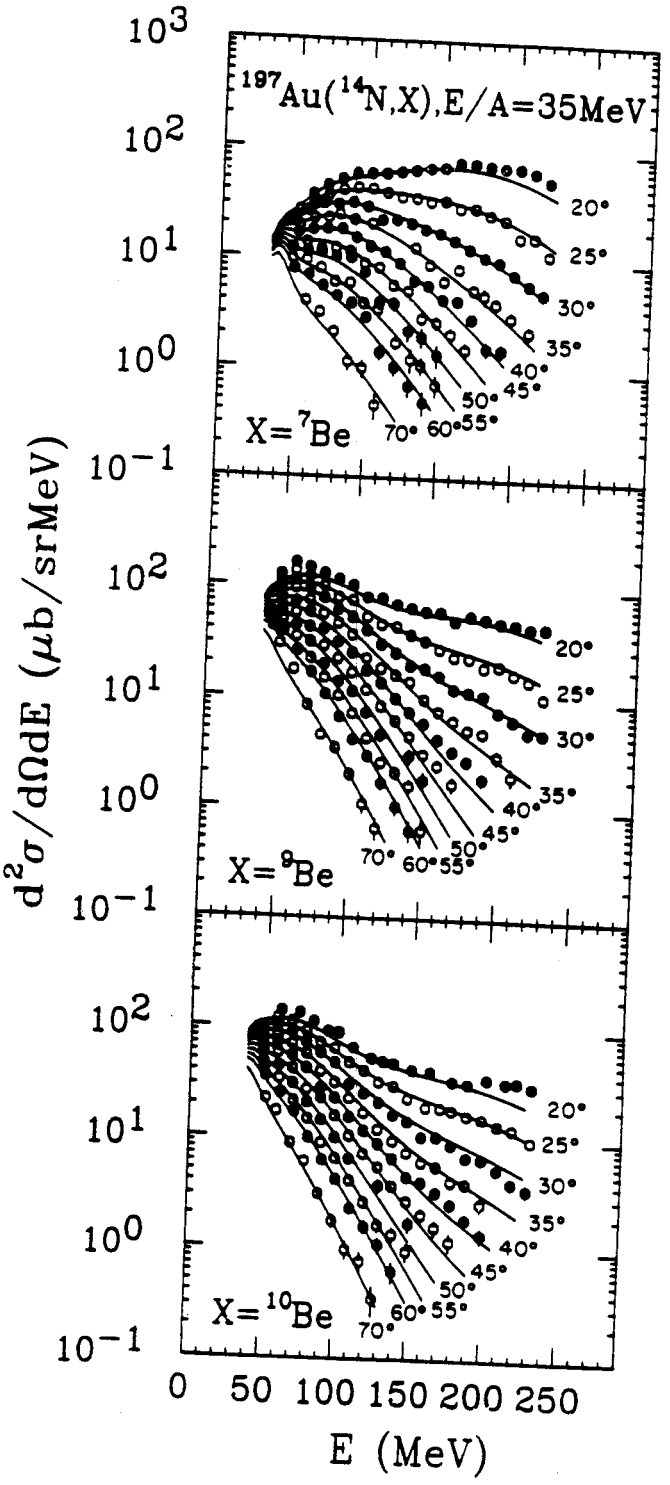

Figure V.3 Differential cross sections for beryllium isotopes. The solid curves show fits with Eq. V.1. The fit parameters are listed in Table 5.

TABLE 5

Parameters of Eq. V.1 used to fit the single particle inclusive cross sections for the reaction $^{14}N + ^{197}Au$ at E/A = 35 MeV shown in Figures V.1-V.3

Part.	V_c [MeV]	τ_1 [MeV]	v_1/c	N_1 [a.u.]	τ_2 [MeV]	v_2/c	N_2 [a.u.]	τ_3 [MeV]	v_3/c	N_3 [a.u.]
p	9.9	5	0.0185	4581	10.0	0.118	5275	5.5	0.248	4990
d	9.6	"	"	1764	10.5	0.122	2131	6.3	0.227	2046
t	9.3	"	"	2794	11.5	0.125	1216	6.4	0.223	901
α	18.1	"	"	24040	11.9	0.123	2514	4.7	0.234	8491
^{6}Li	26.1	"	"	83.7	14.5	0.099	49.5	12.0	0.210	59.9
^{7}Li	25.8	"	"	169	13.6	0.086	115	12.7	0.197	86.6
^{8}Li	25.5	"	"	38.0	14.8	0.084	19.6	12.8	0.190	14.9
^{9}Li	25.4	"	"	14.6	13.2	0.087	5.72	13.3	0.174	2.67
^{7}Be	34.1	"	"	8.95	15.7	0.111	9.35	10.2	0.210	25.7
^{9}Be	33.4	"	"	29.3	13.5	0.077	27.6	12.7	0.188	16.4
^{10}Be	33.2	"	"	32.3	12.8	0.069	27.1	15.6	0.166	7.70

to fit the cross sections at large transverse momenta. For light particles (p, d, t, α), the temperature parameters for this source agree with the systematic trends established previously [Awes 1981, West 1982] (see also Figure V.5 shown below).

5.2 ^{16}O + ^{197}Au at E/A = 94 MeV

Single particle inclusive cross sections for light particles (p, d, t, ^3He, α, ^6Li) are shown in Figure V.4. In this experiment, a small angular range was covered, θ = 39.5°-50.5°, and the spectra can be described in terms of two moving sources, since contributions from projectile-like sources are negligible at these large angles. Because of the small angular range, substantial ambiguities exist for the source velocity parameters and for the kinetic temperature parameter, τ_2, of the low-velocity (target like) sources. The kinetic temperature parameters, τ_1, of the intermediate rapidity sources, on the other hand, are rather well determined. For light particles (p, d, t, α), the kinetic energy temperature parameters, $\tau_1 \approx 18$-20 MeV, of the intermediate rapidity source agree with the systematic trends established previously [Awes 1981, West 1982] (see also Figure V.5 shown below).

5.3 Discussion

Single particle inclusive cross sections for light particles can be rather well described in terms of the superposition of a few Maxwellian distributions (moving sources). Except at most forward and backward angles, the cross section can be described in terms of a source centered at a velocity slightly less than half the beam velocity. A "projectile-like" and a "target-like" source simulating emissions from projectile

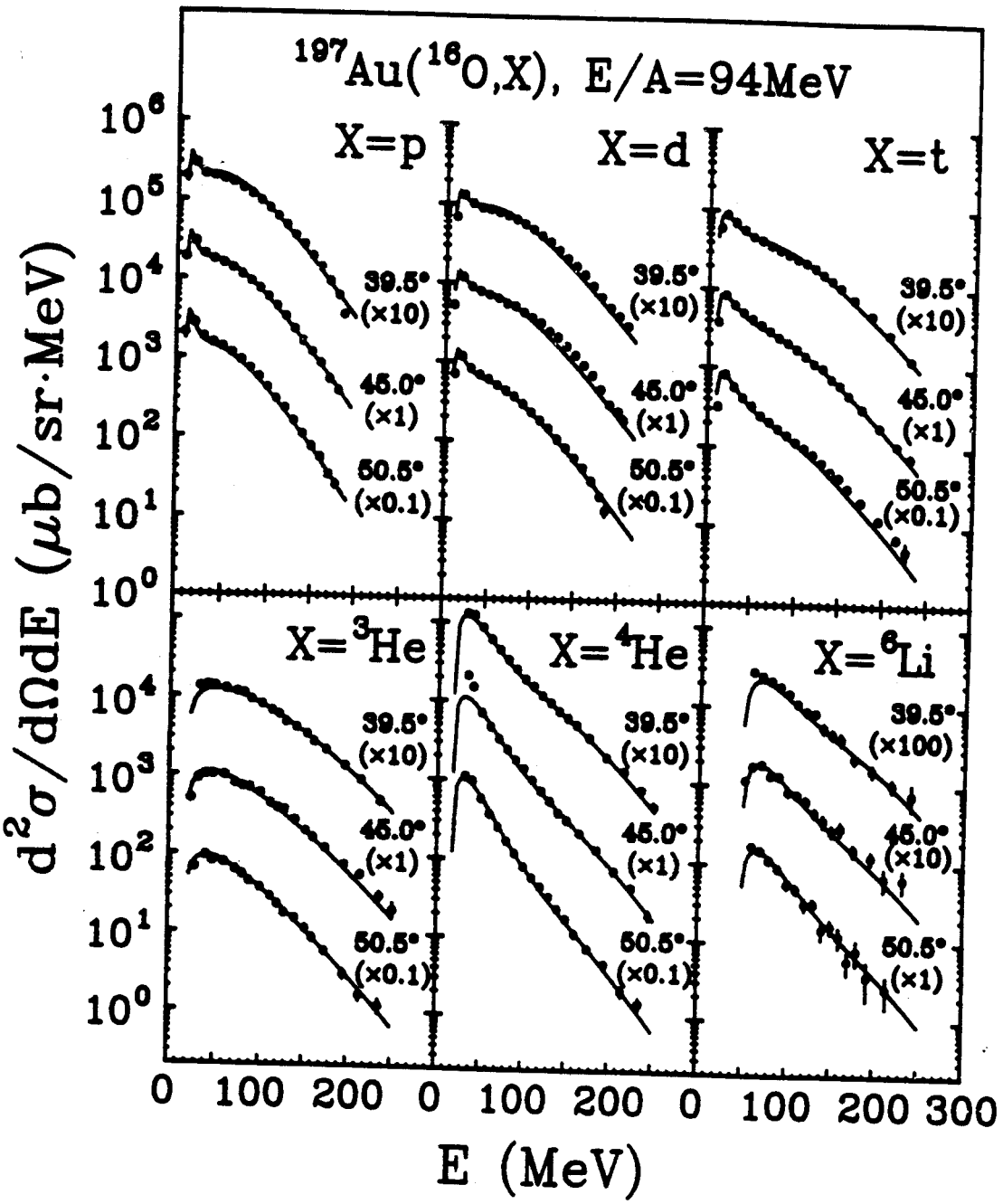

Figure V.4 Single particle inclusive cross sections for p, d, t, ^{3}He, α, and ^{6}Li nuclei emitted in ^{16}O induced reactions on ^{197}Au at E/A=94 MeV at the laboratory angles of 39.5°, 45°, 50.5°. The curves are two-source fits with Eq. V.1; the parameters are listed in Table 6.

TABLE 6

Parameters of Eq. V.1 used to fit the single particle inclusive cross section for the reaction $^{16}O + ^{197}Au$ at E/A=94 MeV shown in Figure V.4. The normalization constants N_1 and N_2 are given in $[\mu b/(sr \cdot MeV^{3/2})]$.

Part.	V_C(MeV)	τ_1(MeV)	v_1/c	N_1	τ_2(MeV)	v_2/c	N_2
p	9.8	18.3	0.24	7850	4.8	0.002	36100
d	9.4	20.4	0.19	3360	6.6	0.000	11160
t	9.2	20.6	0.19	1635	11.2	0.000	5450
^{3}He	18.2	20.2	0.23	370	21.4	0.07	311
α	17.9	18.1	0.19	1008	13.0	0.047	5040
^{6}He	32.7	18.0	0.12	28.7	9.4	0.053	107
^{6}Li	48.4	19.6	0.15	30.2	12.1	0.068	83
^{7}Li	47.9	17.4	0.15	45.2	12.0	0.074	149

fragments and target residues are needed to make a complete description over the entire angular range. In a simple dynamical picture, these sources might be associated with different stages of emission as the reaction evolves [Frie 1983].

The kinetic temperatures of intermediate rapidity sources show a systematic dependence on the incident energy per nucleon as shown in Figure V.5. For the reaction induced by ^{14}N on ^{197}Au at E/A=35 MeV, the temperatures range from 10 to 12 MeV; for ^{16}O induced reaction on ^{197}Au at E/A=94 MeV, they lie between 17 and 20 MeV. The systematic incident energy dependence of the kinetic temperature parameters of the intermediate rapidity sources and the similarity of the parameters extracted for different light particles (p, d, t, ...) raise the interesting question whether these emissions can be explained in terms of a nearly equilibrated source formed in the region of overlap between projectile and target. Of particular interest are the questions of the possible spatial localization of the emitting source and the possible attainment of chemical equilibrium. These questions will be addressed in later chapters.

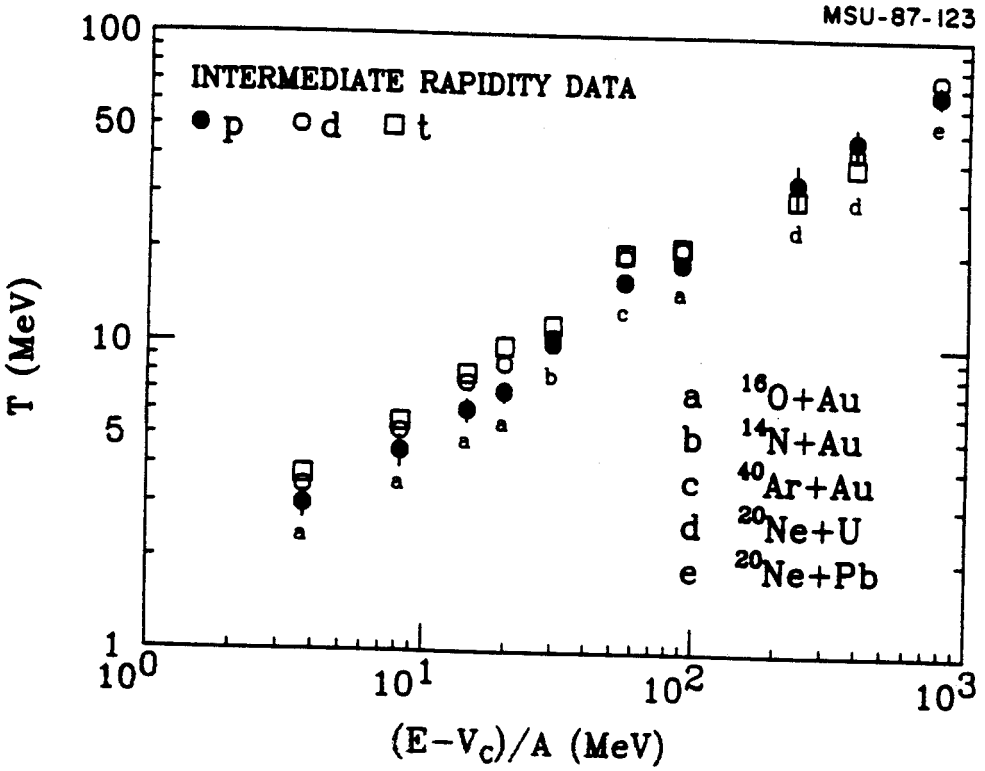

Figure V.5 Kinetic temperature parameters of intermediate rapidity sources as extracted from fits of single particle inclusive cross sections with Maxwellian distributions (see Eq. V.1); data are also from [Awes 1981, West 1982, Poch 1987].

CHAPTER 6. INCLUSIVE TWO-PARTICLE CORRELATION FUNCTIONS

Two particle correlation functions measured for different incident energies and at different average angles will be discussed in this chapter. In the first two sections, structures in the two particle correlation functions, measured in the experiment ^{16}O + ^{197}Au at E/A=94 MeV and ^{14}N + ^{197}Au at E/A=35 MeV, will be shown and explained. Systematic comparisons as well as their implication will be discussed in the last section.

6.1 ^{16}O + ^{197}Au at E/A = 94 MeV

Figure VI.1 shows the measured p-p correlation function, normalized in the relative momentum range of q≈70-100 MeV/c. These correlation functions are constrained by the total kinetic energy of the coincident protons, E_1+E_2, as indicated in the figure. The attractive singlet S-wave interaction between the two coincident protons gives rise to a pronounced maximum in the correlation function at q≈20 MeV/c. This maximum becomes larger with increasing total kinetic energies of the coincident protons. Similar observations have been made previously [Lync 1983]. This energy dependence of correlation functions indicates that more energetic particles are emitted from sources which are more localized in space-time. A qualitative scale is provided by the dashed

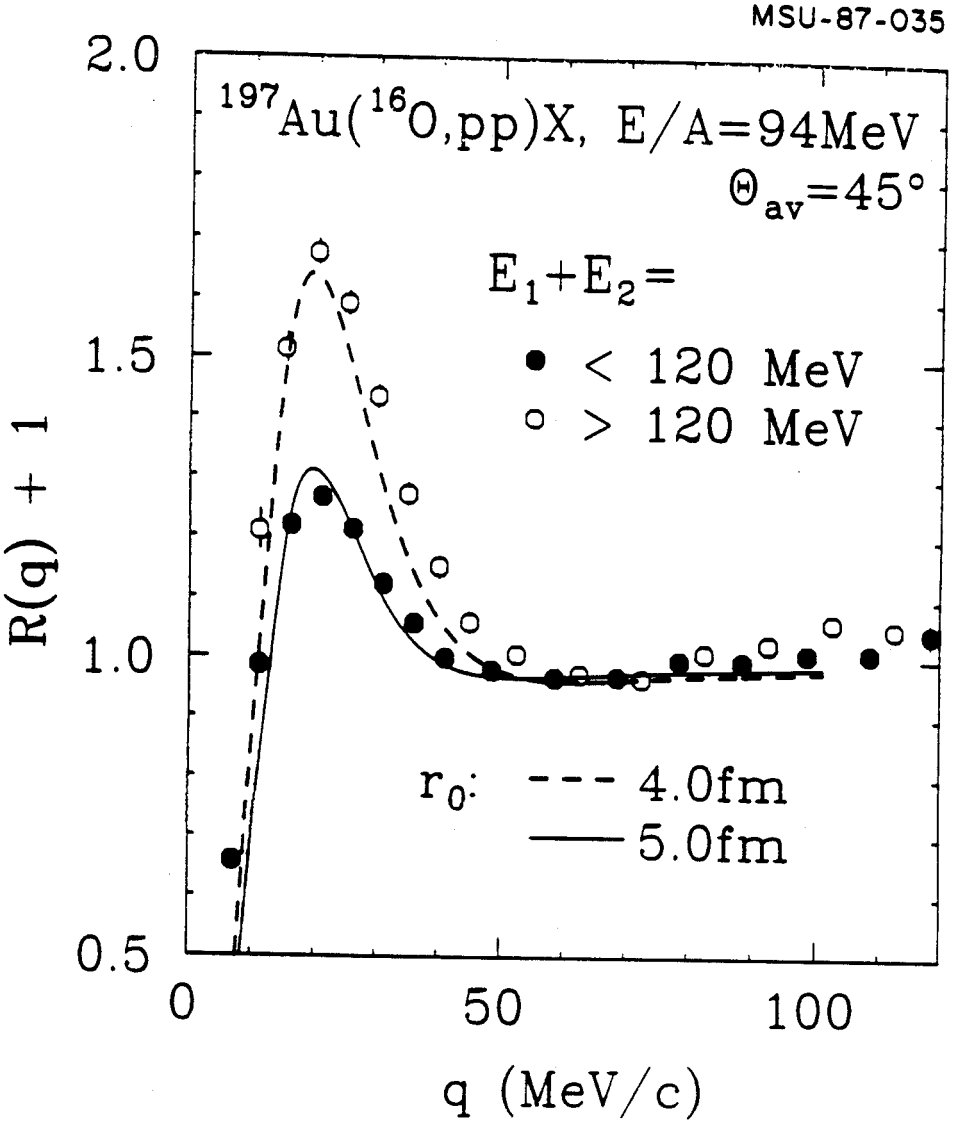

Figure VI.1 p-p correlation functions measured for ^{16}O induced reactions on ^{197}Au at E/A=94 MeV and an average emission angle of Θ_{av}=45°. The constraints on the total kinetic energy, E_1+E_2, of the two coincident particles are indicated in the figure. The curves show calculations with Eq. II.12.

and solid curves which represent theoretical correlation functions predicted by Eq. II.12 for r_o = 4 and 5 fm, respectively.

Two-deuteron correlation functions are shown in Figure VI.2. They are normalized in the range of q≈120-150 MeV/c. At low relative energies, the deuteron-deuteron interaction is repulsive and does not contain any resonant contribution. As a consequence, two-deuteron correlation functions exhibit only a minimum at small relative momenta [Chit 1985, Poch 1986a, Poch 1987]. Consistent with previous measurements [Poch 1986a, Poch 1987], this minimum becomes more pronounced with increasing total kinetic energy of the coincident particles. The solid and dashed curves show theoretical correlation functions predicted with the final state interaction model [Chit 1985]. The extracted source dimensions are larger than those extracted from correlation functions for particle pairs for which the mutual interaction exhibits resonant behavior.

Figure VI.3 shows measured α-d correlation functions which exhibit a sharp peak due to the 2.186 MeV state in ^{6}Li ($J^\pi=3^+$, Γ=24 keV, $\Gamma_\alpha/\Gamma_{tot}$= 1.00) and a broad peak due to the overlapping states at 4.31 MeV ($J^\pi=2^+$, Γ=1.3 MeV, $\Gamma_\alpha/\Gamma_{tot}$= 0.97) and 5.65 MeV ($J^\pi=1^+$, Γ=1.9 MeV, $\Gamma_\alpha/\Gamma_{tot}$=0.74). The normalization is performed over the range q≈125-150 MeV/c. Consistent with previous measurements [Chit 1986a, Poch 1987] and with the qualitative trend of the p-p correlation functions shown in Figure VI.1, these peaks increase in magnitude for more energetic α-d pairs. Theoretical correlation functions calculated from the final state interaction model [Boal 1986] are shown by the solid and dashed curves. Because of the narrow width of the 2.186 MeV state in ^{6}Li, the theoretical α-d correlation function was corrected for the finite

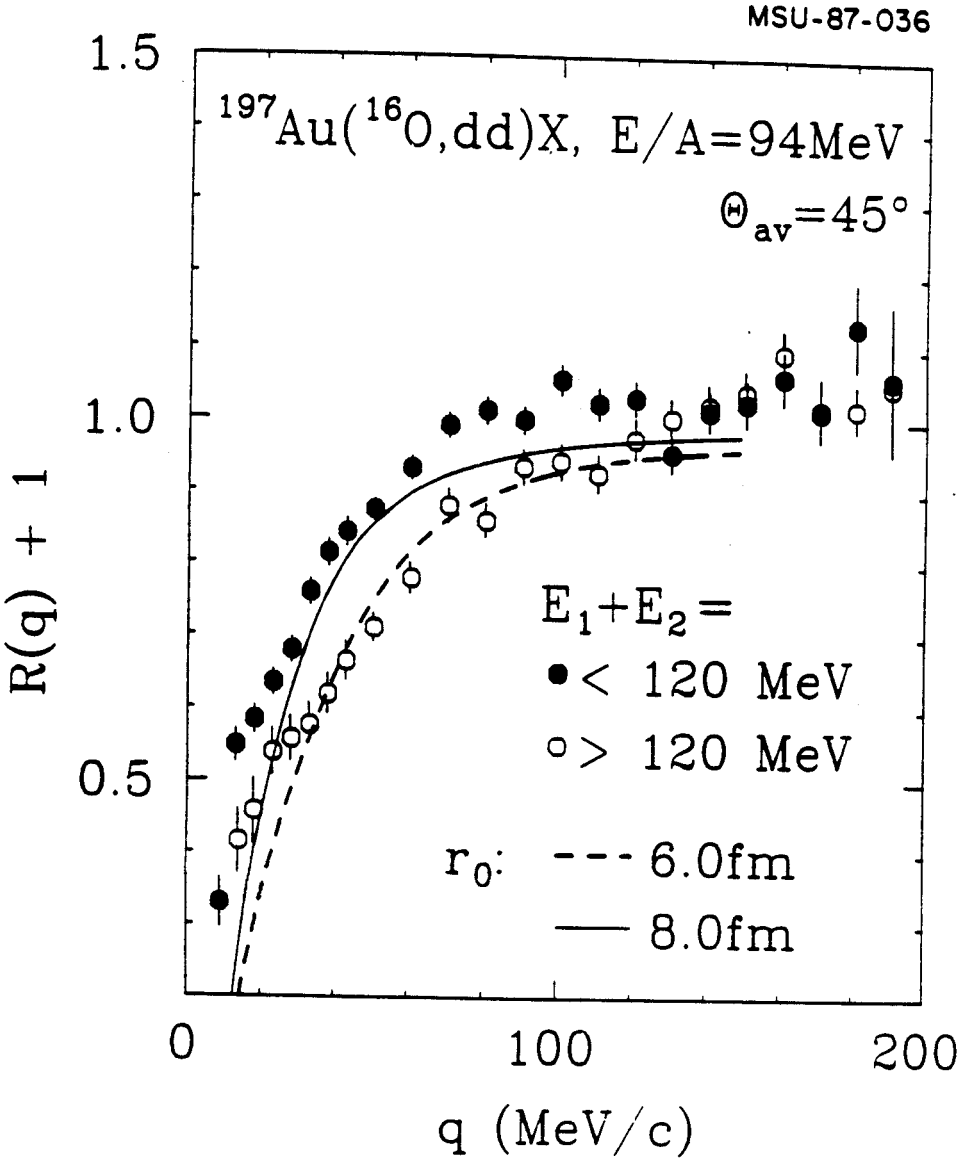

Figure VI.2 d-d correlation functions measured for ^{16}O induced reactions on ^{197}Au at E/A=94 MeV and an average emission angle of Θ_{av}=45°. The constraints on the total kinetic energy, E_1+E_2, of the two coincident particles are indicated in the figure. The curves show calculations with Eq. II.12.

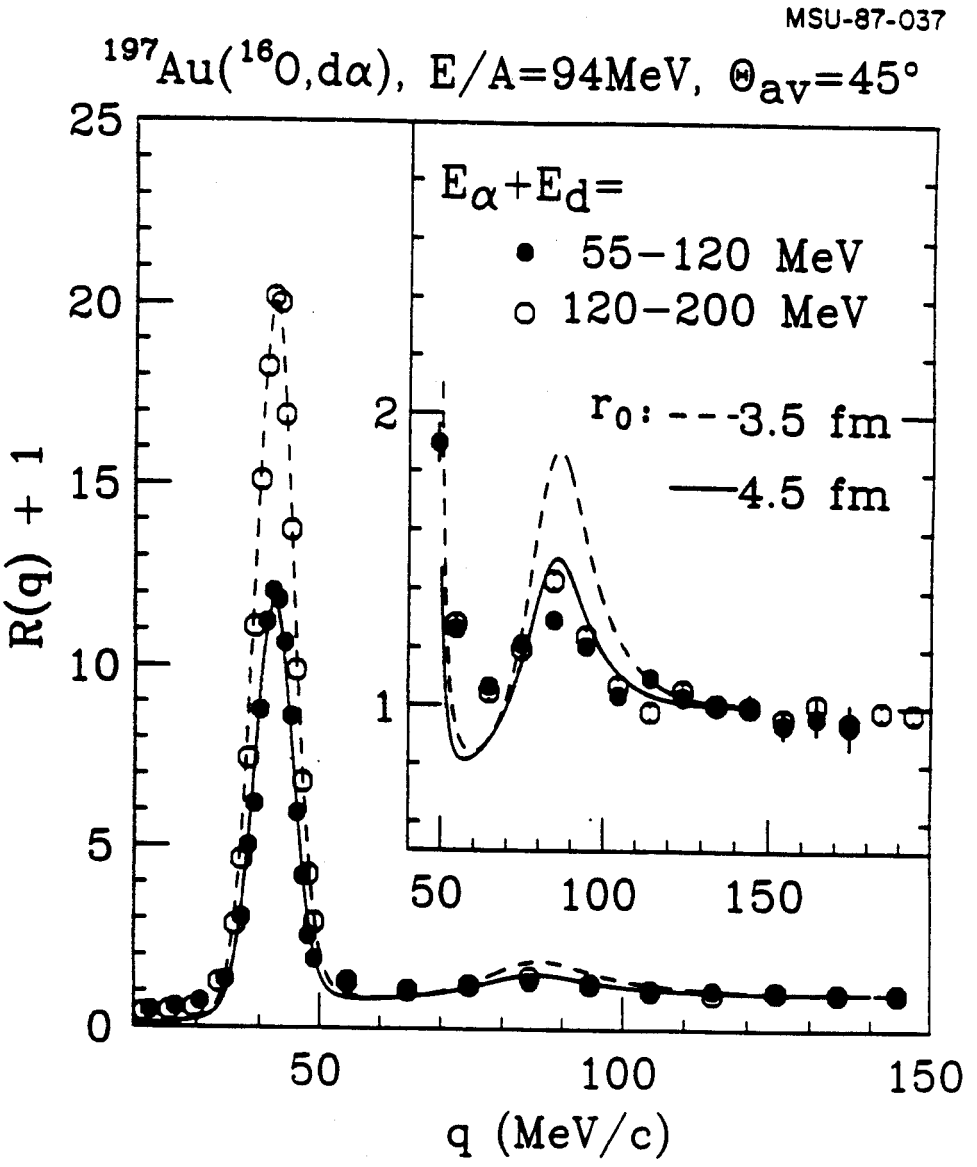

Figure VI.3 α-d correlation functions measured for ^{16}O induced reactions on ^{197}Au at E/A=94 MeV and an average emission angle of Θ_{av}=45°. The constraints on the total kinetic energy, E_1+E_2, of the two coincident particles are indicated in the figure. The curves show calculations with Eq. II.12.

resolution of the hodoscope by folding the original calculation with a Gaussian of appropriate width. Such corrections are of minor importance for other correlation functions, since the widths of the states are usually larger than the resolution of the apparatus. Because of this correction, source radii were extracted from the integral α-d correlation, $R_{eff} = \int dq \cdot R(q)$, with the integration performed over the range of q≈30-60 MeV/c. This procedure also reduces the sensitivity of the extracted source radii to uncertainties of the experimental line shape. Source radii extracted from the broad peak of the α-d correlation function at q≈85 MeV/c are larger by about 1 fm than those extracted from the sharp peak at q≈42 MeV/c; such discrepancies have been noted previously [Poch 1986, Chen 1987]. At present, they are not yet understood.

The p-t correlation function, shown in Figure VI.4, exhibits two maxima, corresponding to the known states in ^{4}He: the $J^\pi = 0^+$ state at 20.1 MeV (Γ_p/Γ = 1.00 [Fiar 1973]) and the two overlapping $J^\pi = 0^-$ and 2^- states at 21.1 and 22.1 MeV [Fiar 1973] ($\Gamma_p \approx \Gamma_n$ [Bari 1971]), respectively. Apart from the energy threshold, no further constraint was applied for these data. The correlation function was normalized over q=150-200 MeV/c.

Figure VI.5 shows the measured p-α (left) and d-^{3}He (right) correlation functions. The p-α correlation function, normalized at q=125-150 MeV/c, exhibits a broad peak near q≈50 MeV/c which is related to the resonant interaction of the unbound ground state in ^{5}Li ($J^\pi = \frac{3}{2}^-$, $\Gamma \approx 1.5$ MeV, Γ_p/Γ = 1.00). The small shoulder at q ≈ 15 MeV/c is not related to a resonance in the mass five system. It results [Poch 1985c] from the decay ^{9}B → 2α + p of the particle unstable ^{9}B ground state. The

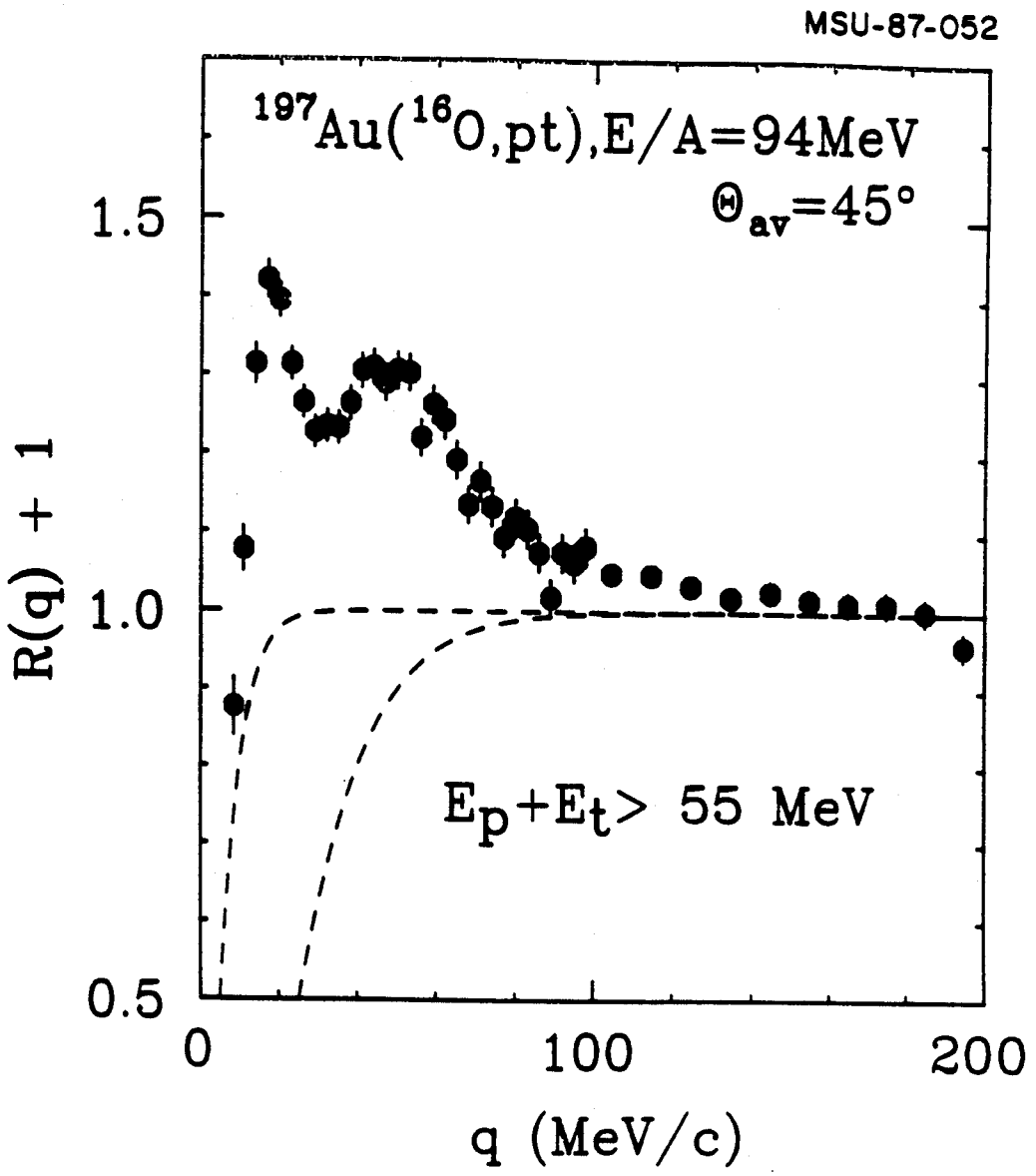

Figure VI.4 p-t correlation function for ^{16}O induced reactions on ^{197}Au at E/A=94 MeV and $\Theta_{av}=45°$. The background correlation function was assumed to lie between the extremes indicated by the dashed lines.

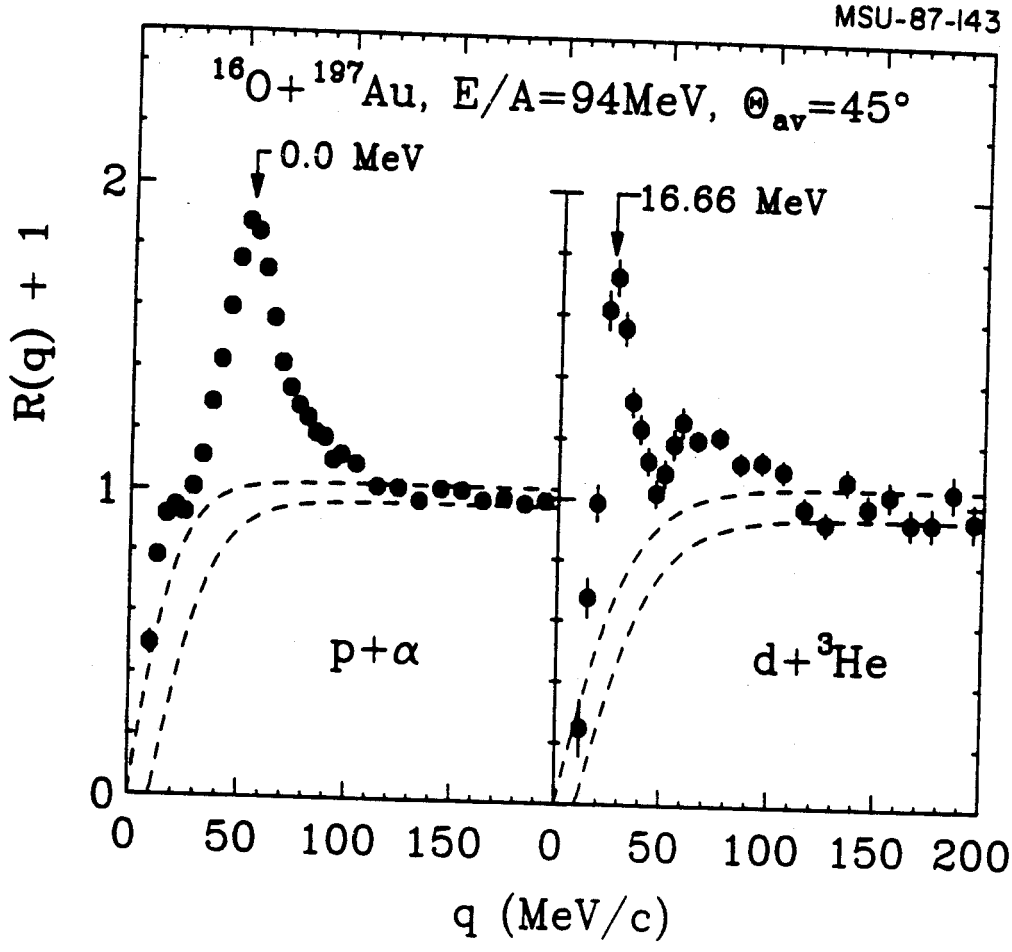

Figure VI.5 p-α (left hand panel) and d-^{3}He (right hand panel) correlation functions for ^{16}O induced reactions on ^{197}Au at E/A=94 MeV and Θ_{av}=45°. The background correlation function was assumed to lie between the extremes indicated by the dashed lines. The correlation functions are shown for $E_1+E_2 \geq 55$ MeV.

largest peak in the d-^{3}He correlation function, normalized at q=125-150 MeV/c, corresponds to the decay of the 16.66 MeV state in ^{5}Li ($J^\pi = \frac{3}{2}^+$, $\Gamma \approx 0.3$ MeV, $\Gamma_d/\Gamma = 0.86$). The other two states, located at 18 and 20 MeV respectively, show their existence by a broad structure in the momentum range between 40 and 90 MeV/c. The properties of these states are not well known.

Figure VI.6 shows the p-^{7}Li (left) and α-α (right) correlation functions, normalized respectively at q=100-150 MeV/c and q=300-350 MeV/c. Because of the relatively large angular separation between adjacent detectors, the well known particle unbound ground state of ^{8}Be is not seen in the α-α correlation function. The peak at q ≈ 105 MeV/c in the α-α correlation function corresponds to the decay of the 3.04 MeV state [Ajze 1984] in ^{8}Be ($J^\pi = 2^+$, Γ = 1.5 MeV, Γ_α/Γ = 1.00). The pronounced structure at q≈50 MeV/c is not directly associated with a state in ^{9}Be. It is caused by the decay of the 2.43 MeV state in ^{9}Be [Chri 1966, Poch 1987]. In addition, it contains contributions from the "ghost peak" of the ^{8}Be ground state [Becc 1981]. The p-^{7}Li correlation function exhibits several sharp structures resulting from the decay of high lying states in ^{8}Be at excitation energies of 17.64 MeV ($J^\pi = 1^+$, Γ = 0.01 MeV, $\Gamma_p/\Gamma_{tot} = 1.00$) and higher.

From the comparison of measured and calculated correlation functions, source radii can be extracted. They are summarized in Table 7.

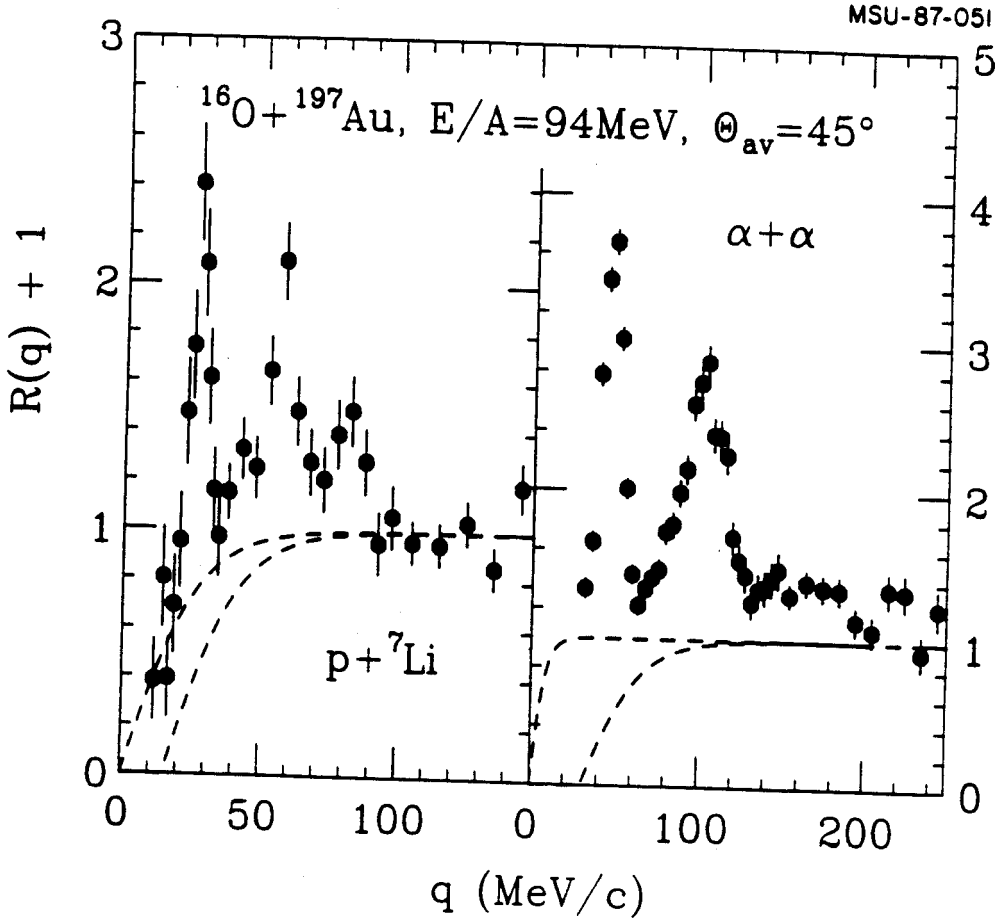

Figure VI.6 p-^{7}Li (left hand panel) and α-α (right hand panel) correlation functions for ^{16}O induced reactions on ^{197}Au at E/A=94 MeV and Θ_{av}=45°. The background correlation function was assumed to lie between the extremes indicated by the dashed lines. The correlation functions are shown for $E_1+E_2 \geq 80$ MeV.

TABLE 7

Source radii extracted from the reaction

$^{16}O + {}^{197}Au$ at E/A=94 MeV

	E_1+E_2(MeV)	r_o (fm)
p-p	30 -80	5.5
p-p	80 -150	4.6
p-p	150-200	3.8
p-p	200-300	3.2
d-d	30 -80	11.
d-d	80 -150	6.3
d-d	150-200	6.0
d-α	55 -120	4.5
d-α	120-200	3.5

6.2 $^{14}N + {}^{197}Au$ at E/A = 35 MeV

The structures of the correlation functions measured for the $^{14}N + {}^{197}Au$ reaction at E/A=35 MeV are qualitatively similar to those measured for the $^{16}O + {}^{197}Au$ at E/A=94 MeV (see previous section). Correlation functions measured for p-p, d-d, d-α are shown in Figure VI.7. The left and right panels show the correlation functions measured at the average detection angles of 35° and 50°, respectively. They are very similar and no significant dependence on average detection angle is observed. Apart from the particle energy thresholds, no further constraints were imposed. The p-α correlation function is dominated by the p-α resonance

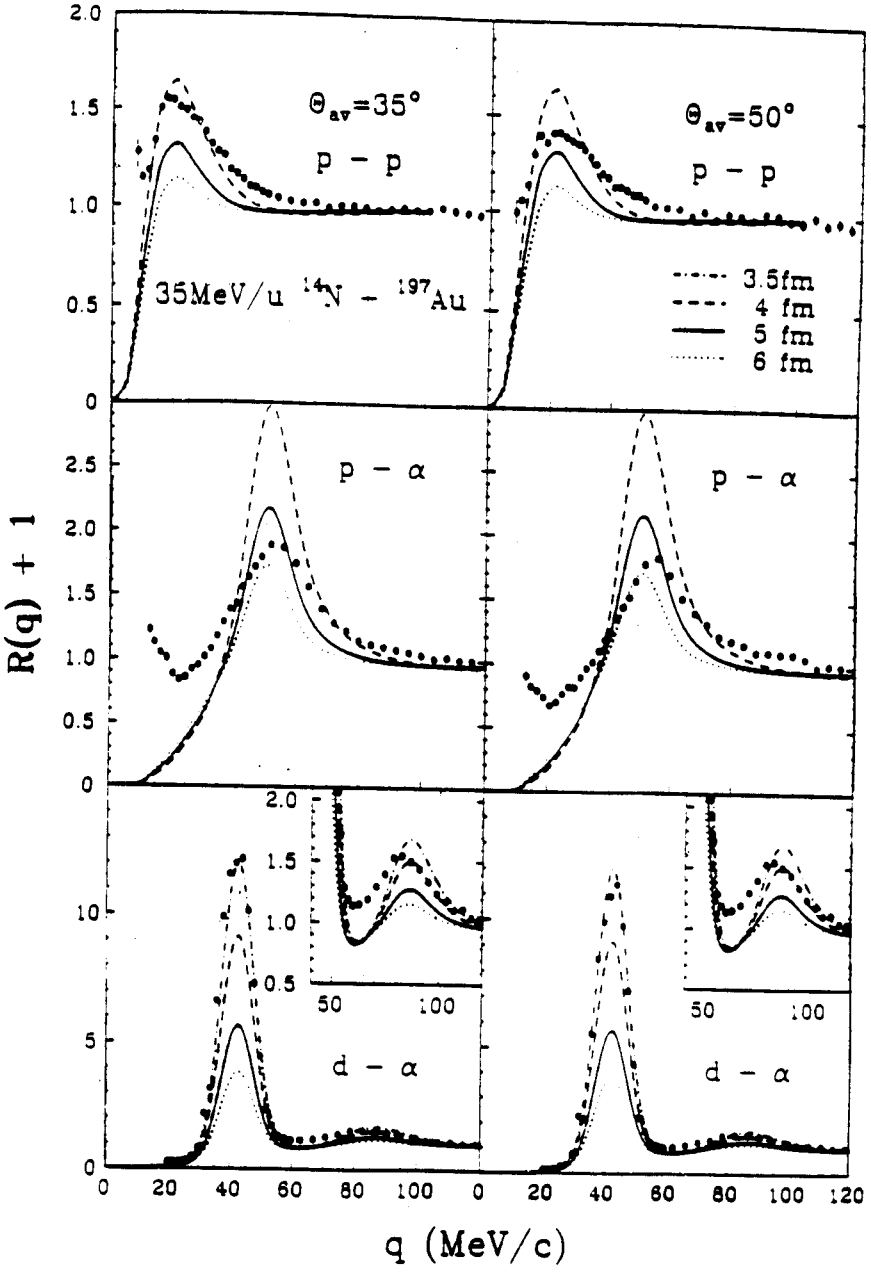

Figure VI.7 Inclusive p-p, p-α, and d-α correlation functions measured at Θ_{av}=35° and 50°. Apart from the energy thresholds, no constraints were applied to generate the experimental correlation functions. The theoretical correlation functions were calculated with the final-state interaction model, Eq. II.12.

corresponding to the ground state of ^{5}Li; its line shape is distorted at small relative momenta by the Coulomb interaction with the target-like residue. These distortions are particularly pronounced because of the different mass to charge ratios for the protons and the alpha particles [Poch 1985c]. The rise at small relative momenta, q≲25 MeV/c, is caused by contributions from the decay ^{9}B →2α+p [Poch 1985c].

Source radii extracted from the theoretical calculation of correlation functions, Eq. II.12, are listed in Table 8 [Poch 1986a].

TABLE 8

Source radii extracted from the reaction ^{14}N + ^{197}Au at E/A=35 MeV [Poch 1986a]

	E_1+E_2	35°	50°
p-p	24-50	4.9±0.5	5.2±0.5
p-p	50-75	4.3±0.3	4.0±0.3
p-p	75-100	3.8±0.2	3.6±0.2
d+d	30-80	8. ±2.	-
d+d	80-160	5.5±1	-
t+t	36-120	6.5±1	-
t+t	120-200	5.5±1	-
p+α	52-100	6.0±0.5	6.0±0.5
p+α	100-150	5.0±0.5	4.8±0.3
p+α	150-200	4.0±0.5	3.7±0.3
d+α	55-100	3.8±0.2	3.9±0.2
d+α	100-150	3.0±0.2	2.8±0.2
d+α	150-220	3.0±0.2	2.7±0.2

6.3 DISCUSSION

Since different particle pairs and particles of different energies could be emitted at different stages of the reaction or for different ranges of impact parameters [Lync 1983, Boal 1986, Chit 1986b], the energy dependence of correlation functions measured for different particle pairs could provide interesting information about the time dependence of the disintegration process.

The dependence of extracted source radii on the total kinetic energy, E_1+E_2, of the two coincident particles is shown in Figure VI.8 for various particle combinations measured for $^{14}N + ^{197}Au$ reaction at E/A=35 MeV and $\Theta_{lab}=35°$. The horizontal bars indicate the gates placed upon the total kinetic energy, E_1+E_2. The normalization constants, C_{12}, in Eq. II.1 were taken as independent of these energy constraints. The vertical error bars include normalization uncertainties for the different energy gates which were evaluated by normalizing the experimental correlation functions to the calculations at large relative momenta. For orientation, the dashed horizontal lines mark the corresponding source dimensions of the projectile and target nuclei.

For particles emitted with high kinetic energies, the radii extracted from resonant interactions are larger than the size of the projectile nucleus but smaller than the size of target nucleus. For particles emitted with small kinetic energies, the source sizes exceed the target size. For all the particle combinations, the extracted apparent source radii decrease with increasing total kinetic energies of the emitted particles. This energy dependence has been observed in all experiments performed up to now. The observation supports the intuitive picture that the energetic particles are primarily emitted at the early

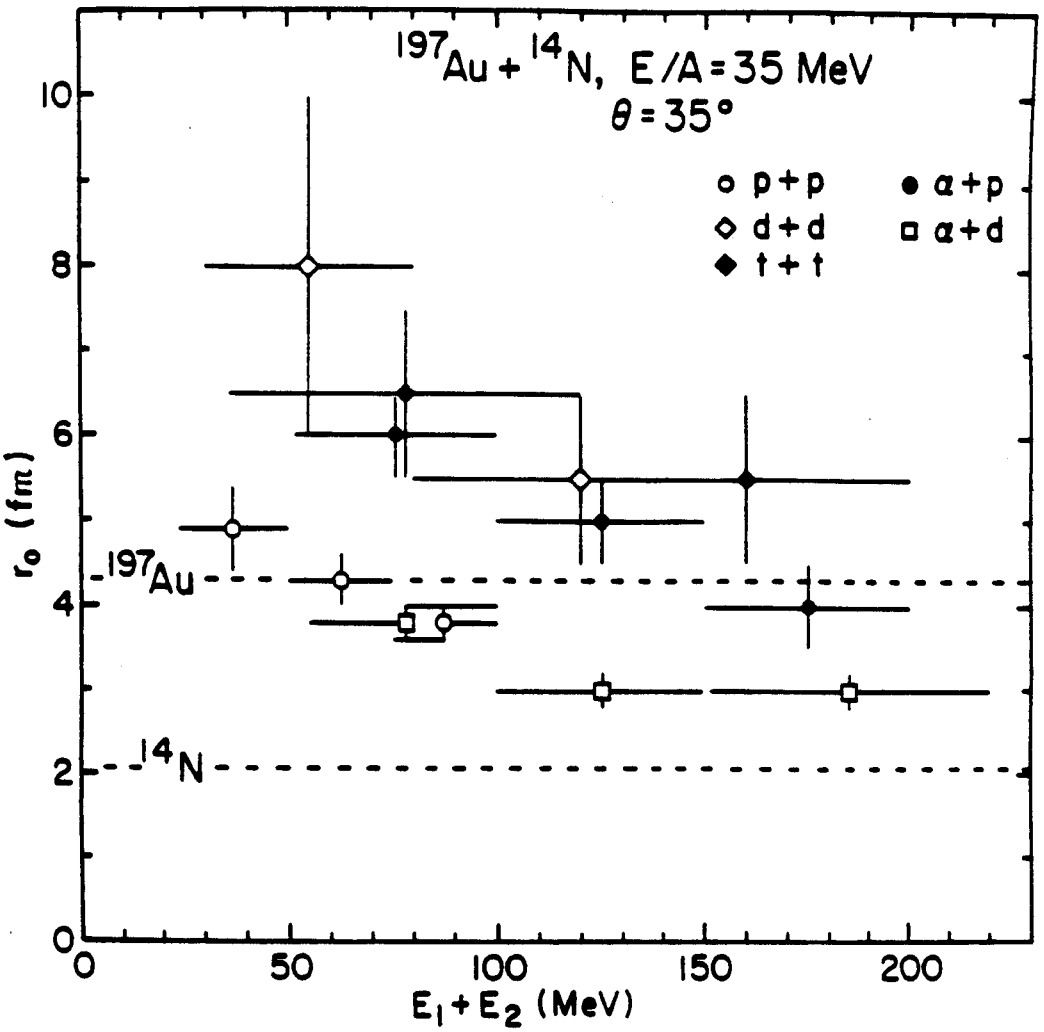

Figure VI.8 Source parameters extracted [Poch 1986a] from inclusive two-particle correlation functions measured at Θ_{av}=35°. The dashed lines indicate the corresponding dimensions of projectile and target; E_1+E_2 denotes the total kinetic energy of the detected particles.

stages of the interaction where the excitation energies are still localized in a small volume and the time interval between subsequent particle emissions is short [Boal 1986].

The smallest source radii are extracted from d-α pairs at high energies. Significantly larger source dimensions are extracted from two-deuteron and two-triton correlations for which the interactions are non-resonant (d-d and t-t pairs, therefore, have larger cross sections), possibly indicating smaller freeze-out densities related to larger interaction cross sections [Chit 1985, Boal 1986]. Similar observations have been made in other experiments. Yet, It is still unclear why the smallest source dimensions are extracted from p-p and d-α correlations and why such large source dimensions are extracted from p-α, d-d, and t-t correlations.

Figure VI.9 compares source radii extracted in terms of the zero-lifetime final state interaction model, Eq. II.12, from p-p (left) and α-d (right) correlation functions measured for ^{14}N, ^{40}Ar, and ^{16}O induced reactions on ^{197}Au at E/A = 35, 60, and 94 MeV, respectively. Smaller source radii are extracted for energetic particles. For the most energetic particles emitted in ^{14}N and ^{16}O induced reactions, the extracted upper limits of the source dimensions are smaller than the size of the target nucleus $\left[r_o(Au) = \sqrt{2/3}\cdot r_{rms}(Au) \approx 4.3 \text{ fm}\right]$. Larger source radii are deduced for ^{40}Ar induced reactions.

Source radii extracted from two-proton correlation functions exhibit an interesting dependence on the quantity, $\frac{E_1 + E_2}{A_1 + A_2} \times \frac{A_p}{E_p}$ (A_1=A_2=1, for protons), the total kinetic energy per nucleon of the two coincident protons measured in units of the kinetic energy per nucleon

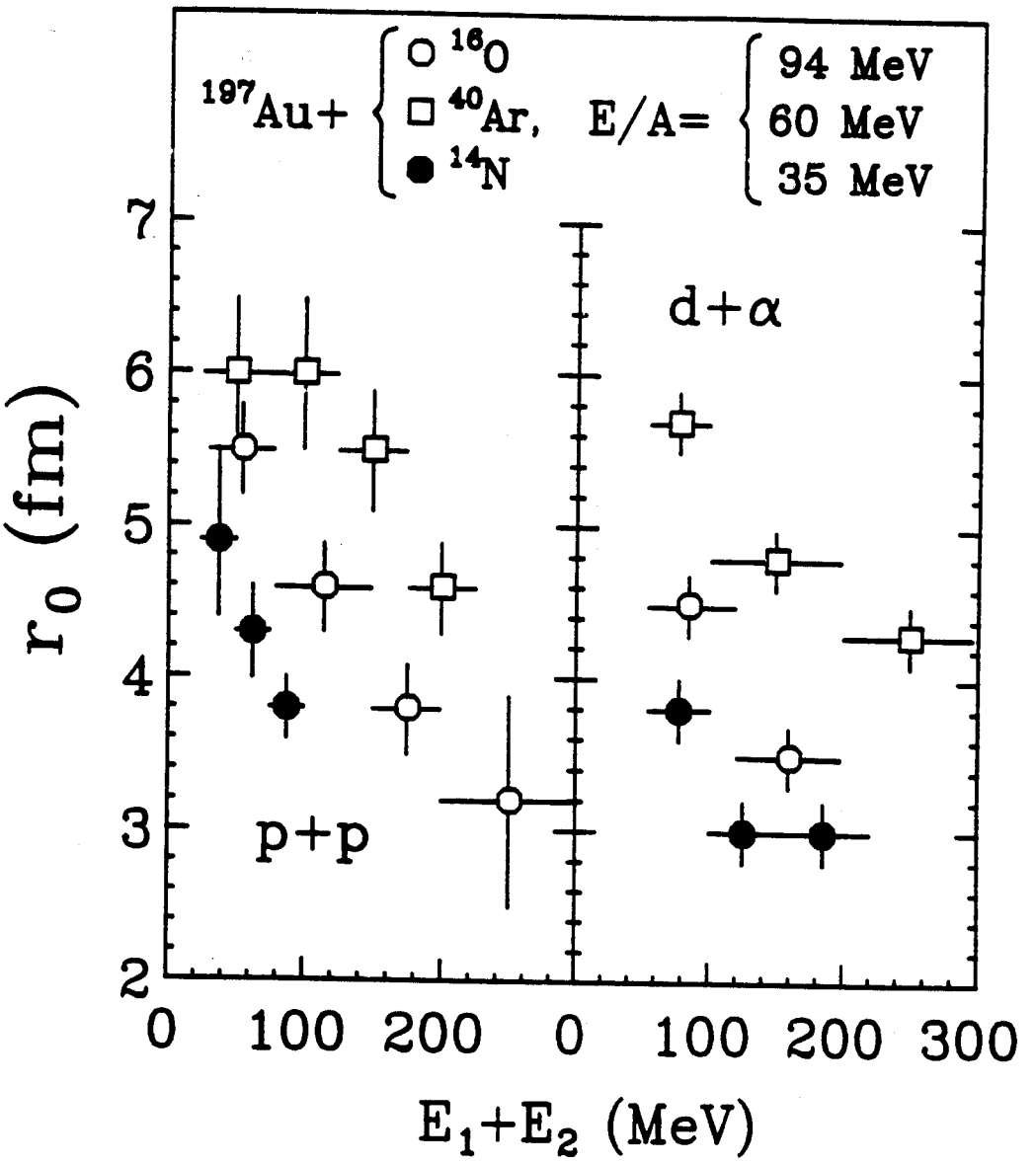

Figure VI.9 Source parameters extracted in terms of Eq. II.12 from p-p correlation functions (left hand side) and α-d correlation functions (right hand side) for the reactions: $^{14}N + ^{197}Au$ at E/A=35 MeV (solid points, [Poch 1986a]), $^{40}Ar+^{197}Au$ at E/A=60 MeV (open squares, [Poch 1987]), and $^{16}O+^{197}Au$ at E/A=94 MeV (open circles). The dependence on the total kinetic energy, E_1+E_2, of the two coincident particles is shown.

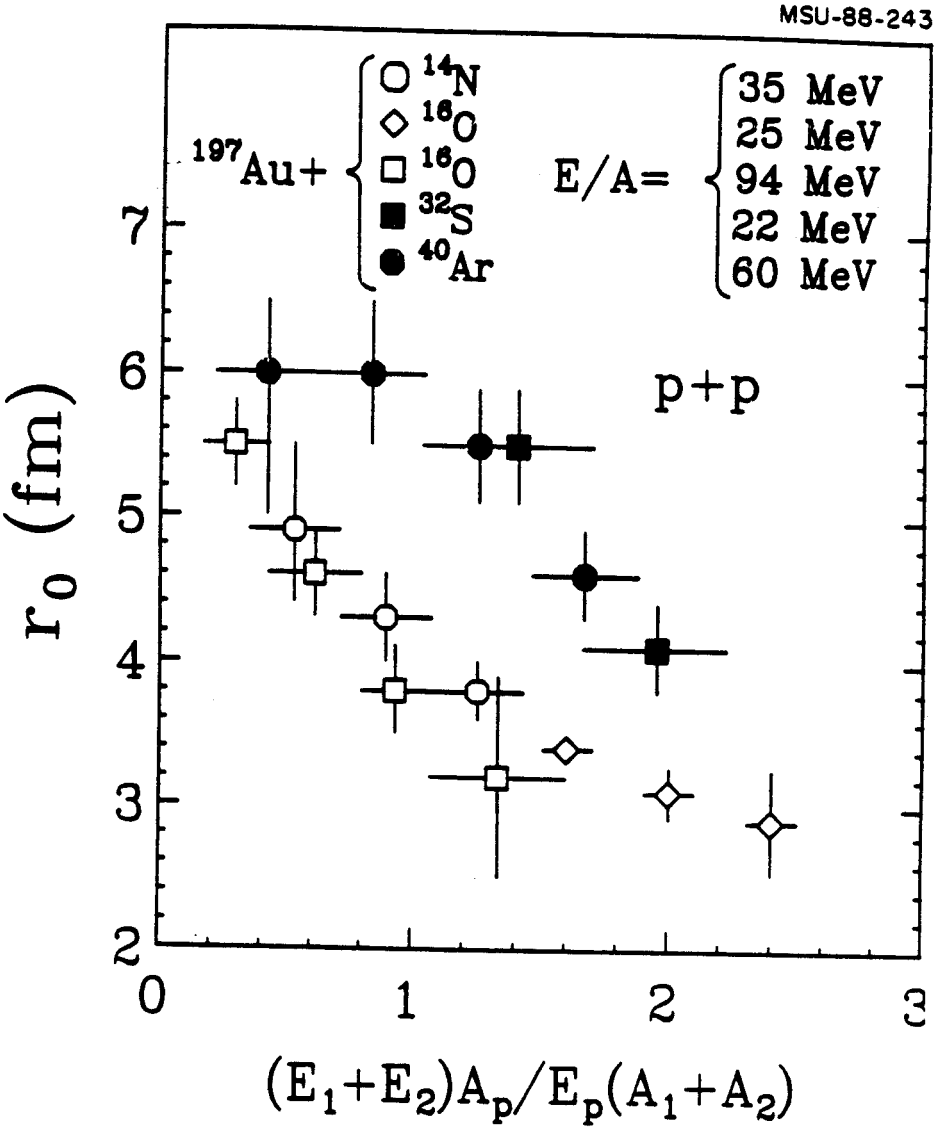

Figure VI.10 Source parameters extracted from p-p correlation functions measured for the reactions: $^{14}N+^{197}Au$ at E/A=35 MeV (open circles, [Poch 1986a]), $^{40}Ar+^{197}Au$ at E/A=60 MeV (solid circles, [Poch 1987a]), $^{16}O+^{197}Au$ at E/A=25 MeV (open diamonds, [Lync 1983]) and at E/A=94 MeV (open squares), and $^{32}S+Ag$ at E/A=22.3 MeV (solid squares, [Awes 1988]). Shown is the dependence on the total kinetic energy per nucleon of the two coincident particles measured in units of the projectile energy per nucleon, $(E_1+E_2)A_p/[(A_1+A_2)E_p]$.

of the incident projectile, see Figure VI.10. Included in this figure are the data of Lynch et al [Lync 1983] and unpublished data of Awes et al. [Awes 1988]. For projectiles of comparable dimensions, such as ^{14}N and ^{16}O, the extracted source radii appear to depend primarily on this parameter. Larger radii are extracted for ^{32}S and ^{40}Ar projectiles which appear to exhibit similar scaling with projectile energy. More data are needed to establish the systematic dependence of two-particle correlation functions on the beam energy and the projectile-target combination.

Several uncertainties, however, remain for the interpretation of inclusively measured two-particle correlation functions: (i) Sequential feeding from highly excited primary fragments may alter the two-particle correlation function. Because of the finite lifetime of possible long-lived intermediate reaction products, sequential decays could lead to a damping of the experimental correlation functions and simulate large source dimensions. Sequential feeding could, however, also increase structures in the correlation functions if the decays proceed via the corresponding resonance. (ii) Collisions with different impact parameters may correspond to sources with different space-time dimensions and/or different relative particle abundances (see Chapter 8). It would, therefore, be desirable to perform more exclusive measurements with appropriate reaction filters to explore the dependence of the correlation functions as impact parameters and/or other reaction varibles. (iii) The calculations of theoretical two-particle correlation functions may have non-negligible uncertainties due to uncertainties of the low energy phase shifts [Poch 1986, Chit 1985]. Phase shifts and densities of states may be different in the nuclear medium as compared

to isolated two-particle systems [Ropk 1982, Ropk 1983, Ropk 1985, Schu 1982, Schu 1983]. Moreover, the effects of the (long-range) Coulomb-interaction with the residual nuclear matter have not yet been treated reliably. They make the extraction of source radii particularly difficult for coincident pairs of particles with different charge-to-mass-ratios. Such distortions have been clearly identified for the p-α [Poch 1985c] and p-d [Poch 1986b] correlations.

CHAPTER 7. EMISSION TEMPERATURES

As discussed in Chapter 5, the single particle kinetic energy spectra can be described in terms of Maxwellian distributions characterized by their mean velocities, v_i, and "kinetic temperature" parameters, τ_i. Such distributions are expected for emissions from thermal sources moving with velocities v_i. Of particular interest is the intermediate rapidity source which dominates the cross sections at large transverse momenta since it is, most likely, associated with the primary reaction zone. The "kinetic temperature" parameters of intermediate rapidity sources formed in nuclear collisions at different incident energies exhibit a smooth and systematic dependence on the incident energy per nucleon. This dependence has been established over a wide range of incident energies. The "kinetic temperature" parameters of the intermediate rapidity source observed in the present experiments are $\tau \approx 17$-20 MeV and $\tau \approx 10$-12 MeV for the reactions $^{16}O + {}^{197}Au$ at E/A=94 MeV and $^{14}N + {}^{197}Au$ at E/A=35 MeV, respectively. Due to possible collective velocity components, the extracted "kinetic temperature" parameters could be higher than the true temperature of the emitting system [Chit 1986, Siem 1979].

Within thermal models, the relative populations of states at different excitation energies are determined by the temperature of the emitting system (see Eqs. II.13-II.16). The yields due to the decays of

particle unbound states are given by Eq. IV.20. Unfortunately, important distortions can arise if the states of interest are fed by the decay of higher lying particle unbound states. These effects have been quantitatively investigated in previous papers [Poch 1987, Xu 1986, Hahn 1987, Fiel 1987, Morr 1986]. In addition, the primary distributions could differ from Eq. IV.20, even if statistical treatments of complex particle emission are justified, because of in-medium modifications [Munc 1982, Schu 1983, Ropk 1983] of the phase space of decay configurations or because of final state interactions between the emitted particles [Boal 1984]. Other complications arise because inclusive measurements average over impact parameter and because of the temporal evolution of the reaction zone as it expands and cools [Bloc 1987].

The use of the Boltzmann factor represents the classical limit for a quantum system. Boltzmann distributions can be used for quantum system if $\exp(\mu/T) << 1$, where μ is the chemical potential. Quantum statistical model calculations [Hahn 1987] indicate that $\exp(\mu/T) \lesssim 0.05$ for the range of particles, break-up densities and emission temperatures of interest; we, therefore, expect the Boltzmann distribution to be a good approximation.

In the following, we regard Eq. IV.20 as an operational definition of the "apparent emission temperature" which clearly defines the relative population of the states under consideration. Possible perturbations due to feeding will be investigated in Chapter 9.

7.1 Yields of particle unbound ^{6}Li states

The left hand side of Figure VII.1 shows the α-d correlation functions with total kinetic energy $E_1+E_2 \geq 50$ MeV for the coincident particles measured in the reaction $^{16}O + ^{197}Au$ at E/A=94 MeV with an average emission angle $\Theta_{av}=45°$. The dashed curve shows a calculation with Eq. II.12, with source radius parameter $r_0=4$ fm, and the solid curve represents the background correlation function as defined in Eq. IV.19. The right hand side of the figure shows the extracted decay coincidence yield, Y_c, resulting from decays, $^6Li \rightarrow \alpha+d$, of particle unstable $^6Li^*$ nuclei, see Eq. IV.19. These yields are plotted as a function of the relative kinetic energy, $T_{c.m.}$, between the coincident deuteron and α particle. (The relative kinetic energy is defined as the kinetic energy in the center-of-mass frame of the two coincident particles; nonrelativistically: $T_{c.m.} = q^2/2\mu$). Calculations based on Eq. IV.20, assuming thermal distributions with T=1, 2.5, 5, and 10 MeV, are shown by the curves on the right hand side of the figure. To calculate the efficiency function, $\varepsilon(E',E)$, the kinetic energy spectra and angular distributions of the excited ^6Li nuclei were parameterized in terms of Eq. V.1 with the parameters tabulated in Table 6, i.e. we assumed that excited ^6Li nuclei are emitted with similar energy and angular distributions as particle stable nuclei (see also Chapter 4.4). The sum in Eq. IV.20 includes the three zero isospin states of ^6Li below 10 MeV excitation energy. The calculations were normalized to reproduce the experimental yield over the energy range of $T_{c.m.}$ = 0.3-1.2 MeV. In order to be less dependent on an accurate description of the line shape of individual states, it is preferable to evaluate the coincidence yields, Y_L and Y_H, integrated over one or several low and high lying states, respectively. By integrating over the energy ranges of $T_{c.m.}$=

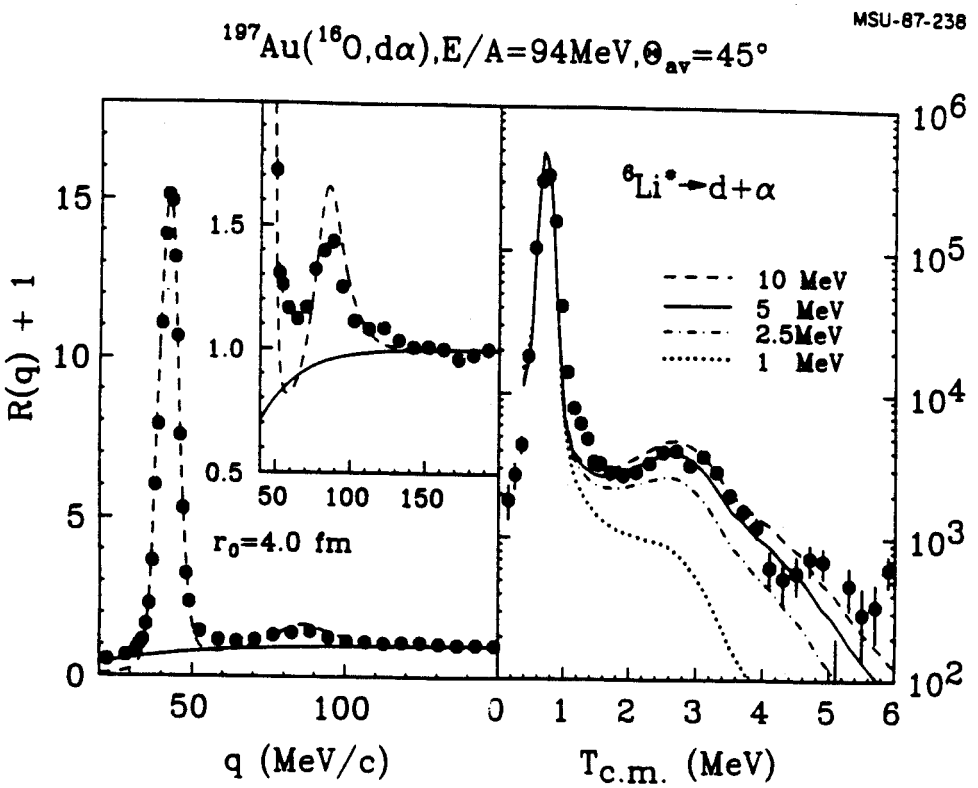

Figure VII.1 The energy integrated α-d correlation function measured in this experiment is shown in the left hand panel. The dashed curve is the calculation of Eq. II.12 with r_0=4 fm, and the solid curve shows the background correlation function, $R_b(q)$, used for the extraction of the coincidence yield for the decay of particle unstable ^{6}Li nuclei, see Eq. IV.19. The dependence of this yield on the relative kinetic energy, $T_{c.m.}$, of the coincident particles is shown in the right hand panel. The curves show yields predicted for thermal distributions corresponding to various temperatures, see Eq. IV.20.

0.3-1.45 and 1.5-6.25 MeV and comparing the experimental yield ratio, Y_H/Y_L, to that calculated from Eq. IV.20, one extracts an apparent emission temperature of $T(^6Li) = 5.8^{+2.0}_{-1.3}$ MeV. Here, the error was estimated from the uncertainty in the normalization of the correlation function; statistical errors were negligible. The spectral shapes in Figure VII.1 are sensitive to temperatures smaller than the level separation, $\Delta E \approx 3$ MeV; higher emission temperatures are more difficult to distinguish. Additional uncertainties result from the unknown magnitude of feeding from higher lying states [Hahn 1987, Fiel 1987].

Figure VII.2 shows the decay coincidence yields, Y_c, from the decay $^6Li^* \rightarrow \alpha+d$, measured for the reaction $^{14}N + ^{197}Au$ at E/A=35 MeV and at $\Theta_{av}=35°$ and 50°. Errors shown are only statistical. We have used the same background correlation function as in Figure VII.1 to extract the α-d coincidence yields resulting from the decay of particle unstable ^6Li nuclei. The curves in Figure VII.2 show the coincidence yields predicted in terms of Eq. IV.20 assuming thermal distributions with T=1, 2.5, 5, and 10 MeV. For the calculation of efficiency function, $\varepsilon(E',E)$, the laboratory energy spectra and angular distributions of the ^6Li parent nuclei were described in terms of Eq. V.1 with the parameters given in Table 5; these distributions are shown by the solid lines in Figure V.2. The curves are normalized to reproduce the experimental yield integrated over the energy range of $T_{c.m.}$ = 0.3 - 1.2 MeV. By integrating the decay yields over the energy ranges of $T_{c.m.}$ = 0.25-1.45 and 1.5-6.25 MeV and comparing the ratio of these yields to the corresponding ratio calculated from Eq. IV.20, an average emission temperature of T≈4 MeV is extracted [Chit 1986b]. This value is believed to be accurate to within about 25% due to uncertainties in the α-d background correlation

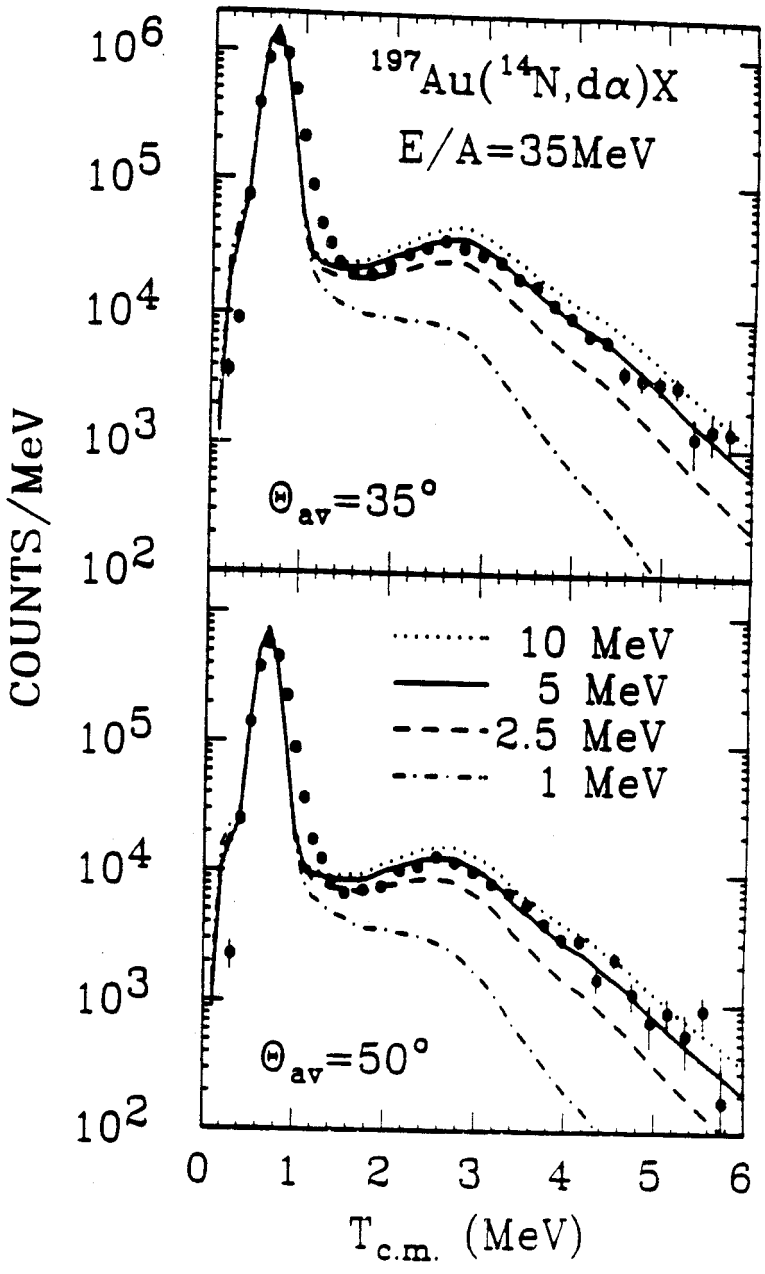

Figure VII.2 Energy spectrum resulting from the decay of particle-unstable states in ^{6}Li. The curves correspond to thermal distributions with T = 1, 2.5, 5, and 10 MeV (see Eq. IV.20), taking the response of the hodoscope into account.

function and due to the saturation of the coincidence yields at higher temperatures; statistical uncertainties are negligible [Chit 1986b].

To test the assumptions of our Monte Carlo calculations for the efficiency function, we examined the decay of $^{6}Li^{*}_{2.186} \rightarrow \alpha+d$ measured in the reaction $^{14}N + ^{197}Au$ at E/A=35 MeV. Figure VII.3 shows the total kinetic energy distribution, $dY_c/d(E_\alpha+E_d)$, integrated over the first peak in the ^{6}Li excitation energy spectrum, $T_{c.m.}$=0.3-1.2 MeV. The yields predicted by the Monte Carlo calculations are shown by the solid histograms. The data are consistent with our assumptions about the parent energy distribution.

Angular distributions, $dY_c/d\Theta_R$ and $dY_c/d\Phi_R$, of the decay yields from the 2.186 MeV state in ^{6}Li are shown in Figure VII.4. Here, Θ_R and Φ_R are defined by Eqs. IV.17 and IV.18. The histograms show the result of our Monte-Carlo calculations. (The asymmetry of $dY_c/d\Phi_R$ with respect to Φ_R=90° is caused by the binning during the analysis of the experimental and simulated data.) It was verified that details of the Θ_R- distribution are sensitive to uncertainties in the absolute energy calibration. Within these uncertainties, the data are consistent with the assumption of isotropic decay.

7.2 DECAY OF WIDELY SEPARATED STATES

More accurate determinations of apparent emission temperatures, however, can be made [Poch 1987, Poch 1985] by measuring the relative populations of states separated by significantly larger energy intervals, $\Delta E >> T$. Examples of widely separated states which were accessible in our experiments are: $^{4}He_{g.s.}$ and $^{4}He_{20.1} \rightarrow p+t$, $^{5}Li_{g.s.} \rightarrow \alpha+p$ and $^{5}Li_{16.7} \rightarrow {}^{3}He+d$, $^{8}Be_{3.04} \rightarrow \alpha+\alpha$ and $^{8}Be_{17.6} \rightarrow {}^{7}Li+p$. These states

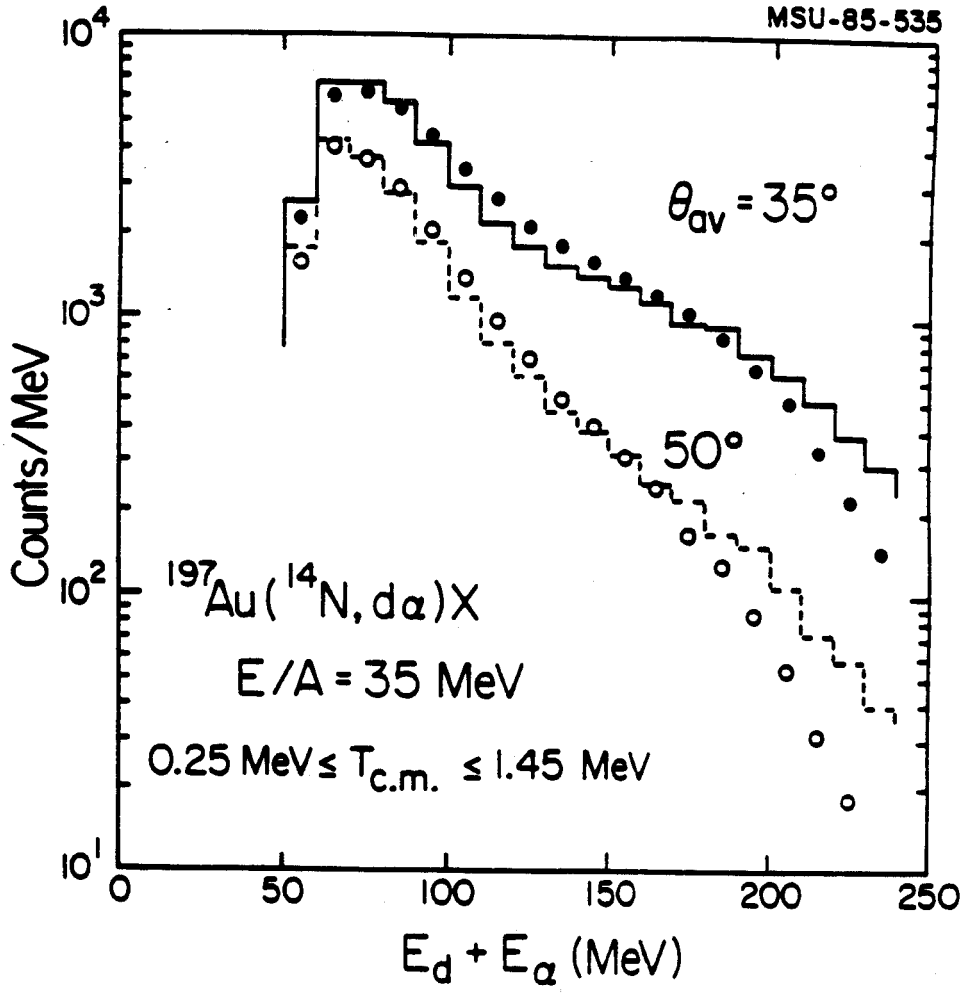

Figure VII.3 Measured α-d coincidence yield resulting from the decay $^6Li^*_{2.186} \rightarrow \alpha+d$ as a function of the total kinetic energy, $E_\alpha + E_d$. The histogram is the result of the Monte Carlo calculations described in the text.

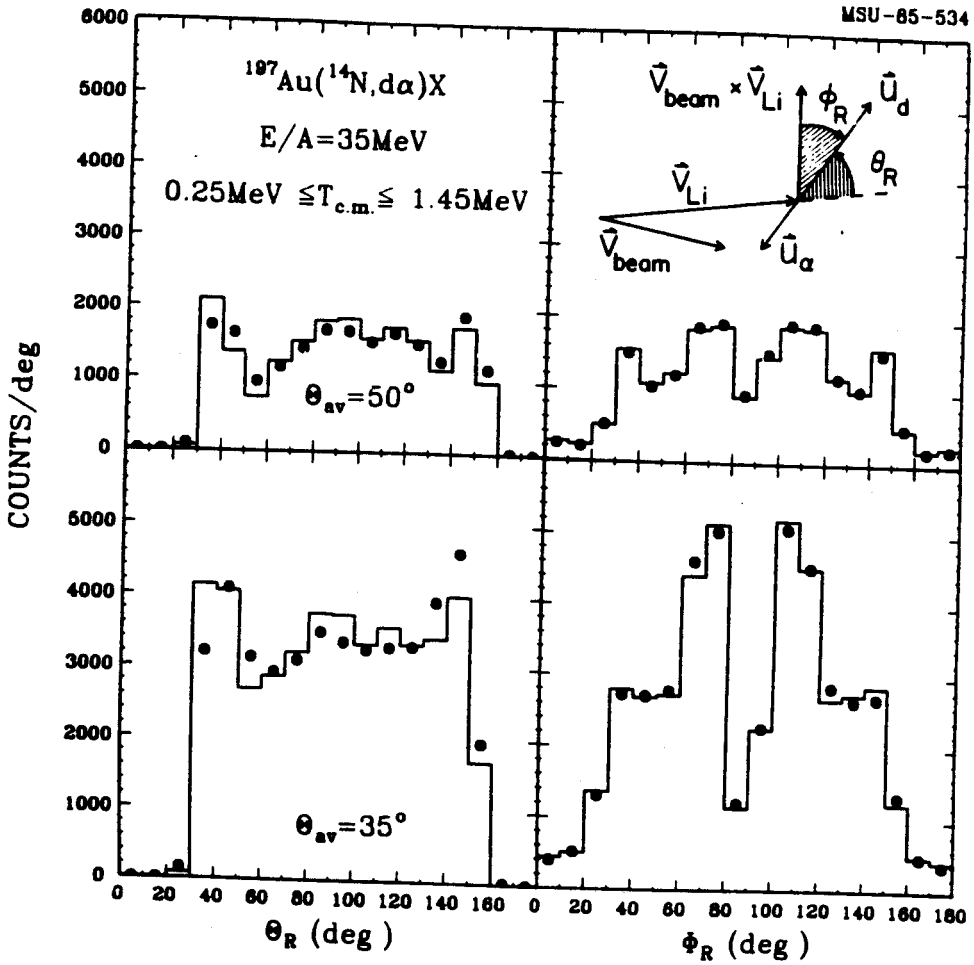

Figure VII.4 Angular distributions of the decay-yields from the decay $^6Li^*_{2.186} \rightarrow \alpha+d$. The angles Θ_R and Φ_R are defined in Eqs. IV.17-IV.18 and depicted in the insert. The histograms are the results of Monte Carlo calculations in which the ^{6}Li nuclei are assumed to decay isotropically in their respective rest frames.

are clearly visible in the correlation functions shown in Figure VI.4-VI.6. Upper and lower limits for background correlation functions, assumed in our analysis, are also indicated in these figures by dashed lines. (For a more detailed discussion of the p-^{7}Li and the α-α correlation functions, see [Poch 1987])

The solid curves in Figure VII.5 show the temperature dependence of the yield ratios, Y_H/Y_L, predicted by Eq. IV.20 for these widely separated states in ^{4}He, ^{5}Li, and ^{8}Be. For the efficiency calculations, the parent distributions of particle unstable ^{4}He nuclei were assumed to be identical to those measured for particle stable α-particles; they were parametrized in terms of Eq. V.1 using the parameters given in Table 6. For particle unstable ^{5}Li nuclei, two calculations were performed by parametrizing the parent distributions in terms of Eq. V.1 and adopting the parameters for particle stable α-particles and ^{6}Li nuclei, respectively. For particle unstable ^{8}Be nuclei, we used the parameters extracted from the distributions of particle stable ^{6}Li and ^{7}Li nuclei. It was verified that the results were insensitive to the specific choices of parameters as long as the calculated parent distributions reproduce the overall trends of the inclusive cross sections. The shaded bands in Figure VII.5 indicate yield ratios and emission temperatures which are consistent with the extreme assumptions about the background correlation functions shown by the dashed lines in Figures VI.4-VI.6. Apparent emission temperatures of $T_{^4He}$= 4.2-5.4 MeV, $T_{^5Li}$= 4.6-5.6 MeV, and $T_{^8Be}$= 4.0-4.6 MeV are extracted. These values are consistent with that extracted from the populations of particle unbound states in ^{6}Li. Table 9 gives the relative momentum intervals over which the yields of the individual states were integrated.

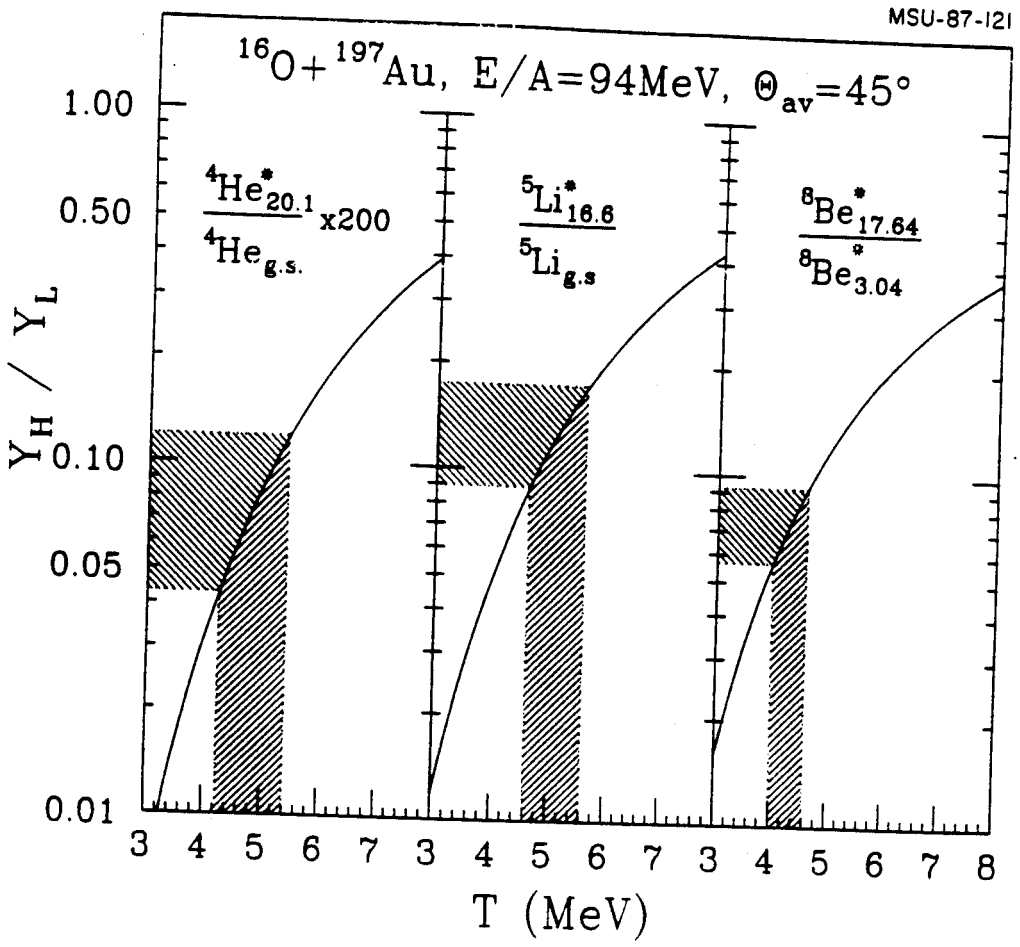

Figure VII.5 The solid curves show the temperature dependence of the yield ratios, Y_H/Y_L, for widely separated states in ^{4}He, ^{5}Li, and ^{8}Be as predicted by Eq. IV.20. The respective states are indicated in the figure. The shaded bands indicate values consistent with our measurements assuming that the background correlation functions lie within the bounds indicated by the dashed lines in Figure VI.4-VI.6.

TABLE 9

Integration ranges in decay channels

for unbound states

	q_{low} (MeV/c)	q_{high} (MeV/c)
p-t	10	30
p-α	25	100
d-^{3}He	20	50
p-^{7}Li	14	30
α-α	65	125

Since more energetic particles are expected to be emitted at the early stages of the reaction at which the excitation energy per nucleon should be highest, one could expect to measure higher emission temperatures for parent nuclei of higher kinetic energy. In order to evaluate such an energy dependence we have set gates on the total kinetic energies, E_1+E_2, of the emitted particles. As will be discussed in Chap. 9, the relative populations of states in ^{5}Li nuclei are predicted to suffer the least distortions from sequential decays, therefore, we have only investigated the energy dependence for this most favorable case. For total kinetic energies of E_1+E_2= 55-125 and 125-300 MeV, apparent emission temperatures of $T_{^5Li}$= 4.4-5.6 and 5.0-6.0 are extracted, respectively (see Figure VII.6). Thus the dependence of the emission temperature on the kinetic energy of the emitted particles is slight.

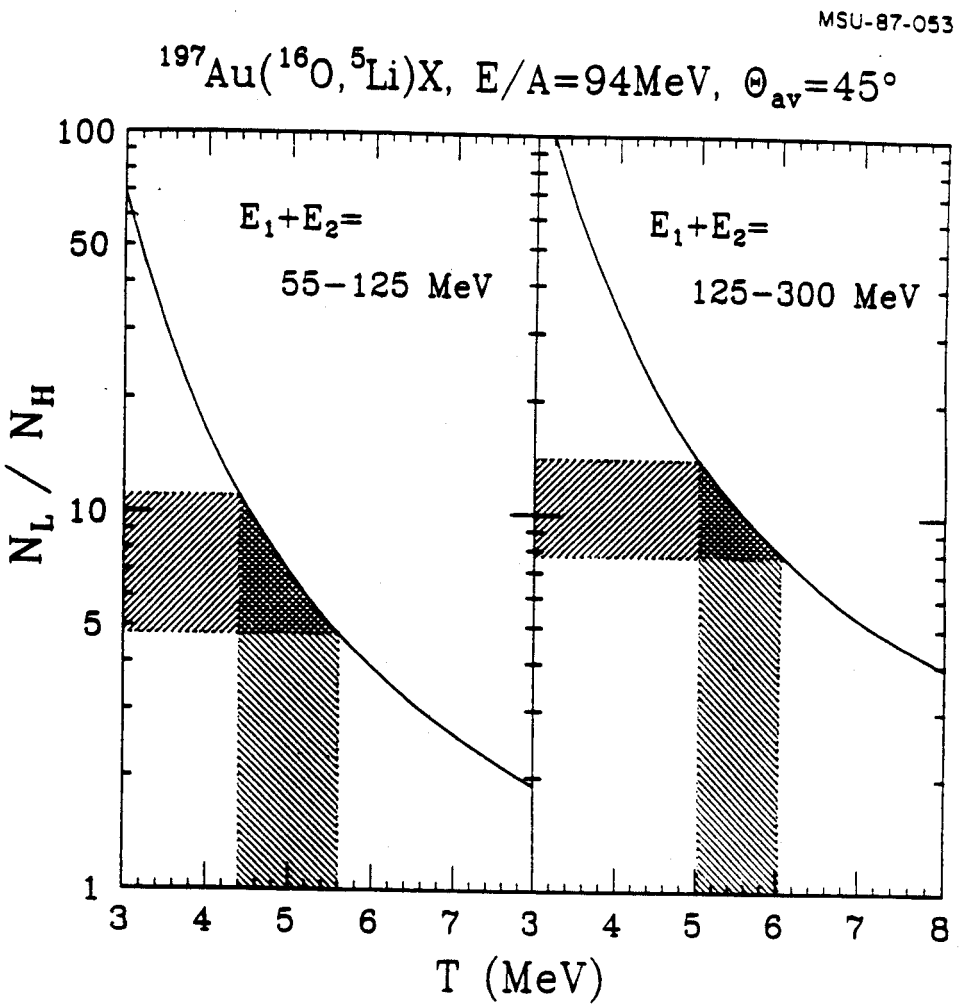

Figure VII.6 The solid curves show the temperature dependence of the yield ratios, Y_H/Y_L, for widely separated states in ^{5}Li as predicted by Eq. IV.20. The two panels are gated by different ranges of total kinetic energy, E_1+E_2, for the coincident particles as indicated in the figure. The shaded bands indicate values consistent with our assumptions on the background correlation functions, see Figure VI.5.

7.3 DISCUSSION

Figure VII.7 gives a comparison of the apparent emission temperatures measured in the present two experiments, as well as the reaction $^{40}Ar+^{197}Au$ at E/A=60 MeV [Poch 1987]. For all cases, the emission temperatures extracted from the relative population of states are considerably smaller than the kinetic temperature parameters which characterize the slopes of the kinetic energy spectra. The extracted emission temperatures are consistent with a slight increase of about 20% over the energy range considered; this increase is of comparable magnitude as the systematic uncertainty and, therefore, not established beyond doubt. The insensitivity of the relative populations of states to the incident energy stands in marked contrast to the systematic energy dependence of the kinetic temperature parameters. As was shown in Figure V.5, the kinetic temperatures increase by nearly a factor of two as the incident energy is increased from E/A≈35 to 94 MeV.

It is rather surprising that the relative populations of states indicate rather similar emission temperatures over the range of incident energies of E/A≈35-94 MeV. If one applies grand canonical treatments [Goss 1978] of the fragmentation process to these reactions, the insensitivity of the emission temperature to the incident energy requires, that fragment freeze-out occurred at nearly constant temperature, T≈5 MeV, rather than at constant density as is most frequently assumed. Our observations could, instead, also indicate that complete thermal and chemical equilibrium is not achieved during the final stages of the reaction.

The large discrepancy between the relatively small emission temperatures which characterize the populations of particle unbound

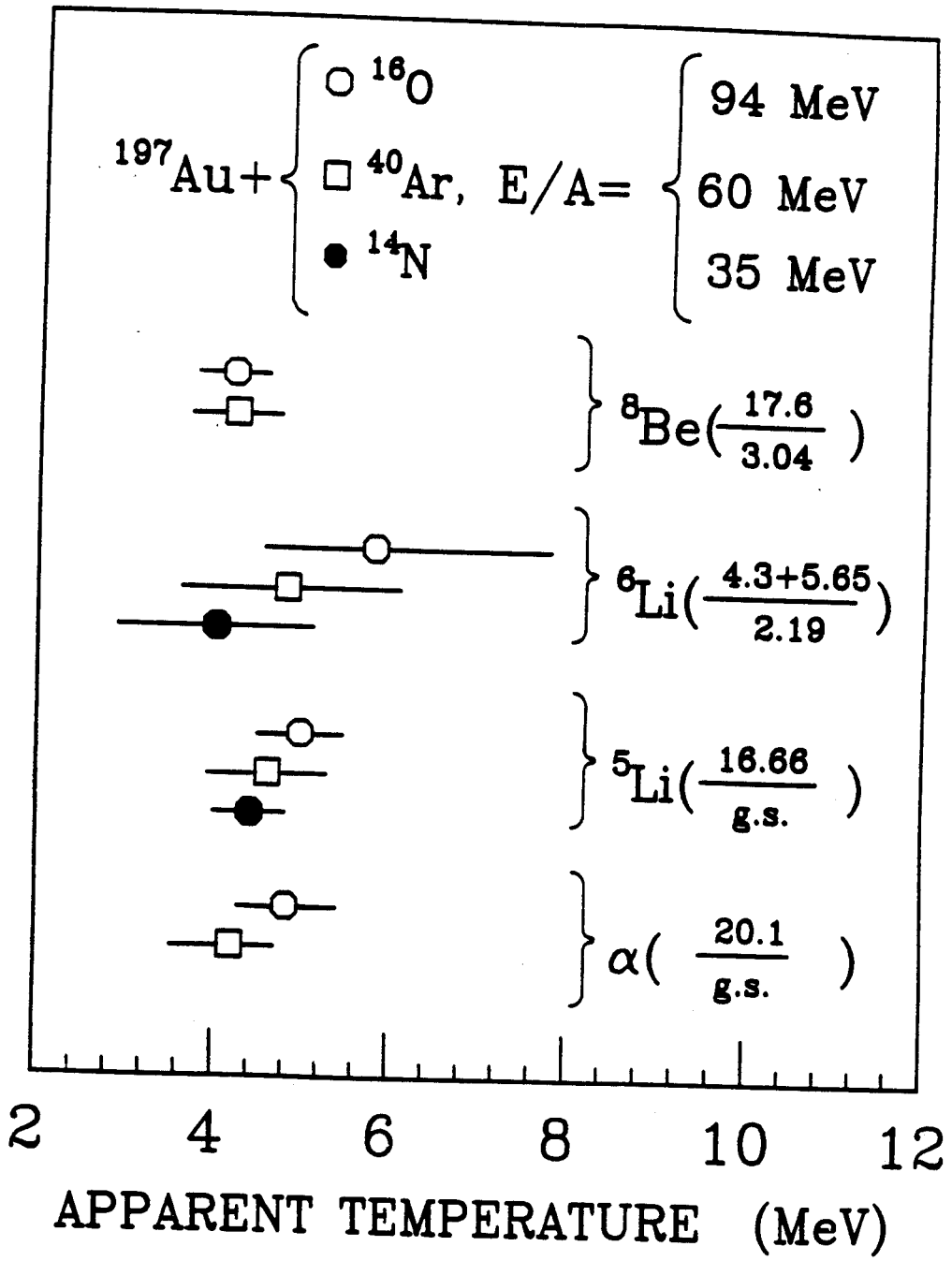

Figure VII.7 Apparent emission temperatures extracted from the relative populations of states in ^{4}He, ^{5}Li ^{6}Li and ^{8}Be nuclei emitted in the reactions: ^{14}N+^{197}Au at E/A=35 MeV ([Chit 1986b], solid points), ^{40}Ar+^{197}Au at E/A=60 MeV ([Poch 1987], open squares), and ^{16}O+^{197}Au (open circles).

states and the relatively large kinetic temperature parameters which characterize the slopes of the kinetic energy spectra is not understood quantitatively. In principle, large kinetic temperature parameters extracted from the slopes of the kinetic energy spectra could arise from the superposition of a large collective velocity component onto smaller thermal velocity components [Chit 1986, Siem 1979]. Qualitatively, the superposition of collective and random (thermal) velocity components has been inferred from a number of experiments [Tsan 1986, Chit 1986, Tsan 1984]. It is, however, difficult to establish their relative magnitudes and infer the extent to which temperatures extracted from kinetic energy spectra are modified by collective velocity components.

While collective velocity components can strongly affect single particle inclusive energy distributions, they should be less visible in the distributions of relative kinetic energy spectra between two coincident particles, provided that the two coincident particles are emitted from the same source. For the extreme case of purely collective motion, all particles have the same velocity; the relative velocity of two coincident particles is zero. One might, therefore, expect that a superposition of small thermal and large collective velocity components could be detected in the distributions of relative kinetic energies, $T_{c.m.}$, between coincident particles detected at small relative angles. Figures VII.8 and VII.9 show the experimental d-d and α-d coincidence yields as a function of the relative kinetic energy. (For the case of α-d coincidences, the contributions from the decay of particle unstable states in ^{6}Li contribute only for $T_{c.m.} \leq 5$ MeV). The curves correspond to yields predicted in terms of Maxwellian distributions folded by the detection efficiency of the experimental apparatus. Clearly temperatures

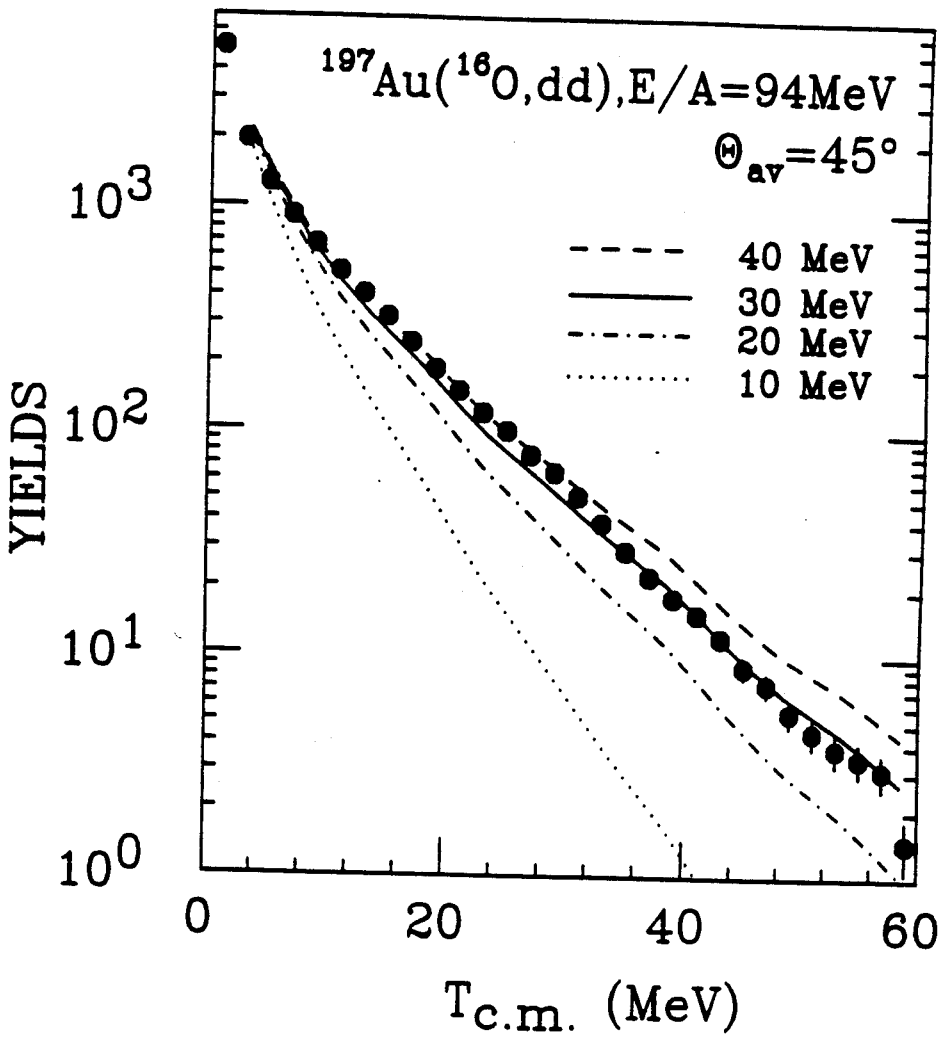

Figure VII.8 Experimental d-d coincidence yield as a function of the relative kinetic energy, $T_{c.m.}$, of the two coincident deuterons. The curves show yields expected for Maxwellian distributions of different temperatures folded by the detection efficiency of the experimental apparatus.

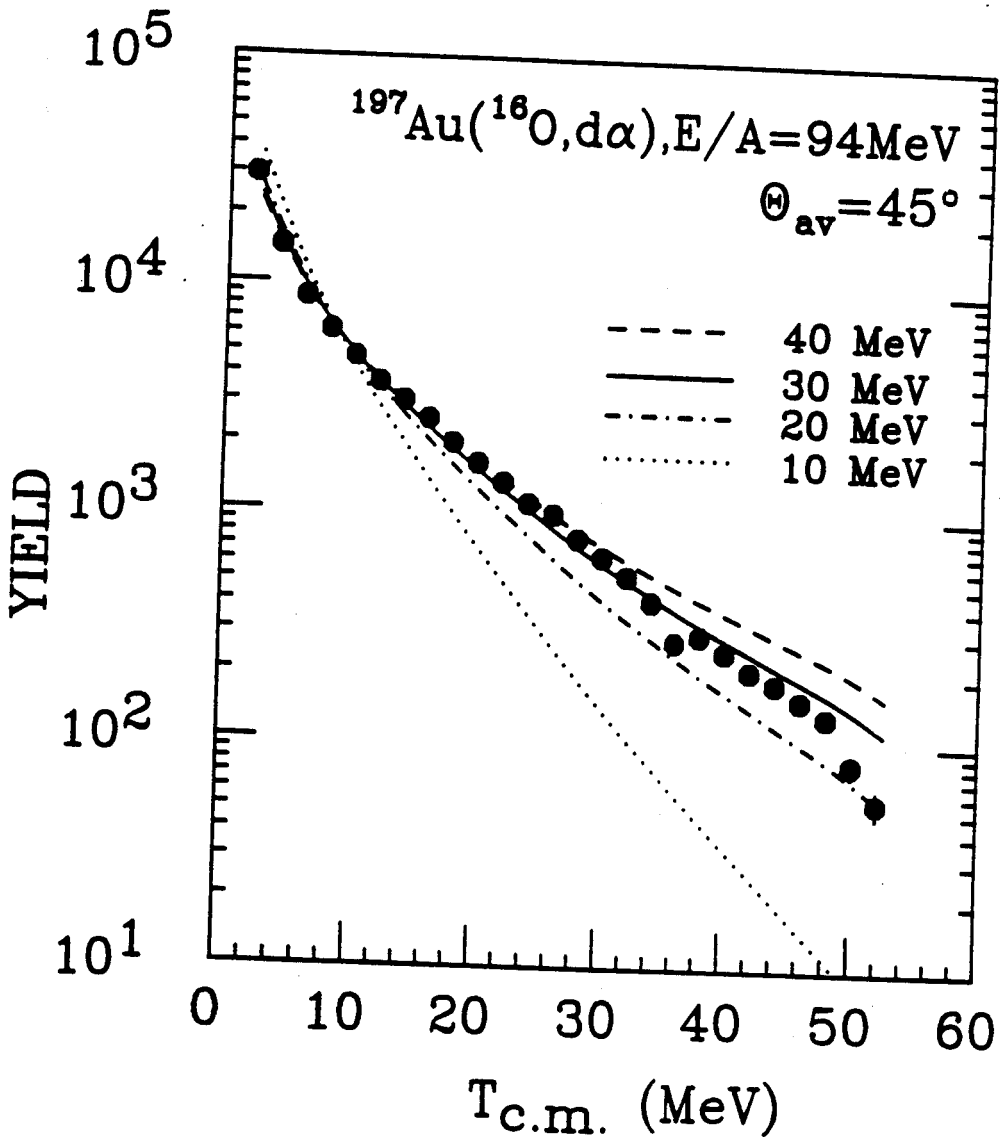

Figure VII.9 Experimental α-d coincidence yield as a function of the relative kinetic energy, $T_{c.m.}$, of the two coincident particles. The curves show yields expected for Maxwellian distributions of different temperatures folded by the detection efficiency of the experimental apparatus.

below 10 MeV are excluded by the data which are most consistent with values of the order of 30 MeV. Since final state Coulomb interactions and momentum conservation effects can modify the detailed shape of the relative kinetic energy spectra, we feel that temperatures of 20 or 40 MeV cannot be ruled out with absolute certainty.

To provide additional evidence for the numerical accuracy of the Monte Carlo calculations shown in Figures VII.8 and VII.9, we show in Figure VII.10 the measured d-d coincidence yields as a function of the kinetic energy, $E_1+E_2-T_{c.m.}$, of the d-d center-of-mass motion. The histogram represents the result of Monte Carlo calculations in which these energy distributions were parametrized in terms of Eq. V.1 using the parameters extracted from the inclusive alpha-particle spectra. A Maxwellian distribution characterized by T=30 MeV was adopted for the spectrum of relative kinetic energies. The calculations are in good agreement with the data.

It is clear that the relative kinetic energy spectra between coincident light particles and the relative populations of particle unbound states cannot be described in terms of similar temperatures. Qualitatively, this conclusion could have been arrived at by inspecting the two-particle correlation functions which approach a constant value at larger relative momenta.

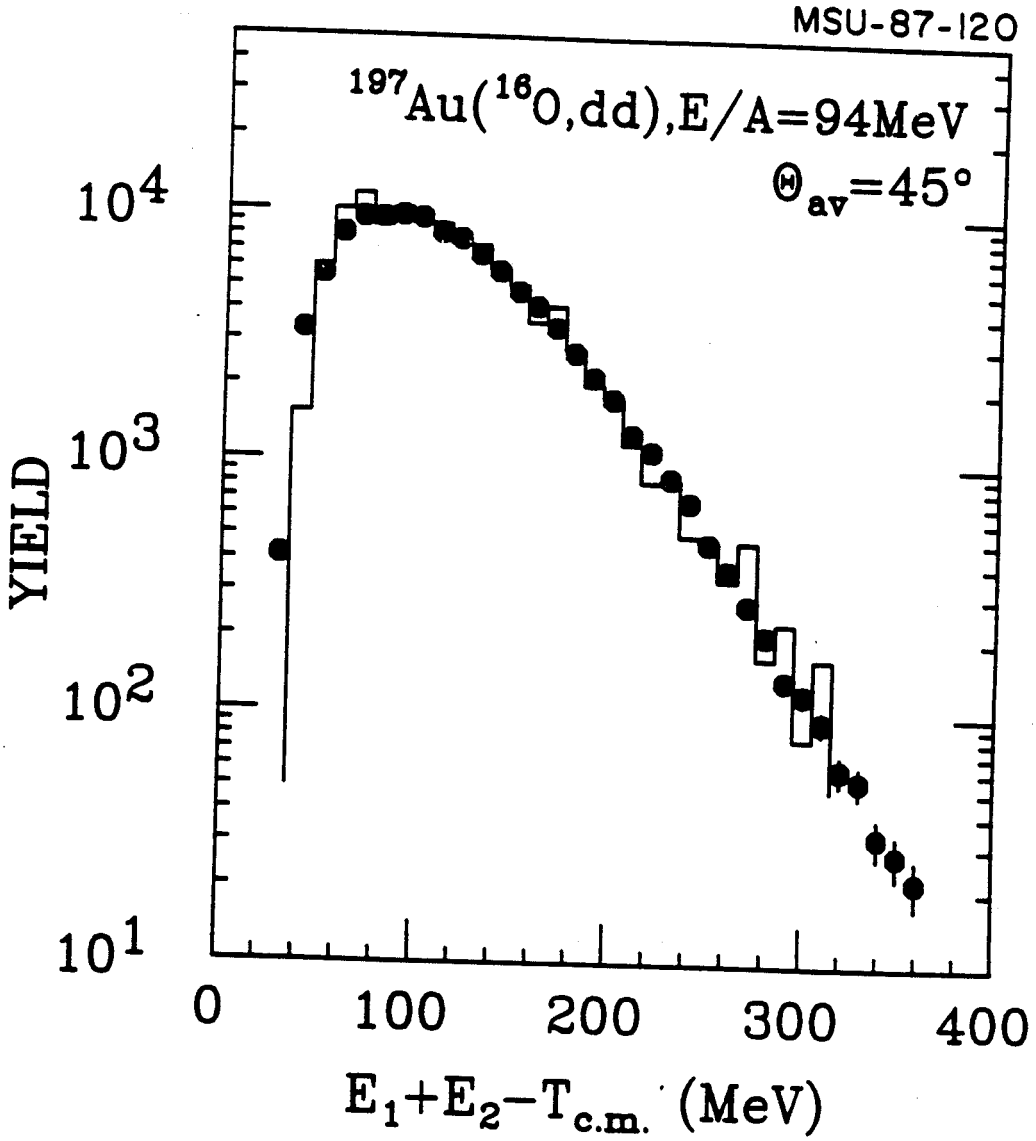

Figure VII.10 Experimental d-d coincidence yield as a function of the kinetic energy of the d-d center-of-mass system, $E_1+E_2-T_{c.m.}$. The histogram show the result of Monte-Carlo calculations in which it is assumed that these energies are distributed according to Eq. V.1 with the parameters extracted from the inclusive alpha particle spectra (see Table 6).

CHAPTER 8. MEASUREMENTS IN FILTERED REACTIONS

While two-particle inclusive measurements can provide insights into the average properties of the collision process, more detailed information can be achieved from more exclusive measurements in which specific classes of reactions can be enhanced or suppressed. We used the linear momentum transferred to the heavy reaction residue as a filter to discriminate between quasi-elastic and more violent, fusion-like projectile-target interactions. The correlation functions at small relative momenta and relative populations of states were investigated for the different gates placed on the linear momentum transfer.

The basic concept of the technique is illustrated in Figure VIII.1. For large linear momentum transfers in the reaction, the target residue is accelerated in the beam direction and the subsequent fission fragments are focussed kinematically, resulting in small folding angles, Θ_{ff}, defined as the sum of the polar angles for the two fission fragments in the laboratory. On the other hand, the residue will stay nearly at rest in the laboratory for small linear momentum transfers, the fission fragments will be emitted in almost opposite directions, and the folding angles are close to 180°. This technique had been applied in previous coincident experiments [Back 1980, Awes 1981]. Quantitatively, the observed folding angle distribution can be related

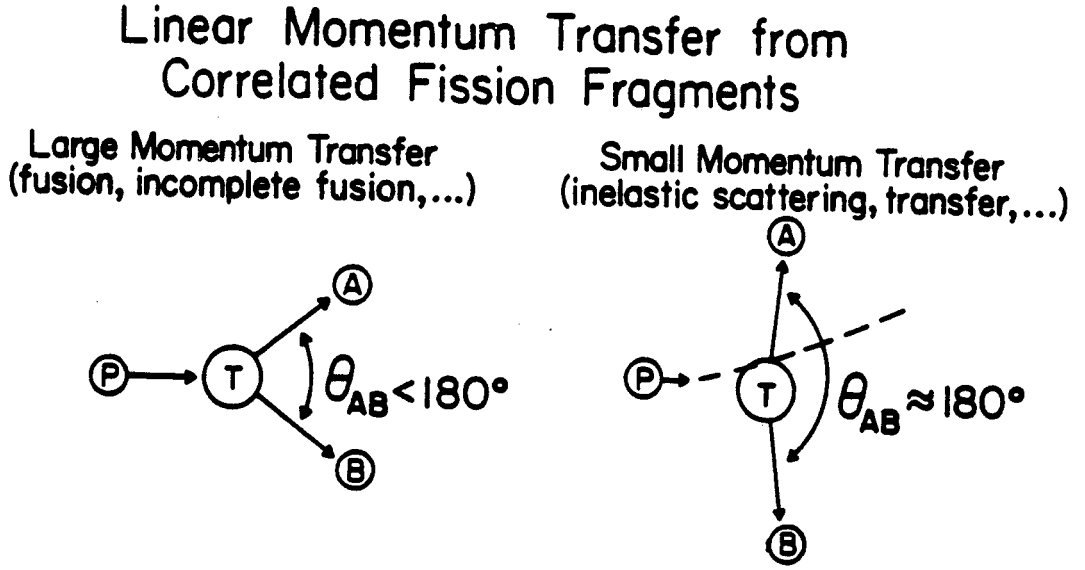

Figure VIII.1 Schematic illustration of the reaction filter. A and B represent the subsequent fission fragments. Θ_{AB} is the folding angle defined in the text.

to the distribution of linear momentum transfer with the help of Monte Carlo calculations.

8.1 FOLDING ANGLE DISTRIBUTIONS

Folding angle distributions between two fission fragments measured in coincidence with protons, deuterons, tritons, α-particles and Li nuclei, detected at $\Theta_{av}=20°$, are shown in Figure VIII.2. For orientation, the upper scale gives an approximate scale for the fraction, $\Delta p/p$, of the projectile momentum which is transferred to the heavy reaction residue. This scale gives the relation between the linear momentum of the fissioning system and the most probable folding angle between two fission fragments resulting from the symmetric fission of the composite nucleus. With increasing mass of the detected light particle, the maximum of the coincident folding angle distribution is shifted towards larger angles. To a large extent, this effect is due to momentum conservation: Heavier particles emitted at forward angles carry away a larger fraction of the projectile momentum.

Even for the ideal case of fission of a composite nucleus with unique spin, excitation energy, and recoil momentum, rather broad folding angle distributions will be measured because of the finite widths of the mass and kinetic energy distributions of the fission fragments and because of additional broadening by light particle evaporation. For this reason, gates on folding angle distributions do not select a sharply defined range of recoil momenta. Instead, they correspond to a filter of moderate resolution which, nevertheless, can serve to enhance or suppress reactions associated with small or large linear momentum transfers.

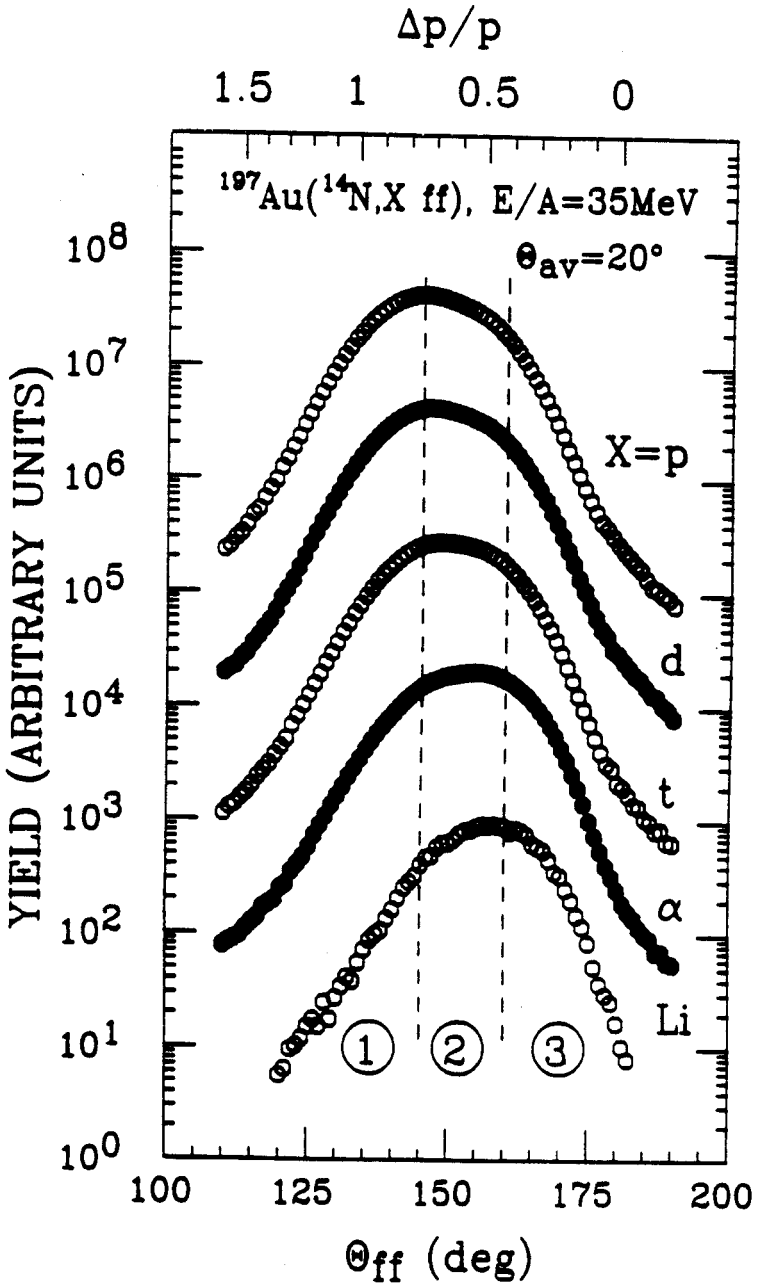

Figure VIII.2 Folding angle distributions between two coincident fission fragments detected in coincidence with p, d, t, α, and Li nuclei emitted at θ_{av}= 20°. The dashed lines depict the boundaries of the folding angle gates (1), (2), and (3).

In order to discriminate between reactions associated with small or large linear momentum transfers to the heavy reaction residue, we define three different gates on folding angle. The boundaries of these gates are indicated by the dashed vertical lines in Figure VIII.2. More specifically, these gates are defined by: $\Theta_{ff}<145°$ (gate 1), $145°\leq\Theta_{ff}\leq160°$ (gate 2), and $\Theta_{ff}>160°$ (gate 3). Because of the low fissility of nuclei with $Z\approx80$, target residues with excitation energies of less than a few tens of MeV will not fission; the study of such gentle collisions necessitates the use of more fissile, heavier target nuclei such as uranium [Back 1980, Awes 1981]. Nevertheless, we will use the term "peripheral, quasi-elastic collisions" for reactions filtered by large folding angles ($\Theta_{ff}>160°$, gate 3). It should then be clear, that this operational definition excludes the most gentle of these collisions.

8.2 FILTERED SINGLE-PARTICLE DISTRIBUTIONS

The effects of filtering light particle energy spectra by the three folding angle gates are illustrated in Figures VIII.3-VIII.5. The spectra were obtained by summing the corresponding yields over all detectors of the hodoscope with the center of the hodoscope placed at $\Theta_{av}=20°$. The absolute normalizations of the vertical scale is in arbitrary units; relative normalization are proportional to the ratio N^c_{ff}/N_{ff}, where N^c_{ff} corresponds to the number of triple coincidences (light particle + two fission fragments) and N_{ff} corresponds to the number of two-fold coincidences (two fission fragments) for a given constraint on folding angle. Figures VIII.3 and VIII.4 show the spectra of hydrogen and helium isotopes, respectively. The right hand part of

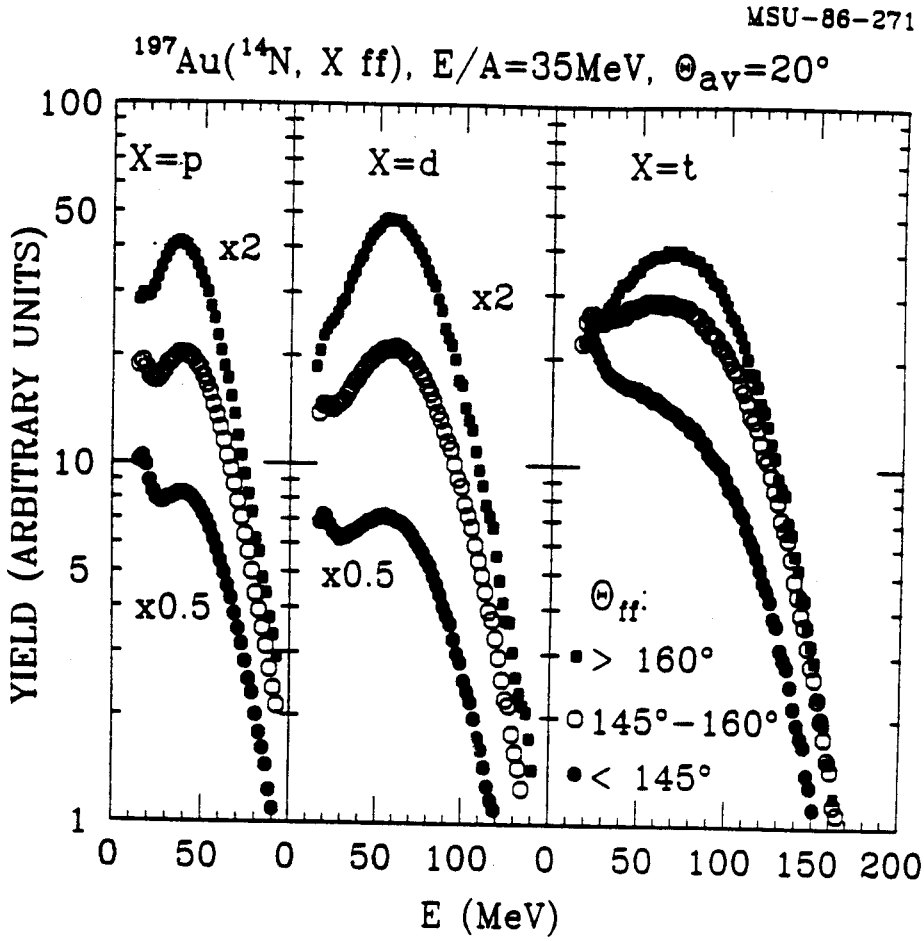

Figure VIII.3 Yields of protons, deuterons and tritons summed over all elements of the hodoscope with the center of the hodoscope positioned at θ_{av}=20°. The distributions are shown for the three gates on folding angle defined in Figure VIII.2.

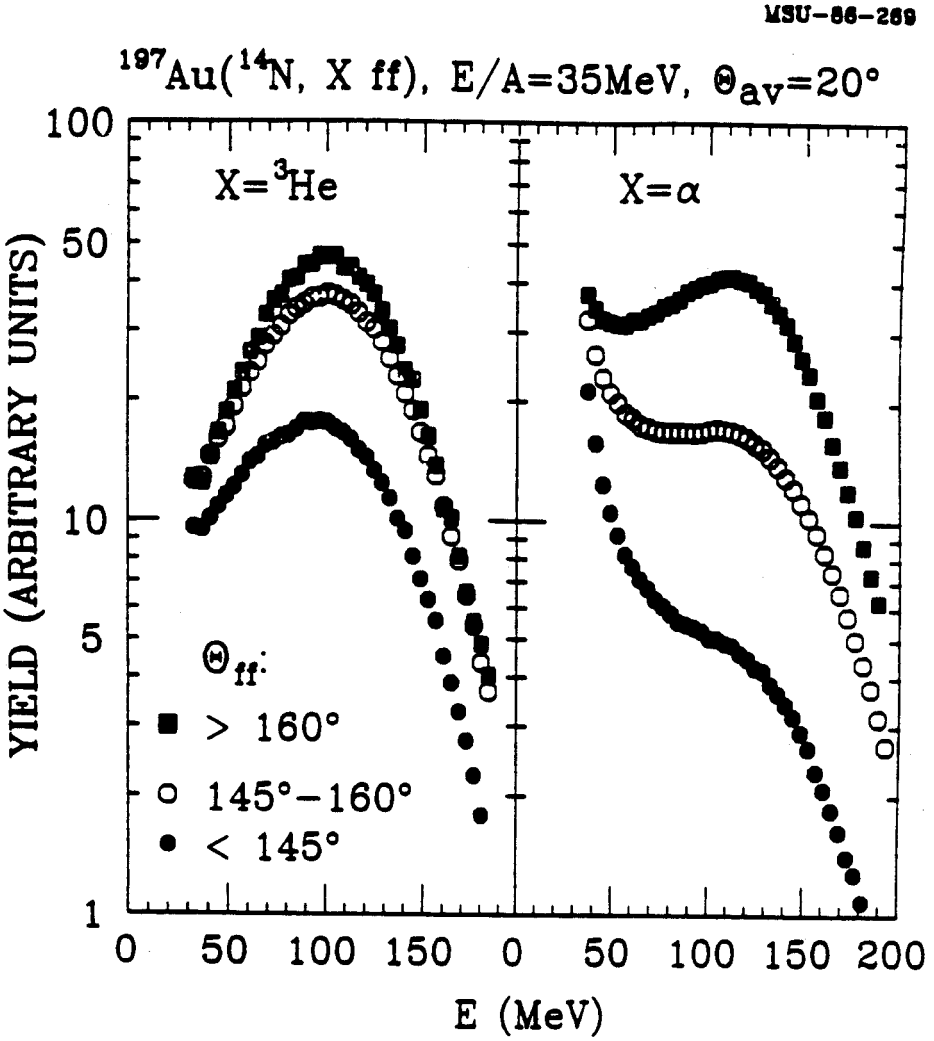

Figure VIII.4 Yields of ^{3}He and ^{4}He nuclei summed over all elements of the hodoscope with the center of the hodoscope positioned at Θ_{av}=20°. The distributions are shown for the three gates on folding angle defined in Figure VIII.2.

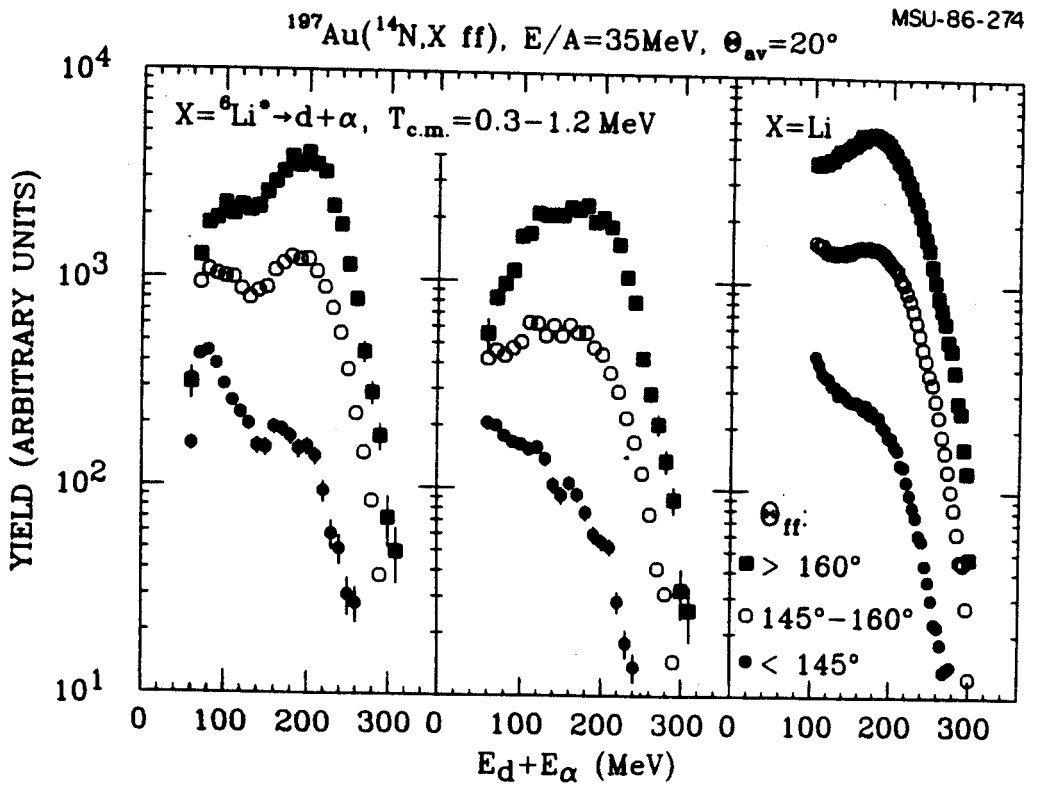

Figure VIII.5 Left hand part: Dependence of the α-d coincidence yield on the total kinetic energy, $E_\alpha+E_d$, for α-d pairs which can be attributed to the decay of the 2.816 MeV state in ^{6}Li. Center part: Same as left hand part, but corrected for the variation of the hodoscope efficiency with $E_\alpha+E_d$. Right hand part: Yields of lithium nuclei summed over all elements of the hodoscope. The distributions are shown for the three gates on folding angle defined in Figure VIII.2. The center of the hodoscope was positioned at θ_{av}=20°.

Figure VIII.5 shows the spectrum of particle stable Li nuclei. The left hand part of the figure shows the dependence of the measured α-d coincidence yield on the total kinetic energy, $E_\alpha+E_d$, for α-d pairs which can be attributed to the 2.186 MeV state in ^{6}Li. (This yield was obtained by placing a gate on the relative kinetic energy of the two coincident particles, $E_{rel}= q^2/2\mu$ = 0.3-1.2 MeV, and subtracting the "background" coincidence yield, see also Eq. IV.19) The yields shown in the center part of the figure were corrected for the energy dependence of the hodoscope efficiency.

Energy spectra gated by large folding angles, i.e. by small linear momentum transfers (gate 3, $\Theta_{ff}>160°$), exhibit pronounced quasi-elastic components centered close to the projectile velocity. These components are strongly suppressed by gating on small folding angles, i.e. large linear momentum transfers (gate 1, $\Theta_{ff}<145°$). These observations support the intuitive picture which associates large folding angles with collisions at large impact parameters for which break-up reactions or sequential decays of excited projectile residues are important. Smaller folding angles, on the other hand, are associated with less peripheral and more violent collisions in which a major part of the projectile momentum is absorbed by the heavy target nucleus. In general, gate 1 serves as an effective filter condition to suppress the quasi-elastic, beam velocity components in the energy spectra. Since beam velocity particles can also be emitted in absorptive breakup or massive transfer reactions characterized by large momentum transfers to the heavy reaction residue, the suppression of the beam velocity component is not perfect. In fact, small residual beam velocity components can be discerned in most of the gated energy spectra. It is remarkable that the

^{3}He energy spectra are dominated by the beam velocity component irrespective of the gating condition, see Figure VIII.3. Possibly, ^{3}He nuclei are preferentially produced in more direct reactions and only to a lesser extent in statistical emission processes.

Figure VIII.6 shows the differential yields, $d^2Y(E,\theta)/dEd\Omega$, of α-particles and lithium nuclei emitted at forward angles and gated by the three constraints on folding angle. In order to be able to make reasonable assumptions about the distributions of particle unstable ^{5}Li and ^{6}Li nuclei, we have fit these yields with the parametrization of Eq. V.1. The fits are shown by the solid lines in Figure VIII.6; the parameters are listed in Table 10.

8.3 FILTERED TWO-PARTICLE CORRELATION FUNCTIONS

Figures VIII.7 and VIII.8 show the α-d and p-p correlation functions measured for large (gate (1), open points) and small (gate (3), solid points) linear momentum transfers to the heavy reaction residue. In order to reduce contributions from later stages of the reaction for which sequential emission of low energy particles from the fully equilibrated composite system may be important, these correlations were gated on total energies well above the compound nucleus Coulomb barrier: $E_\alpha+E_d \geq 100$ MeV and $E_{p1}+E_{p2} \geq 50$ MeV. The selection of events with large linear momentum transfer produces enhanced maxima in both correlation functions as compared to those with low momentum transfer. For the α-d correlation function, the sharp peak at $q \approx 42$ MeV/c is enhanced by about a factor of two. For the p-p correlation function, the enhancement is less dramatic but still appreciable. A similar enhancement is also observed for the α-p correlation function (see

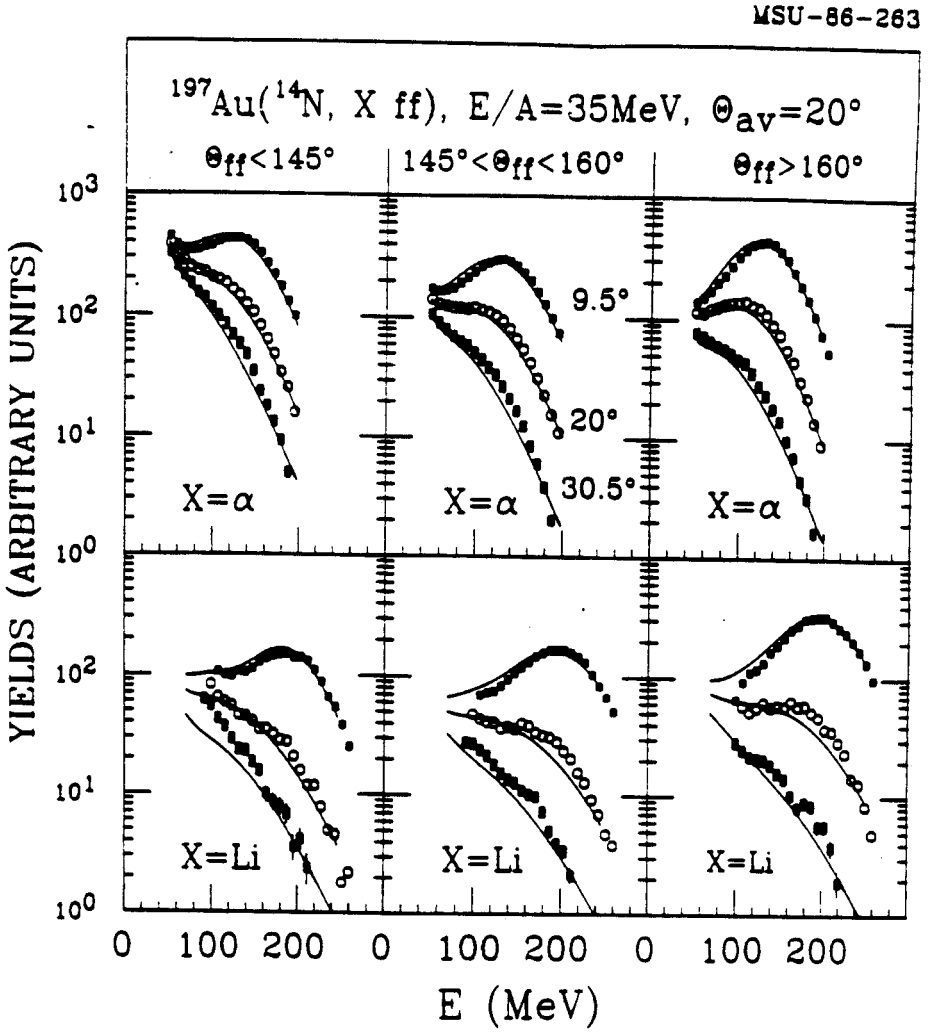

Figure VIII.6 Differential yields, $d^2Y(E,\theta)/dEd\Omega$, of α-particles and lithium nuclei emitted at forward angles and gated by the three folding angle gates. The solid lines show fits with the parametrization of Eq. V.1. The parameters are listed in Table 10.

TABLE 10

Parameters of Eq. V.1 used to fit the single particle cross sections gated by folding angles of the fission fragments for the reaction $^{14}N + ^{197}Au$ at E/A=35 MeV shown in Figure VIII.6.

Part. (Gate)	U_c [MeV]	τ_1 [MeV]	v_1/c	N_1 [a.u.]	τ_2 [MeV]	v_2/c	N_2 [a.u.]	τ_3 [MeV]	v_3/c	N_3 [a.u.]
α (1)	16.1	8.0	0.002	346.6	16.7	0.118	43.26	6.1	0.233	8.553
α (2)	"	8.0	0.017	265.0	13.8	0.150	66.06	6.1	0.236	29.99
α (3)	"	8.0	0.000	146.0	11.8	0.168	23.70	5.0	0.236	14.79
Li (1)	"	9.8	0.040	37.5	13.9	0.149	18.57	3.6	0.220	6.62
Li (2)	"	13.4	0.054	10.8	13.2	0.166	6.16	4.7	0.227	3.87
Li (3)	"	14.9	0.071	62.2	11.2	0.187	33.23	4.2	0.228	27.7

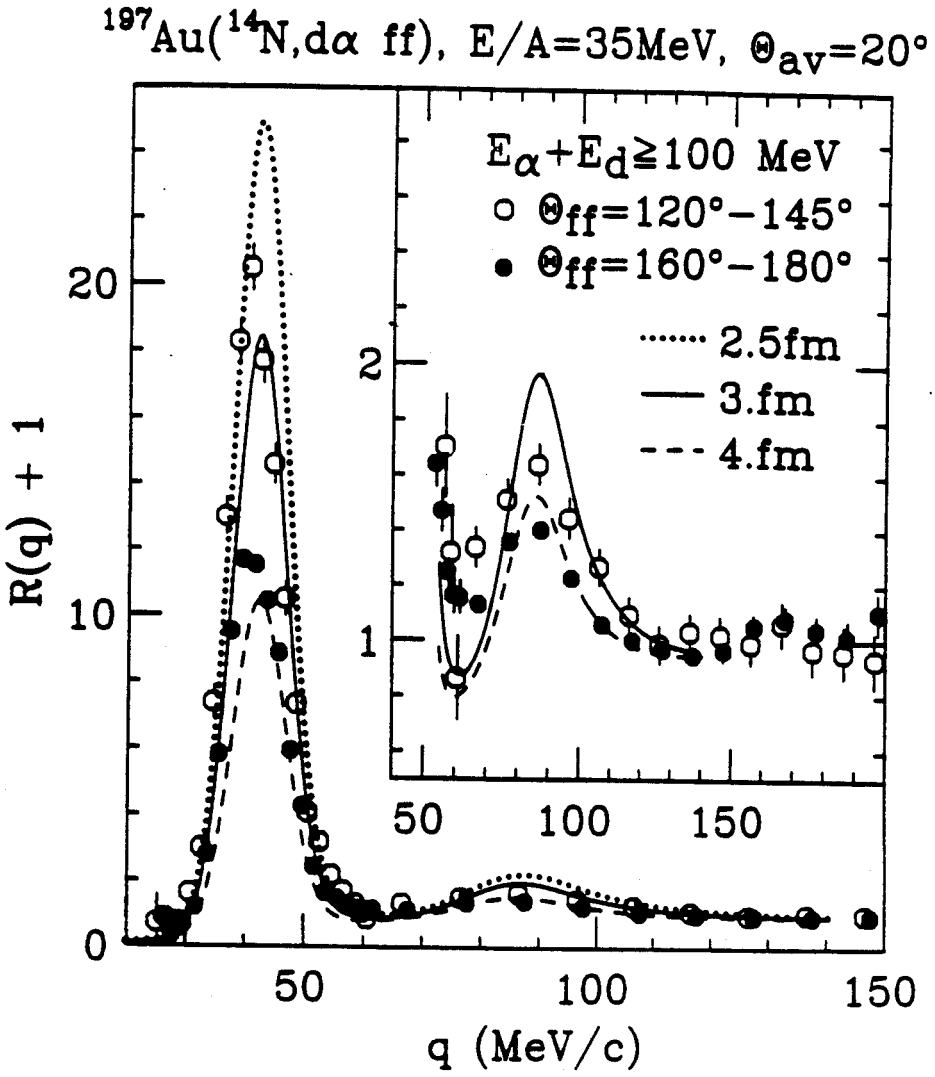

Figure VIII.7 α-d correlation functions gated on large (gate (1): open points) and small (gate (3): solid points) linear momentum transfers to the heavy reaction residue. The gate on the total kinetic energy is indicated in the figure; the curves are explained in the text (see Eq. II.12).

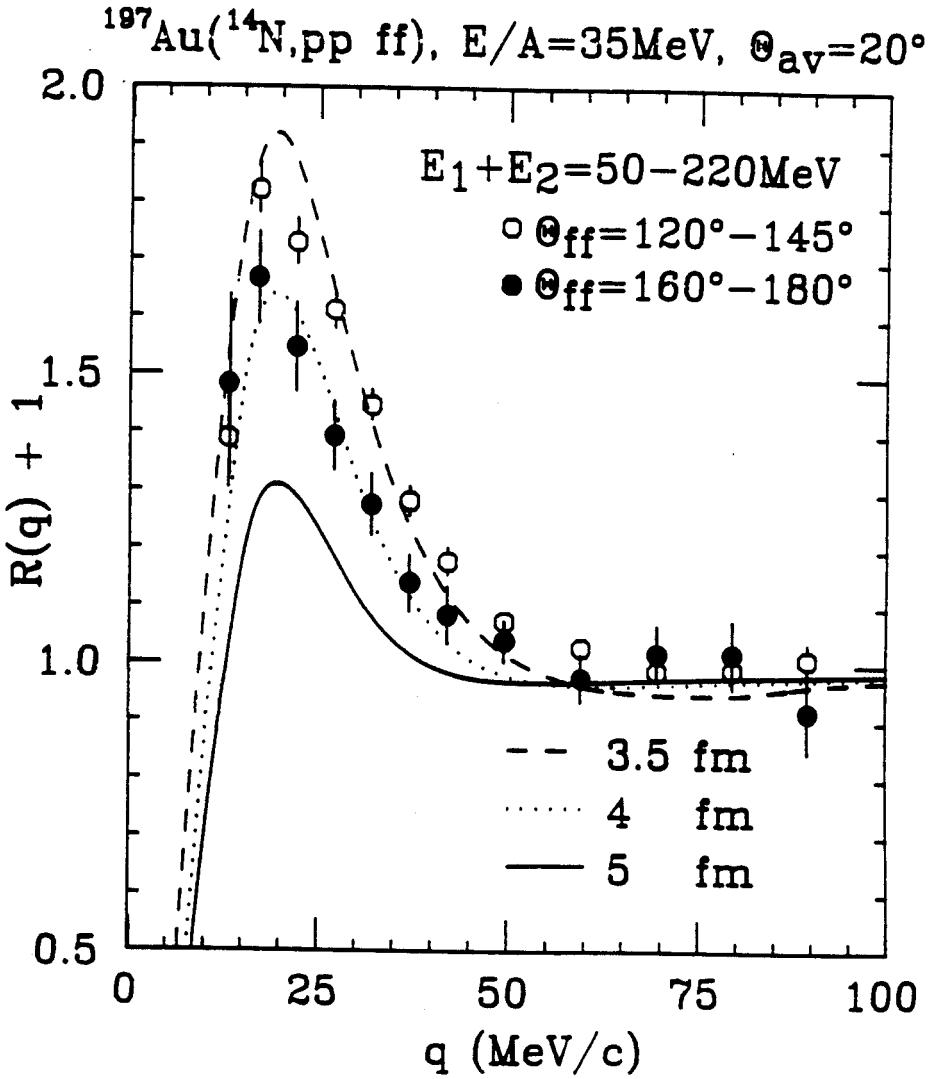

Figure VIII.8 p-p correlation functions gated on large [gate (1): open points] and small [gate (3): solid points] linear momentum transfers to the heavy reaction residue. The gate on the total kinetic energy is indicated in the figure; the curves are explained in the text (see Eq. II.12).

Figure VIII.17). The curves shown in Figures VIII.7 and VIII.8 represent theoretical correlation functions predicted by the final-state interaction model of Koonin [Koon 1977] and its extension [Boal 1986] to particles heavier than protons (see Eq. II.12). The theoretical α-d correlations include corrections for the finite resolution of the hodoscope.

For the case of p-p correlations, source radii of $r_0 \approx 3.7$ and 4.0 fm are extracted for gates (1) and (3), respectively. Source radii extracted from the sharp peak of the α-d correlation function at $q \approx 42$ MeV/c are $r_0 \approx 2.8$ and 3.6 fm, respectively, for gates (1) and (3). Since the exact height of the theoretical α-d correlation function depends on the instrumental line shape, we have extracted these latter source radii from the integral correlation, $R_{eff} = \int dq \cdot R(q)$, with the integration performed over the range of $q \approx 30$-60 MeV/c. The extracted source sizes are generally smaller than the size of the target nucleus [Brow 1984] $\left[r_0(Au) = \sqrt{2/3} \cdot r_{rms}(Au) \approx 4.4 \text{ fm}\right]$. A strictly geometric interpretation of our results would imply that quasi-elastic collisions are characterized by sources significantly larger than the size of the projectile nucleus [Brow 1984] $\left[r_0(N) \approx 2.1 \text{ fm}\right]$. It is, however, likely that temporal effects cannot be neglected when interpreting these results. The time scales characteristic of preequilibrium particle emission in violent fusion-like collisions may be shorter than those which characterize particle emission in quasi-elastic reactions thus producing stronger correlations and smaller apparent source radii. Our observation of reduced correlations for peripheral processes may, therefore, reflect longer emission time scales rather than larger source dimensions. The sequential decay of excited projectile residues is an

example for reactions which proceed via longer emission time scales. For such processes, Koonin's formulation may be less useful for the calculation of two-particle correlation functions and alternative statistical formulations, such as appropriate generalization of the Hauser-Feshbach theory, could be explored. For the case of equilibrium decay of light compound nuclei, Hauser-Feshbach calculations have predicted [Bern 1985] smaller two-proton correlations than expected from the zero-lifetime limit of Koonin's model. Within Koonin's model, reduced correlations are expected due to the long lifetime of the compound nucleus. From these arguments, one expects reduced correlations for peripheral collisions for which contributions from the decay of equilibrated projectile residues may be important. For fusion-like collisions, on the other hand, such processes are suppressed. It is significant that these collisions exhibit larger correlations. They should reflect, more clearly, the space-time localization of the reaction.

Figure VIII.9-VIII.13 show the energy dependence of α-d correlation functions under different constraints: inclusive, gated by any fission events, and gated by three ranges of folding angle indicated in Figure VIII.2. These extracted source radii are summarized in Figure VIII.14, which shows the dependence of α-d correlations on the total energy per nucleon, $(E/A)_{tot}=(E_{\alpha}+E_{d})/6$, of the two coincident particles. Inclusive [Chit 1986b] correlations and correlations measured in coincidence with fission fragments are shown in the right and left hand parts of the figure, respectively. The left hand scale of the figure gives the integral correlation, $R_{eff}= \int dq \cdot R(q)$. The right hand scale of the figure gives source radii extracted with the model of Ref. [Boal 1986]. At low

energies, the α-d correlations are of comparable magnitude. For small linear momentum transfers (gate 3), they are nearly independent of energy. On the other hand, the α-d correlations for larger linear momentum transfers vary strongly with energy. For inclusive correlations, right hand part of Figure VIII.14, a similar energy dependence exists [Chit 1986, Lync 1983] and becomes more pronounced at larger angles, Θ_{av}, where contributions from quasi-elastic processes become less important. It was argued [Bond 1984] that the energy dependence of inclusive two-particle correlations could be due to increasing contributions from the decay of excited projectile residues. Our observation of increasing two-particle correlations in violent fusion-like collisions and nearly energy independent correlations for quasi-elastic collisions refutes that argument.

8.4 FILTERED EMISSION TEMPERATURES

Since fission fragments are preferentially emitted in the entrance channel scattering plane [Tsan 1984], the assumption of isotropic decay of particle unstable states can be addressed more sensitively for decays measured in coincidence with fission fragments. By gating on different ranges of folding angles one may also explore whether the assumption of isotropic decay is only violated for specific classes of reactions. This information is important for the extraction of the relative populations of states. It can be evaluated for the decay of the sharp 2.186 MeV state in ^{6}Li. For this state, uncertainties due to the subtraction of the uncorrelated background are minimal.

Figure VIII.15 shows the dependence of the α-d coincidence yield from the decay of $^{6}Li_{2.816} \rightarrow \alpha$+d as a function of the angles Θ_R and Φ_R

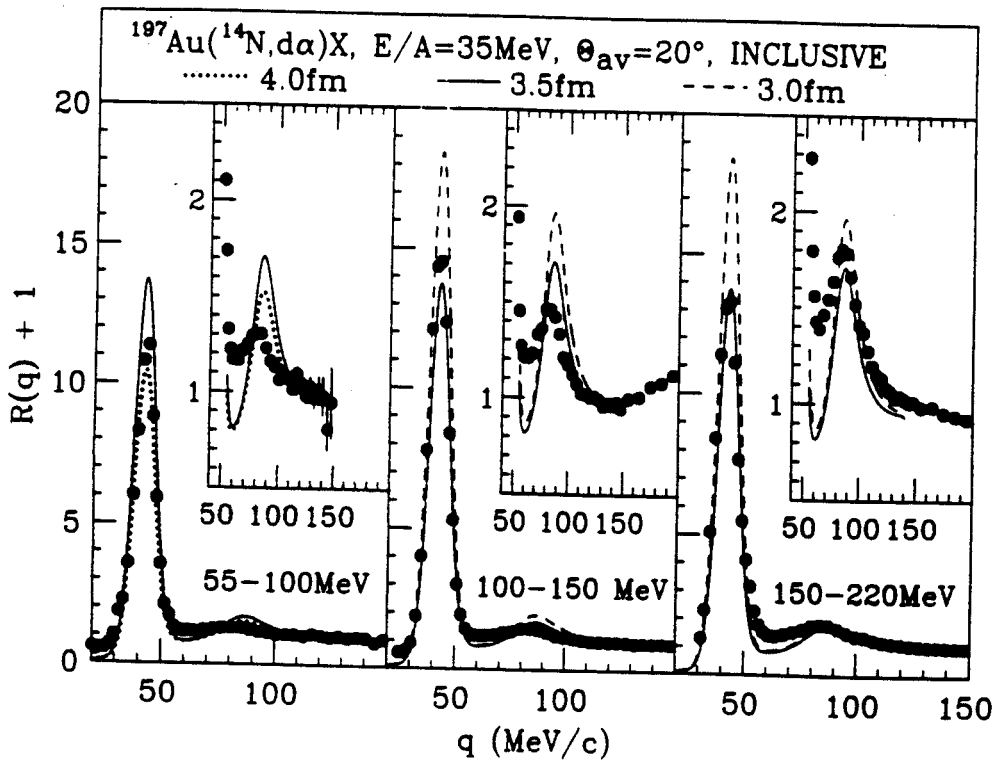

Figure VIII.9 Inclusive α-d correlation functions measured at Θ_{av}=20°. The constraints placed on $E_\alpha + E_d$ are indicated in the figure. The curves are theoretical calculations of Eq. II.12 with source radii indicated in the figure.

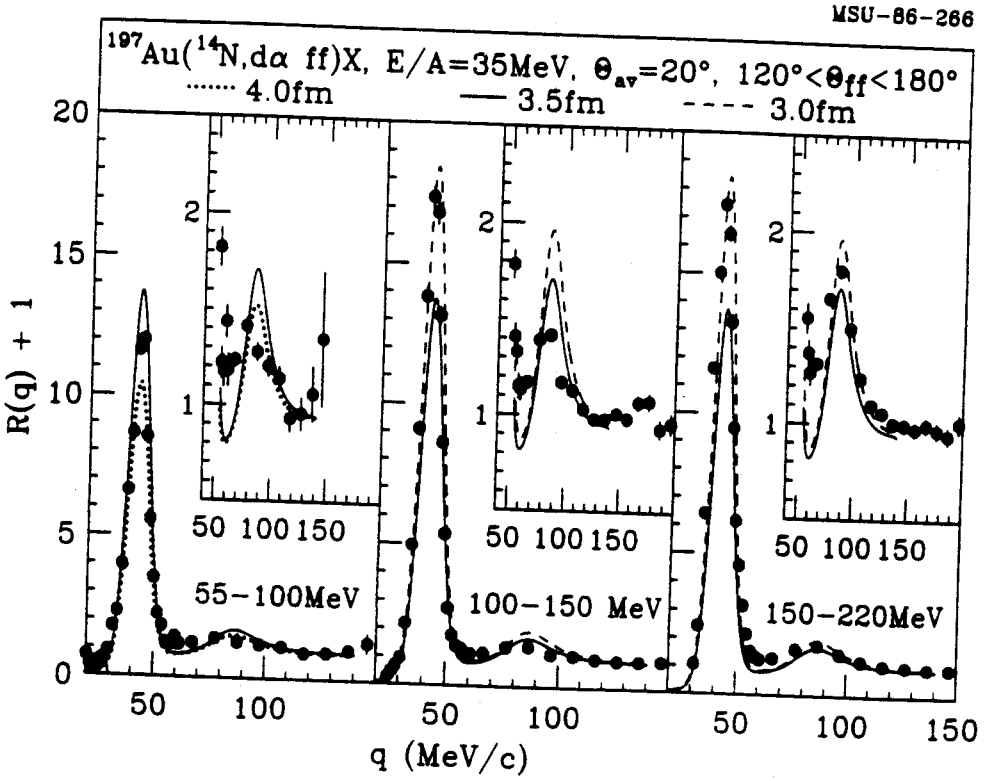

Figure VIII.10 α-d correlation functions measured at Θ_{av}=20° in coincidence with fission fragments. No gates are set on Θ_{ff}. The constraints placed on $E_\alpha + E_d$ are indicated in the figure. The curves are theoretical calculations of Eq. II.12 with source radii indicated in the figure.

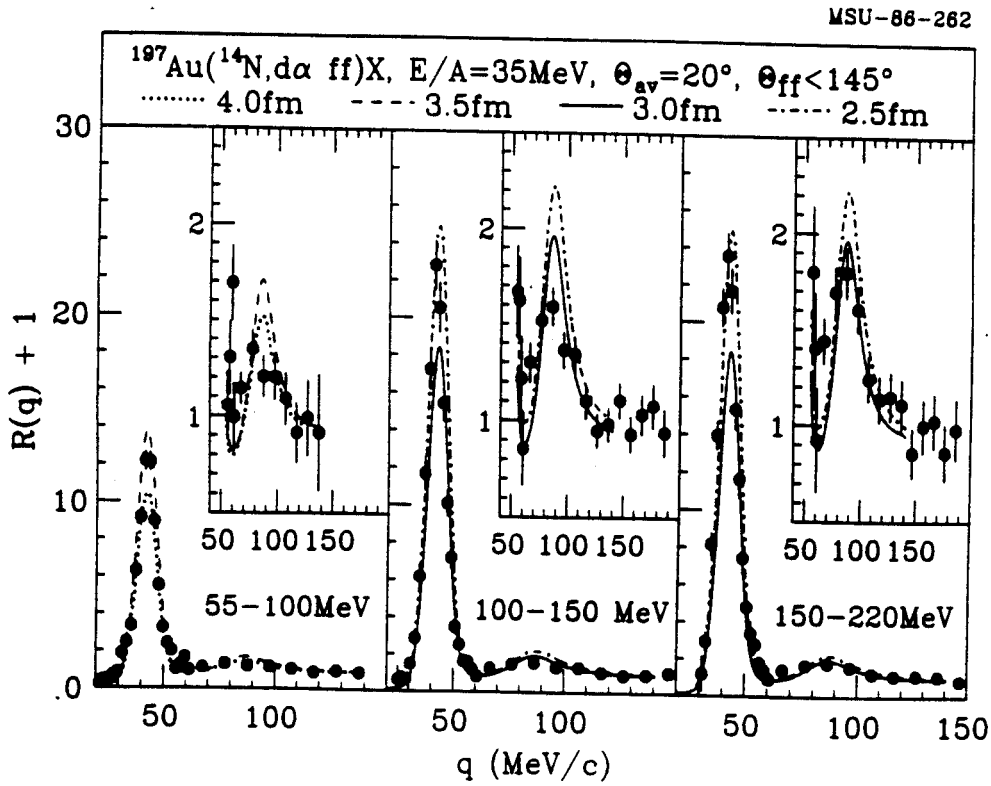

Figure VIII.11 α-d correlation functions measured at Θ_{av}=20° in coincidence with fission fragments gated by Θ_{ff}<145°. The constraints placed on $E_\alpha + E_d$ are indicated in the figure. The curves are theoretical calculations of Eq. II.12 with source radii indicated in the figure.

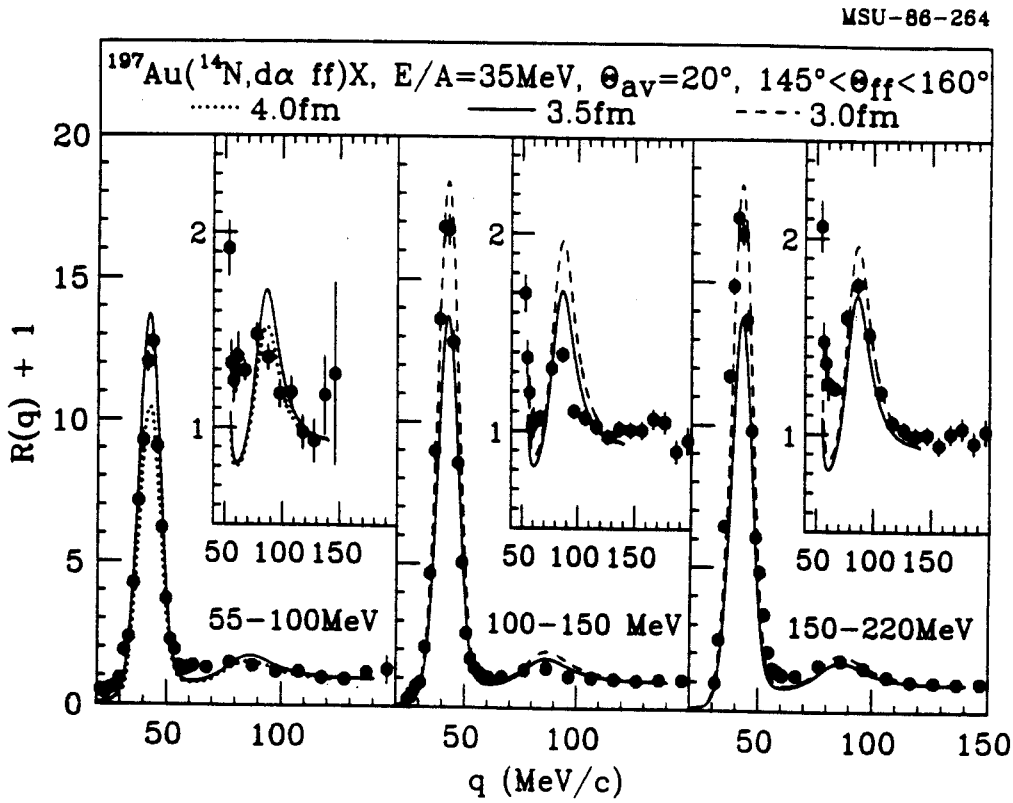

Figure VIII.12 α-d correlation functions measured at θ_{av}=20° in coincidence with fission fragments gated by 145°<θ_{ff}<160°. The constraints placed on E_α+ E_d are indicated in the figure. The curves are theoretical calculations of Eq. II.12 with source radii indicated in the figure.

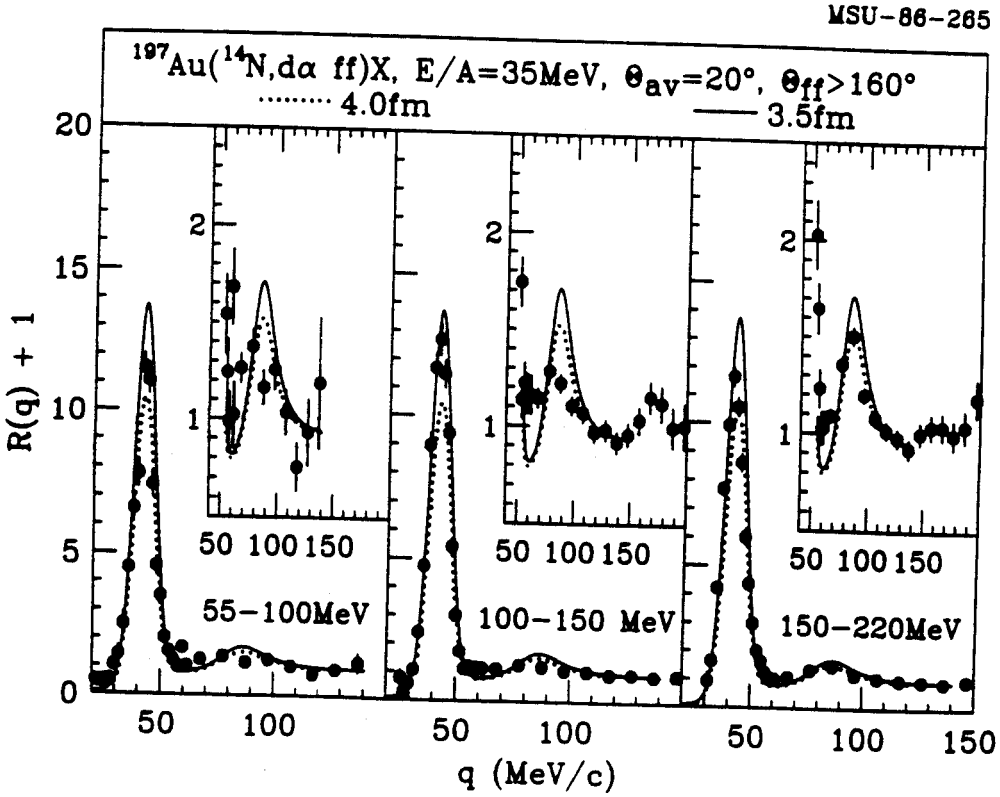

Figure VIII.13 α-d correlation functions measured at θ_{av}=20° in coincidence with fission fragments gated by θ_{ff}>160°. The constraints placed on E_α+ E_d are indicated in the figure. The curves are theoretical calculations of Eq. II.12 with source radii indicated in the figure.

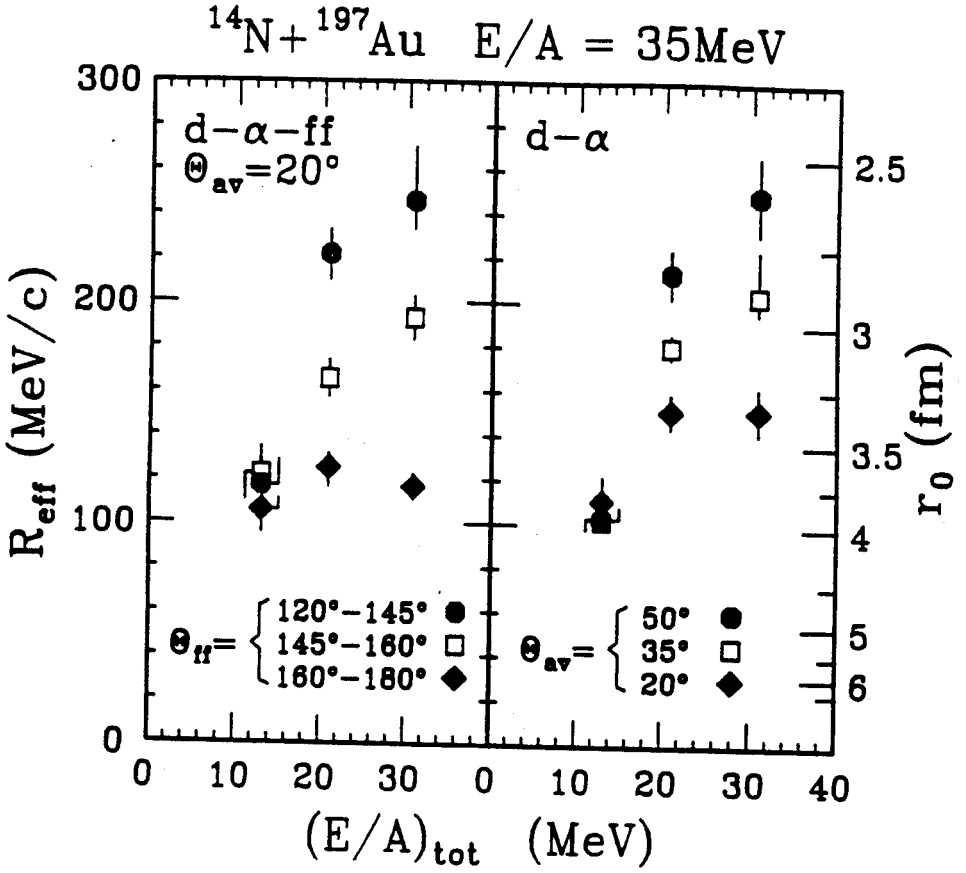

Figure VIII.14 Dependence of α-d correlations on the total energy per nucleon, $(E/A)_{tot}=[E_\alpha+E_d]/6$, of the two coincident particles. Correlations measured inclusively and in coincidence with fission fragments are shown in the right and left hand parts, respectively. The left hand scale corresponds to $R_{eff}=\int dq \cdot R(q)$, with the integration performed over the range of q=30-60 MeV. The right hand scale gives source radii extracted with the final-state interaction model, Eq. II.12. Data for Θ_{av}= 35° and 50° were taken from [Chit 1986b].

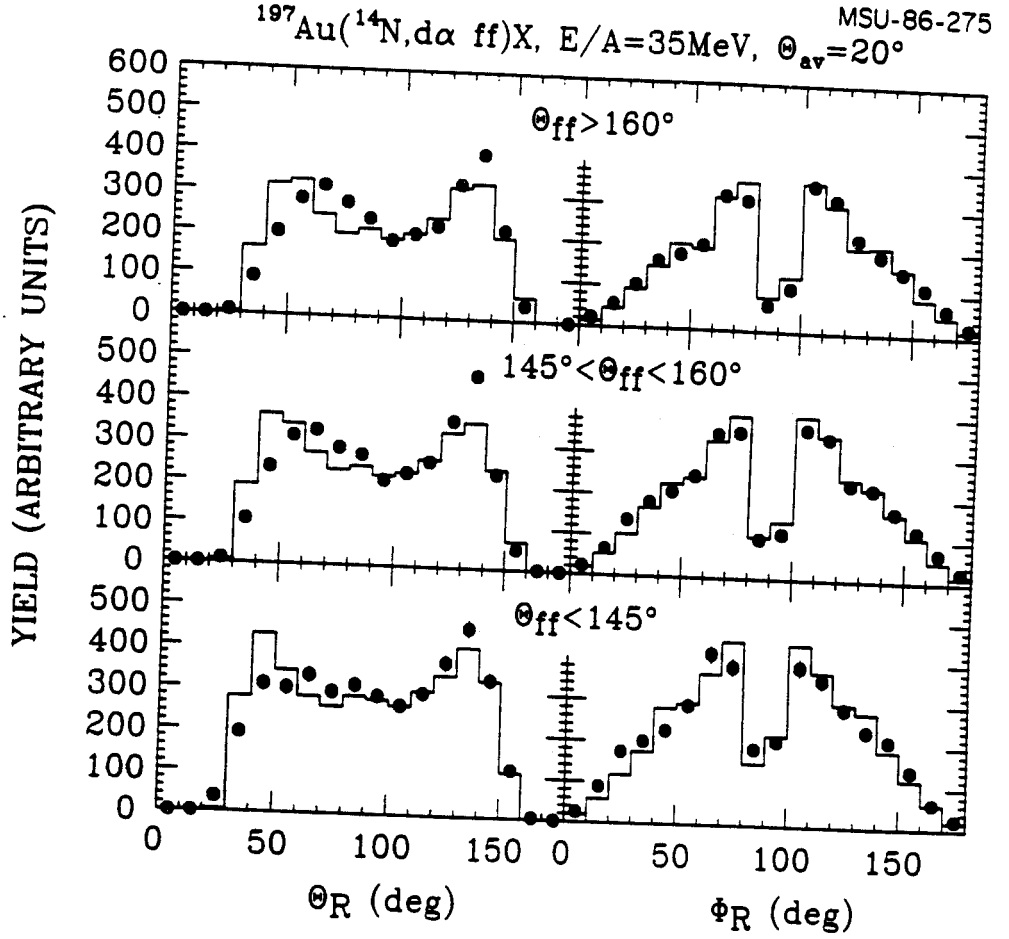

Figure VIII.15 Angular distributions of the α-d yields resulting from the decay $^6Li^*_{2.186} \rightarrow$ α+d, gated on the three different gates on folding angle defined in Figure VIII.2. The angles Θ_R and Φ_R were defined in Eqs. IV.17-IV.18 (see also Figure VII3). The histograms show the results of Monte Carlo calculations in which the ^{6}Li nuclei are assumed to decay isotropically in their respective rest frames.

defined in Eqs. IV.17-IV.18. These yields were gated by the three constraints on folding angle defined in Figure VIII.2. The histograms show the results of Monte Carlo calculations based on the assumption of isotropic decay in the rest frame of the parent nucleus. In these calculations, the differential cross sections for the emission of the primary $^6Li_{2.186}$ nuclei were extrapolated in terms of the moving source parameterization, Eq. V.1, using the parameters given in Table 9. The calculations are in good agreement with the data; remaining small discrepancies can be attributed to uncertainties of the energy calibrations. No evidence can be established for significant violations of the assumption of isotropic decay.

In order to extract emission temperatures, we determined the $^6Li^* \rightarrow \alpha+d$ coincidence yields, N_L and N_H, integrated over the energy ranges of $T_{c.m.}$=0.3-1.45 and 1.5-6.25 MeV, respectively. The shaded horizontal bands in Figure VIII.16 show the yield ratios, N_L/N_H, extracted for events selected by the three folding angle gates defined in Figure VIII.2. The additional constraint, $E_\alpha + E_d \geq 100$ MeV, was applied to reduce contributions from the decay of equilibrated target nuclei. The widths of the shaded bands reflect uncertainties of the background subtraction caused by limited coincidence statistics at large relative momenta. The solid lines show the temperature dependence of the coincidence yield ratios predicted for thermal distributions, see Eq. IV.20. The shaded vertical bands in Figure VIII.16 indicate the range of temperatures consistent with the experimental yield ratios; typical values are of the order of 4 MeV. These temperatures have considerable uncertainties due to the small energy separation of the states considered. Additional systematic errors could be caused by sequential

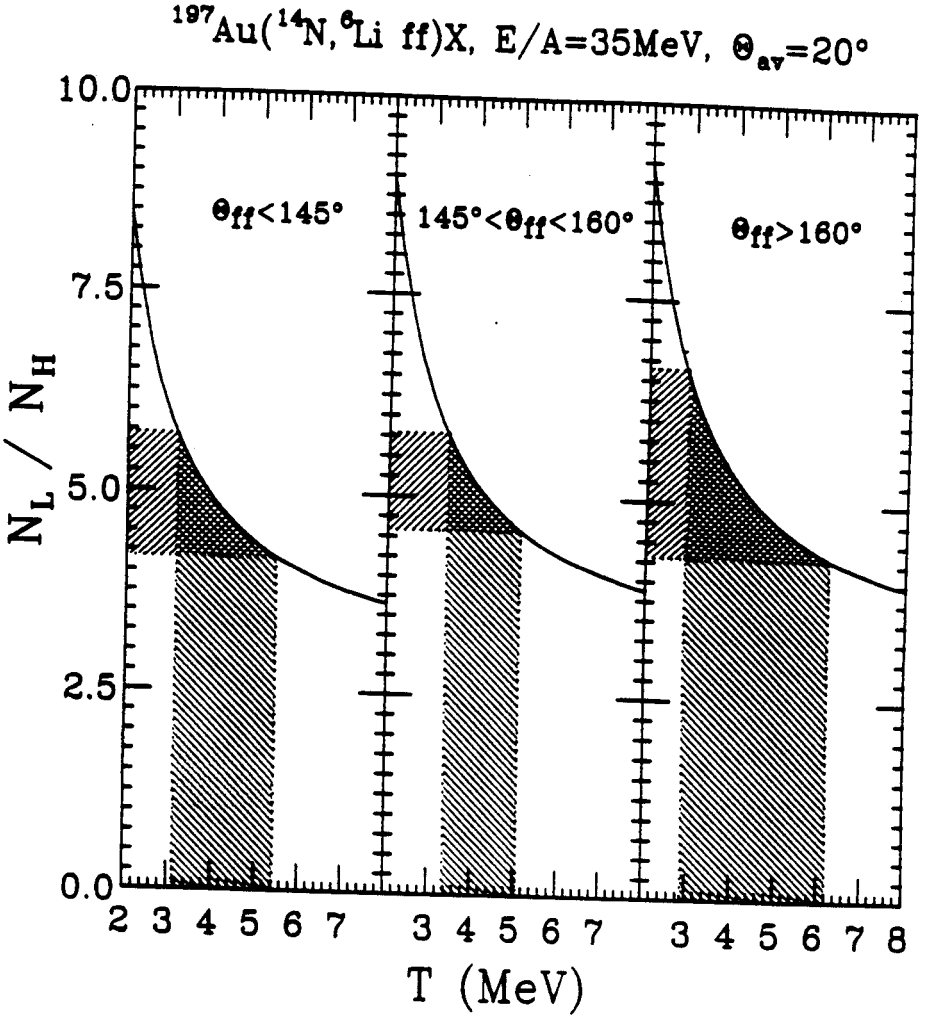

Figure VIII.16 Ratios N_L/N_H, of measured α-d coincidence yields resulting from the decays of particle unstable ^{6}Li nuclei. The yields N_L and N_H were integrated over the energy ranges of $T_{c.m.}$ = 0.3-1.45 and 1.5-6.25 MeV, respectively. Gates on folding angle are given in the figure. The hatched regions indicate the experimental values. The solid curves show the temperature dependences of yields predicted by Eq. IV.20.

feeding from higher lying particle unstable states [Hahn 1987, Fiel 1987].

More accurate temperature determinations could be made from the relative populations of the ^{5}Li ground state, $^5Li_{gs} \rightarrow \alpha+p$, and the 16.7 MeV state, $^5Li_{16.7} \rightarrow d+^3He$. Unfortunately, the detector geometry of this experiment had not been optimized for the detection of the decay of the 16.7 MeV state in ^{5}Li which lies close to the $d+^3$He threshold. Because of the relatively large angular separation between adjacent detectors, $\Delta\Theta=6.1°$, the thresholds on the total kinetic energy were lowered to $E_{d+^3He} = E_{p+\alpha} = 52$ MeV. The dependence of the extracted emission temperatures on the total kinetic energy could not be explored.

Figures VIII.17 and VIII.18 show the α-p and d-^{3}He correlations functions, respectively, gated by the three constraints on folding angles defined in Figure VIII.2. The broad peak in the α-p correlation function at q≈50 MeV/c corresponds to the decay $^5Li_{gs} \rightarrow \alpha+p$; the maximum of the d-^{3}He correlation function at small relative momenta is due to the decay $^5Li_{16.7} \rightarrow d+^3He$. The coincidence yields, N_L and N_H, from the decays of the low-lying ground state and the high-lying 16.7 MeV state, respectively, were extracted according to Eq. IV.19. The extreme limits within which the background correlation functions were assumed to vary are shown by the dashed curves in Figures VIII.17 and VIII.18. The extracted yield ratios, N_L/N_H, are shown by the shaded horizontal bands in Figure VIII.20.

For measurements close to the grazing angle, the shapes of the energy spectra of particle stable nuclei change rapidly with detection angle, see Figure VIII.6. In addition, they depend sensitively on the folding angle gate, see Figures VIII.3-VIII.5. Since stable ^{5}Li nuclei

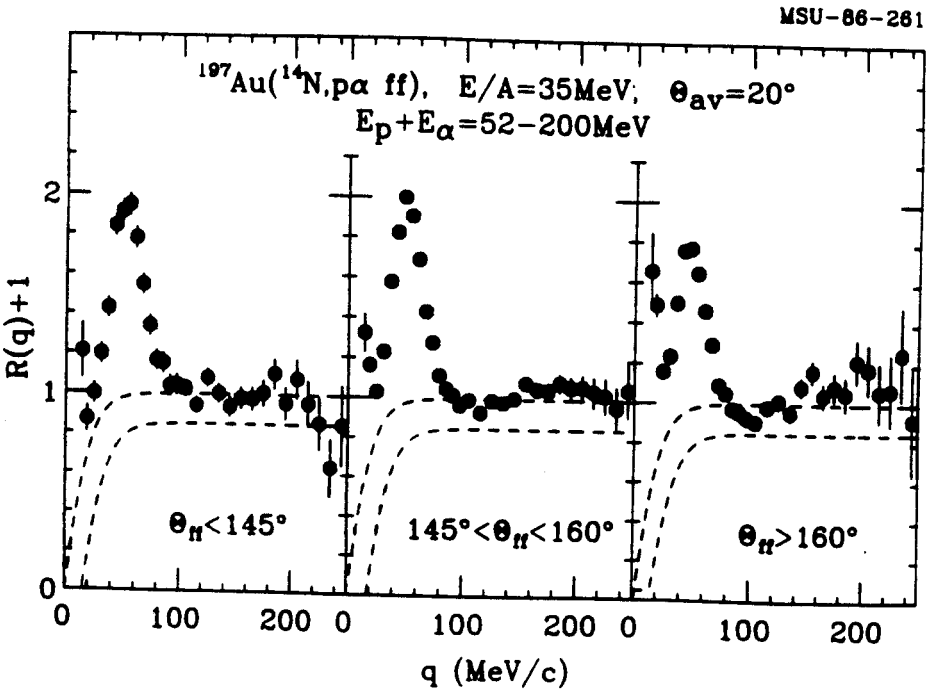

Figure VIII.17 p-α correlation functions measured in coincidence with two fission fragments. The gates on folding angle are given in the figure. The dashed lines indicate the bounds within which the background correlation function was assumed to lie.

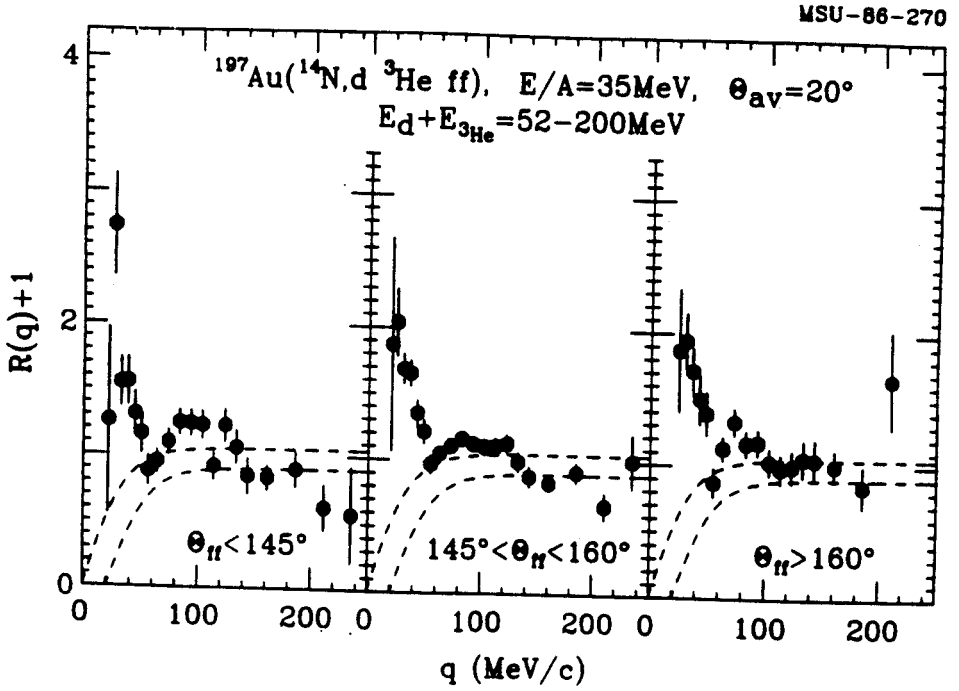

Figure VIII.18 d-^{3}He correlation functions measured in coincidence with two fission fragments. The gates on folding angle are given in the figure. The dashed lines indicate the bounds within which the background correlation function was assumed to lie.

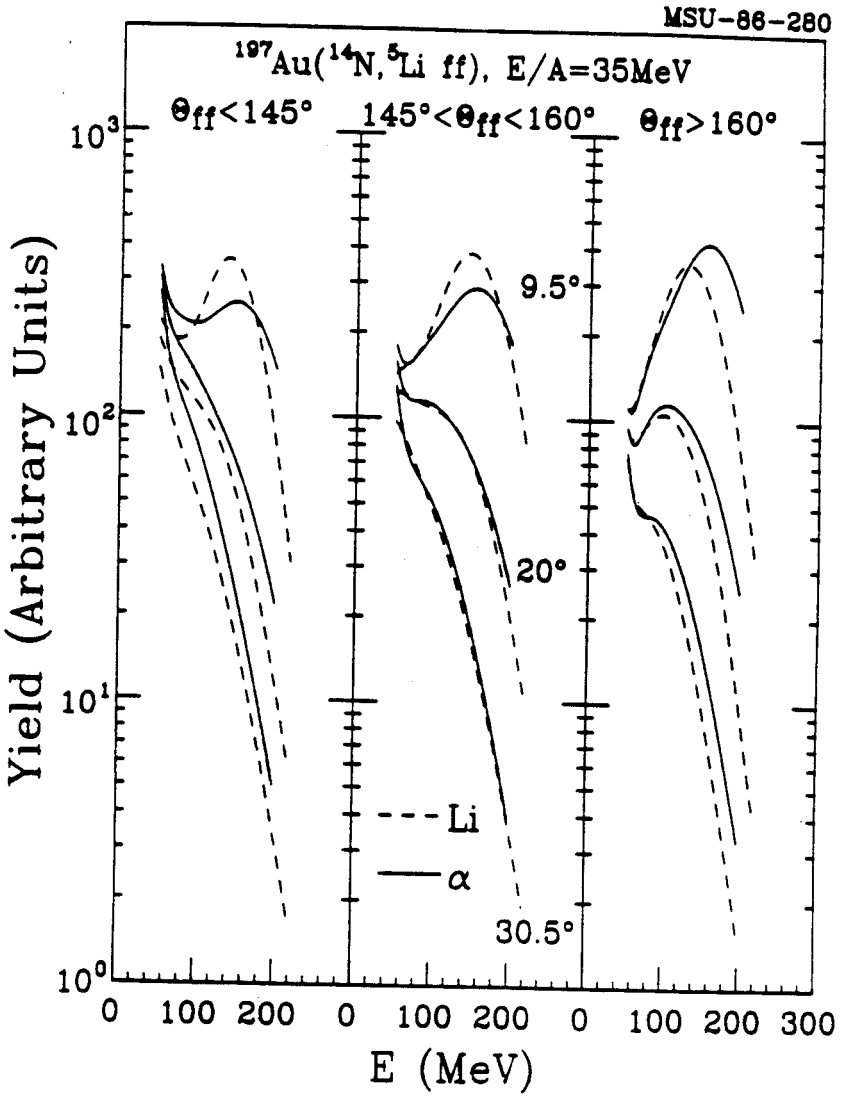

Figure VIII.19 ^{5}Li parent distributions assumed for the efficiency calculations shown by the solid and dashed lines in Figure VIII.20.

do not exist, the shapes of the energy and angular distributions of the emitted ^{5}Li parent nuclei are not known. We have assumed that the ^{5}Li parent distributions could be described in terms of a superposition of three Maxwellian distributions, Eq. V.1, the parameters of which were taken from fits to the α-particle and Li cross sections shown in Tab. 9. The extrapolated ^{5}Li distributions are shown by the solid and dashed curves in Figure VIII.19. The solid curves represent distributions calculated by using source parameters extracted from fits to the α-particle yields; the dashed curves represent distributions calculated with parameters from fits to the Li yields. The differences between the two calculations illustrate the large uncertainties which have to be attributed to the ^{5}Li parent distributions. However, relative detection efficiencies are rather insensitive to the detailed shape of the parent distributions. This is illustrated by the solid and dashed curves in Figure VIII.20 which show the temperature dependence of thermal yields ratios, Eq. IV.20, predicted for the two sets of parent distributions. The two predicted yield ratios are nearly indistinguishable. It is, therefore, possible to extract emission temperatures from the relative populations of states in ^{5}Li in spite of existing large uncertainties about the shape of the parent distributions.

The shaded vertical bands in Figure VIII.20 indicate the ranges of emission temperatures which are consistent with our assumptions on the background correlation functions. The temperatures extracted for the three gates on folding angles are of the order of 4-5 MeV. These values are consistent with those extracted from the decays of particle unstable ^{6}Li nuclei. The surprising similarity of emission temperatures extracted for peripheral and fusion-like collisions could be related to the fact

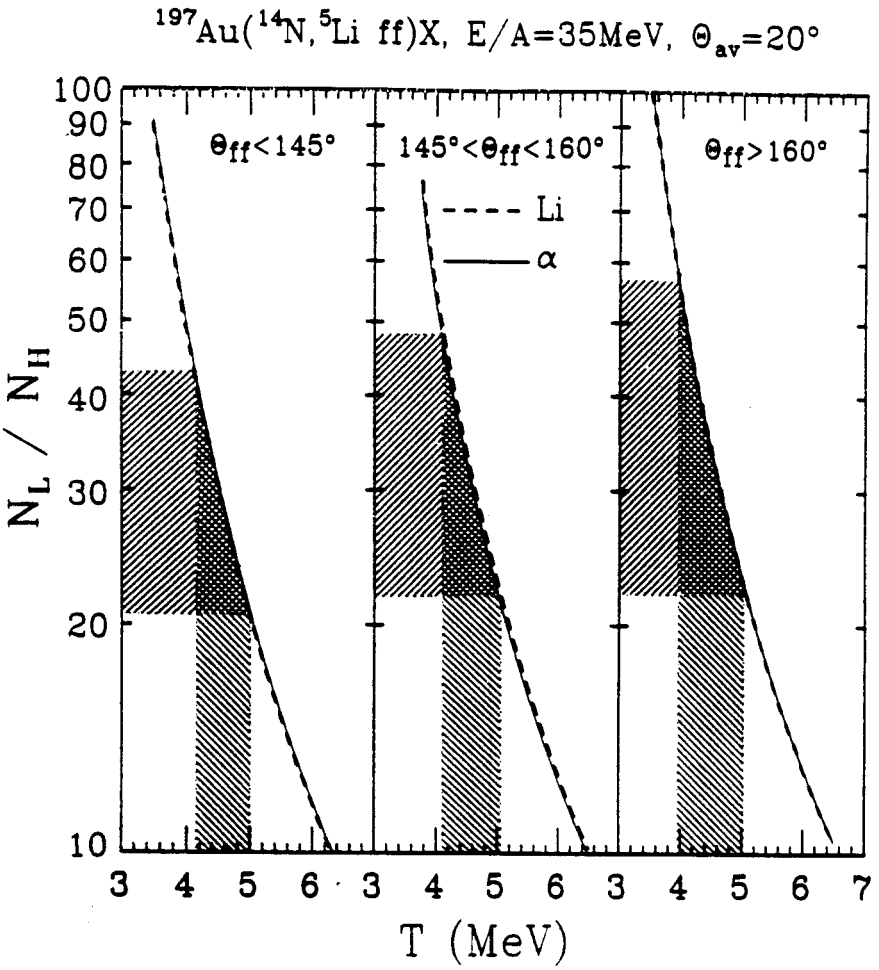

Figure VIII.20 Yield ratios N_L/N_H for the detection of the decays $^5Li_{gs} \rightarrow \alpha+p$ and $^5Li_{16.7} \rightarrow d+^3He$ in coincidence with two fission fragments. The gates on folding angle are given in the figure. The hatched regions indicate the range of values consistent with our assumptions on the background correlation functions shown in Figure VIII.17-VIII.18. The solid and dashed curves show the temperature dependences of yields predicted by Eqs. IV.20 assuming parent distributions given by Eq. V.1 with parameters extracted from fits to the α-particle and Li distributions shown in Figure VIII.6. The parameters are given in Table 10.

that our fission filter suppresses the most gentle types of collisions. It was already stressed before that the study of such gentle collisions requires the use of more fissile targets. It is worth noting that emission temperatures have also been shown to be rather insensitive to the multiplicity of charged particles emitted at forward angles [Sain 1988].

CHAPTER 9. SEQUENTIAL FEEDING AND TEMPERATURE DETERMINATIONS

Temperatures determined from relative populations of states can have large uncertainties whenever the final populations of states differ significantly from the primary ones. The resulting uncertainties are expected to be smaller when temperatures are extracted from the relative populations of states separated by energies, ΔE, much larger than the temperature, T, of the emitting source. Because of the exponential factor in Eq. II.16, T is less sensitive to the change of $R_{1,2}$ by the feeding if ΔE is large [Poch 1985a].

Perturbations of the primary populations of states can, for example, arise from final state interactions among the emitted particles [Boal 1985] and/or feeding from higher lying states [Morr 1984,Morr 1986, Poch 1985a, Poch 1987, Xu 1986, Fiel 1987, Hahn 1987]. Perturbations due to final state interactions are difficult to assess since they depend on the detailed space-time evolution of the final stages of the reaction [Boal 1985]. It is often assumed that they are small as compared to those caused by sequential feeding. However, the full extent of feeding from high lying particle unbound states is also not known. It must be calculated. Previous calculations [Hahn 1987, Fiel 1987] have evaluated the effects of feeding from known particle unbound states of nuclei with charge $Z \leq 10$.

The results of recent calculations [Hahn 1987, Fiel 1987] are shown in Figure IX.1. The figure shows the temperature dependence of the normalized population ratio of states, R_p/R_∞, where R_∞ is the high temperature limit of the primary population ratio. The solid curves show the primary population ratios. The dashed and dotted-dashed curves show the results of quantum statistical calculations [Hahn 1987] for densities of ρ/ρ_0=0.05 and 0.9, respectively, where ρ_0 denotes the density of normal nuclear matter. The dotted curves show the result of different calculations [Fiel 1987] in which the primary isotopic distributions were parametrized by a simple analytical function of the ground state masses and Coulomb barriers of the emitted nuclei. The shaded horizontal bands indicate the population ratios which are consistent with our measurements for the reaction $^{16}O + ^{197}Au$ at E/A=94 MeV. Because of the small value of $\Delta E/T$, the predicted feeding of particle unbound states in ^{6}Li could be sufficient to make the extraction of an upper bound for the true emission temperature highly uncertain. The calculations also indicate significant perturbations of the relative populations of states for the widely separated states in ^{4}He and ^{8}Be nuclei. Furthermore, the predicted perturbations are very sensitive to the detailed assumptions on the primary nuclide distributions [Fiel 1987]. Based upon these calculations, the measured populations of states in ^{4}He nuclei cannot provide reliable upper bounds for the true emission temperatures; the uncertainties are somewhat smaller, but still appreciable for the measured populations of states in ^{8}Be. The relative populations of states in ^{5}Li, on the other hand, are predicted to be relatively unperturbed over the temperature range of interest.

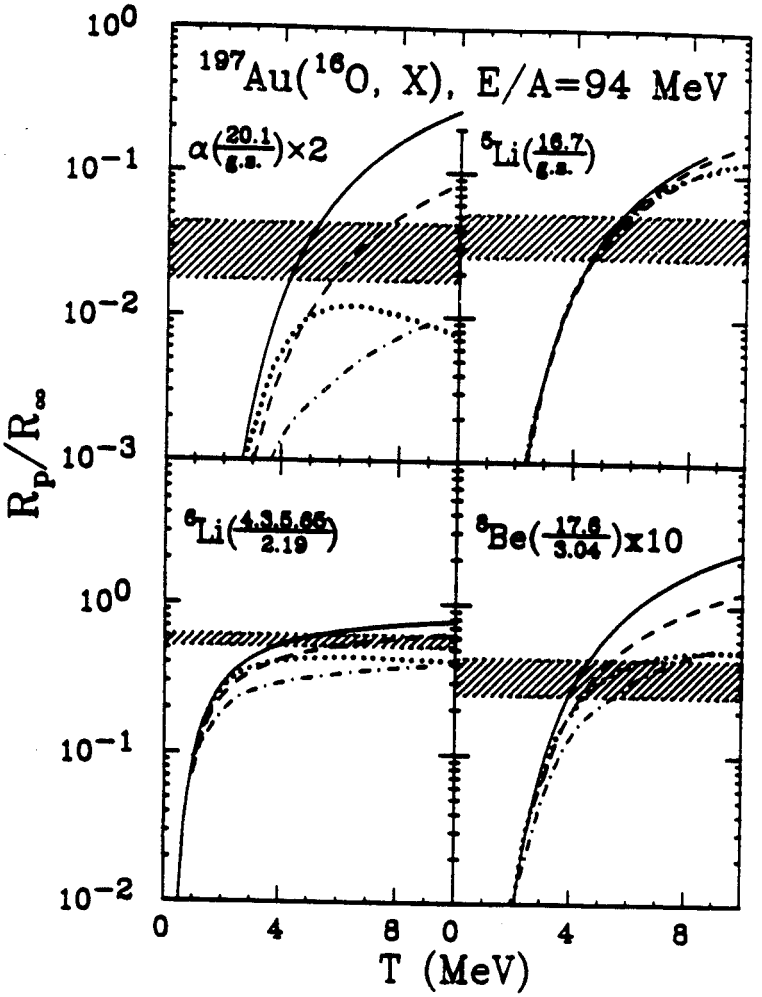

Figure IX.1 Temperature dependence of population ratios for specific states in ^{4}He, ^{5}Li, ^{6}Li, and ^{8}Be. Ratios measured in this experiment are indicated by the shaded bands. The solid curves show the temperature dependence of the primary population ratio; the dashed and dotted-dashed curves show the final ratios predicted by the quantum statistical calculations of [Hahn 1987] assuming densities of ρ/ρ_0=0.05 and 0.9, respectively, where ρ_0 denotes normal nuclear matter density. The dotted curves are final population ratios calculated by assuming a simple analytical dependence of the primary populations on binding energies and Coulomb barriers [Fiel 1987].

In order to overcome some of the limitations of previous feeding calculations, we have extended the scope of such calculations. In comparison with previous work, our calculations are not restricted to feeding from tabulated states of fragments with $Z \leq 10$, but also include feeding from high lying continuum states for an extended range of primary fragments, $Z \leq 20$. In order to reduce previous ambiguities for the primary fragment distributions, the calculations are constrained by element distributions measured [Troc 1986] for the ^{16}O+Au reaction at E/A=84 MeV. (The use of these data, obtained from a slightly different reaction, is justified since the final element distributions exhibit only slight dependences on entrance channel and incident energy [Troc 1986].) The calculations indicate that feeding from high lying continuum states has only minor effects on the emission temperatures extracted from relative populations of the states in ^{4}He, ^{5}Li, and ^{8}Be nuclei measured for the reaction ^{16}O + ^{197}Au at E/A=94 MeV.

Details of our calculations are presented in Section 9.1. The calculated effects of feeding on the relative populations of states are discussed in Section 9.2.

9.1 MODEL ASSUMPTIONS

In our calculation, the initial fragment distribution is assumed to be given by:

$$dP(N,Z,J,E^*)/dE^* = \frac{P(Z) \cdot P_Z(A) \cdot (2J+1) \cdot \rho(E^*,J) \cdot \exp(-E^*/T)}{\sum_J \int dE^* \, (2J+1) \cdot \rho(E^*,J) \cdot \exp(-E^*/T)} , \quad (IX.1)$$

where P(Z) denotes the primary element distribution, $P_Z(A)$ is the isotopic distribution for a given element, and $\rho(E^*,J)$ is the level-density at excitation energy E^* and angular momentum J. For the sake of clarity we have assumed that the populations of states of all primary fragments can be described by a single emission temperature T. This assumption is useful for the discussion of systematic errors due to feeding from higher lying particle unbound states. By construction, such an approach is schematic. Because of the expected effects of expansion and cooling of the reaction zone [Lenk 1986, Schl 1987, Frie 1988], realistic fragment distributions will include fragments emitted over a range of temperatures. Present theoretical uncertainties are sufficiently large to make the investigation of more complicated distributions less instructive. Nevertheless, such investigations must be performed when specific models are compared to experimental data.

Details of the fragment formation process are still unclear. The primary fragment distributions, $P(Z)\cdot P_Z(A)$, can be expected to depend on Coulomb barrier penetrabilities, the charge-to-mass ratio of the reaction zone, binding energies, as well as on details of the reaction dynamics such as an expansion of the reaction zone or a development of mechanical instabilities followed by a rapid growth of density fluctuations. Rather than calculating the primary fragment distributions from a specific model, we have adjusted the primary element distribution, P(Z), at each temperature to make the final element distribution (which includes the products from the decay of particle unstable states) consistent with the data of ref. [Troc 1986] and Chapter V, (see also Sect. 9.2). While this approach explores the uncertainties of emission temperatures extracted from the reaction ^{16}O +

^{197}Au at E/A=94 MeV, it does not make general predictions about the temperature dependence of relative populations of states. Such predictions cannot be obtained in a model-independent way since they require the knowledge of the temperature dependence of the primary fragment distributions.

Because of lacking experimental information, the isotopic distributions were parametrized as in ref. [Fiel 1987]:

$$P_Z(A) \propto \exp\{ -V_C/T + Q/T \} , \qquad (IX.2)$$

where V_C is the Coulomb barrier for emission from a parent nucleus of mass and atomic numbers A_0 and Z_0, and Q is the ground state Q-value:

$$V_C = Z(Z_0-Z)e^2/[r_o[A^{1/3} + (A_0-A)^{1/3}]] \qquad (IX.3)$$

and

$$Q = [B(A_0-A,Z_0-Z) + B(A,Z)] - B(A_0,Z_0) . \qquad (IX.4)$$

We used the parameters r_o=1.2 fm, A_0=213 and Z_0=87. The binding energies, $B(A_0,Z_0)$ and $B(A_0-A,Z_0-Z)$, of heavy nuclei were calculated from the Weizsäcker mass formula [Marm 1969].

$$B(A,Z) = C_0A - C_1A^{2/3} - C_2Z^2/A^{1/3} - C_3(A-2Z)^2/A , \qquad (IX.5)$$

with C_0=14.1 MeV, C_1=13.0 MeV, C_2=0.595 MeV, and C_3=19.0 MeV. For the emitted light fragments, we used the measured binding energies, B(A,Z), of the respective ground states [Waps 1985]. Distributions similar to Eqs. IX.2-IX.4 can result from the sequential decay of highly excited

compound nuclei [Frie 1983]. Slightly different assumptions about the isotopic distributions are not expected to significantly alter our conclusions.

For nuclei of charge $Z \leq 11$, the level density included known [Ajze 1983, Ajze 1984, Ajze 1985, Ajze 1986a, Ajze 1986b, Endt 1978] states up to an excitation energy ε_0:

$$\rho(E^*,J) = \sum_i \delta(E_i - E^*) \text{ , for } E^* \leq \varepsilon_0 \text{ .} \qquad \text{(IX.6)}$$

At higher excitation energies, $\varepsilon_0 < E^* < E^*_{max}$, where individual states are not known in sufficient detail, a continuum approximation [Gilb 1965] was used:

$$\rho(E^*,J) = \frac{(2J+1)\ \exp\left[2\sqrt{a(E^*-E_0)}\right]}{24\ \sqrt{2}\ a^{1/4}\ \sigma^3\ (E^*-E_0)^{5/4}} \cdot \exp\left[-(J+1/2)^2/2\sigma^2\right],$$

$$\text{for } \varepsilon_0 < E^* < E^*_{max}. \qquad \text{(IX.7)}$$

Here, a is the level density parameter, chosen as $a = A/8\ \text{MeV}^{-1}$, $E^*_{max} = \varepsilon^*_{max} \cdot A$ is a cutoff parameter for the excitation energy, and σ is the spin cutoff parameter taken from ref. [Gilb 1965] as:

$$\sigma^2 = 0.0888\ \left[a(E^*-E_0)\right]^{1/2}\ A^{2/3} \text{ .} \qquad \text{(IX.8)}$$

For each isotope, the matching energy ε_0 was chosen as the location of the maximum of the density $\eta(E) = \Delta N(E)/\Delta E$, where $\Delta N(E)$ denotes the number of tabulated levels in the energy interval $E-\Delta E/2$, ..., $E+\Delta E/2$.

For illustration, the histogram in Figure IX.2 shows the known level density of ^{20}Ne states. At the energy ε_0=13 MeV, the density $\eta(E)$ has a maximum clearly because of decreasing experimental information about individual states at higher excitation energies. The energy E_0 was then determined by the normalization condition:

$$\int_{E_0}^{\varepsilon_0} dE^* \int dJ \left\{ \frac{(2J+1)\,\exp\left[2\sqrt{a(E^*-E_0)}\right]}{24\sqrt{2}\,a^{1/4}\,\sigma^3\,(E^*-E_0)^{5/4}} \exp\left[-(J+1/2)^2/2\sigma^2\right] \right\}$$

$$= \int_0^{\varepsilon_0} dE^* \left\{ \sum_i \delta(E_i-E^*) \right\} . \qquad \text{(IX.9)}$$

For nuclei of charge $12 \leq Z \leq 20$, a continuum approximation to the level density was used over the entire range of excitation energies. At low excitation energies, $E^* \leq \varepsilon_0$, we modified the empirical interpolation formula of Ref. [Gilb 1965] to include a spin dependence:

$$\rho(E^*,J) = \frac{1}{T} \exp\left[(E-E_1)/T\right] \frac{(2J+1)\,\exp\left[-(J+1/2)^2/2\sigma^2\right]}{\sum(2J+1)\,\exp\left[-(J+1/2)^2/2\sigma^2\right]} ,$$

$$\text{for } E^* \leq \varepsilon_0 , \qquad \text{(IX.10)}$$

where the spin cutoff parameter was calculated from Eq. (IX.8) at the energy $E^*=\varepsilon_0$; ε_0, T, and E_1 were taken from ref. [Gilb 1965]; σ was assumed to be constant for $E^* \leq \varepsilon_0$. At higher excitation energies, the level density was assumed to have the functional form of Eq. (IX.7), with a=A/8 and E_0 determined by requiring the level density to be continuous at $E^*=\varepsilon_0$.

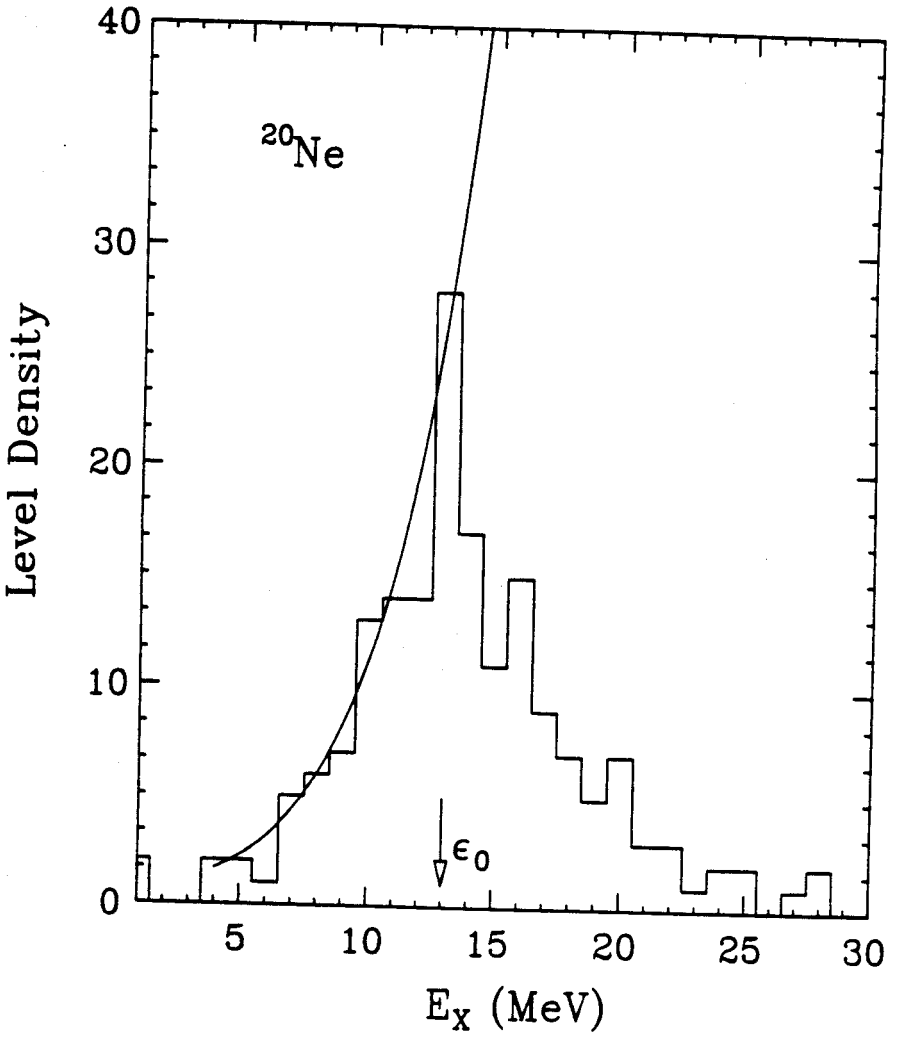

Figure IX.2 The level density as a function of excitation energy. The histogram shows the number of known levels for ^{20}Ne binned in excitation energy. The curves is the level density calculation with Eq. IX.7.

The continuum approximation for the level density, Eq. (IX.7), may be unrealistic at high excitation energies. In order to study the incremental effects of feeding from high lying continuum states, we have truncated the level density above a certain excitation energy per nucleon, $\epsilon^*_{max}=E^*_{max}/A$, and investigated the results for different truncations. Because of life-time arguments [Frie 1983, Fai 1983], some truncation of fragment excitation energies should be physically reasonable. Extrapolating from the systematics of level widths given in ref. [Stok 1977], the mean lifetime of states at E*/A=10 MeV is estimated to be of the order of $\tau \approx 2\times10^{-22}$ s. This time is comparable to the time the fragments need to separate from the emitting source. Much shorter lifetimes should be physically unreasonable since the corresponding states would decay before the fragments left the emitting source. Nevertheless, we will also explore extreme and, most likely, less realistic assumptions about the primary populations of states to assess the possible range of temperatures which could be consistent with the measurements for the reaction $^{16}O + {}^{197}Au$ at E/A=94 MeV.

The decay of particle unstable states was calculated from the Hauser-Feshbach formula [Haus 1952] for which the branching ratios are expressed as:

$$\Gamma_c \propto \sum_{S=|j-s|}^{|j+s|} \sum_{\ell=|J-S|}^{|J+S|} T_\ell(E) \ . \qquad \text{(IX.11)}$$

Here, j is the spin of the daughter nucleus, S is the channel spin, ℓ is the orbital angular momentum of the emitted particle, and $T_\ell(E)$ is the transmission coefficient for the ℓ-th partial wave. For decays from

continuum states, the transmission coefficients were approximated by the sharp cutoff approximation,

$$T_\ell(E) = \begin{cases} 1 , & \text{for } \ell \leq \ell_0 \\ 0 , & \text{for } \ell > \ell_0 \end{cases} , \qquad \text{(IX.12)}$$

with

$$\ell_0 = (2\pi/h)\, r_0 \{(A-A_c)^{1/3} + A_c^{1/3}\} \sqrt{2\mu(E-V_c)} . \qquad \text{(IX.13)}$$

Here, μ denotes the reduced mass. For decays from discrete states, the transmission coefficients were parametrized as [Gomez]:

$$T_\ell(E) = \{1 + \exp[\frac{V_{\ell,Z} - E}{\delta\, V_{\ell,Z}}]\}^{-1} , \qquad \text{(IX.14)}$$

with

$$V_{\ell,Z} = \frac{e^2\, Z_c(Z - Z_c)}{r_Z[(A-A_c)^{1/3} + A_c^{1/3}]} + \frac{(h/2\pi)^2\, \ell(\ell+1)}{2\mu r_Z^2[(A-A_c)^{1/3} + A_c^{1/3}]^2} , \qquad \text{(IX.15)}$$

and

$$\delta = \begin{cases} \delta_1 , & \text{for } E > V_{\ell,Z} \\ \delta_2 , & \text{for } E < V_{\ell,Z} \end{cases} . \qquad \text{(IX.16)}$$

The parameters r_Z, δ_1, and δ_2 are listed in Table 11.

To keep the numerical calculations tractable, we restricted the calculations by only including decays via emission of the ground states of fragments with $Z \leq 5$ and those resonances which are of direct relevance for the present investigation. Specifically, we included the emission of: n, (2n), p, (2p), d, t, ^{3}He, ^{4}He(g.s., 20.1 MeV), ^{5}Li(g.s., 16.7 MeV), ^{6}Li(g.s., 2.19 MeV, 4.3 MeV, 5.65 MeV), ^{7}Li(g.s.), ^{7}Be(g.s.), ^{8}Be(g.s., 3.04 MeV, 17.6 MeV), ^{9}Be(g.s.), ^{10}B(g.s.).

9.3 RESULTS FOR SEQUENTIAL FEEDING

In our discussion of the distortions of the relative populations of particle unbound states due to sequential feeding, we focus on the relative populations of $^4He_{g.s.}(J^\pi = 0^+)$ vs. $^4He_{20.1}(J^\pi = 0^+)$, $^5Li_{g.s.}(J^\pi = \frac{3}{2}^-)$ vs. $^5Li_{16.7}(J^\pi = \frac{3}{2}^+)$, and $^8Be_{3.04}(J^\pi = 2^+)$ vs. $^8Be_{17.6}(J^\pi = 1^+)$. In order to assess the uncertainties due to sequential feeding we have extended the scope of previous calculations, by including decays from heavier nuclei (up to $Z \leq 20$) and from higher lying continuum states. Uncertainties for the primary fragment distributions were reduced by constraining the calculations with measured element distributions [Troc 1986], see Fig. IX.3 for illustration. In this figure, primary element distributions, integrated over all states populated, are shown by histograms and particle stable primary fragments are represented by shaded areas. The distributions of fragments after the decay of particle unstable states are shown by open points. The data of [Troc 1986] are shown by solid points (the relative yields of helium and lithium nuclei were taken from Chapter V by integrating the cross sections for these elements). At moderate temperatures, $T \leq 5$ MeV, one can always construct fragment distributions which are consistent with measured fragment yields, see Fig. IX.3a. At higher temperatures, one can still obtain reasonable agreement for moderate cut-off parameters, $\epsilon^*_{max} \leq 10$ MeV, see the example given in Fig. IX.3d. For more extreme (and probably unrealistic) cases, when the primary distributions are characterized both by high temperatures ($T > 10$ MeV) and by high values of the truncation parameter ($\epsilon^*_{max} = 15$ MeV), practically all heavier primary fragments decay into significantly lighter final fragments, causing a depletion of yields at larger Z, see Figure IX.3b and IX.3c. Better

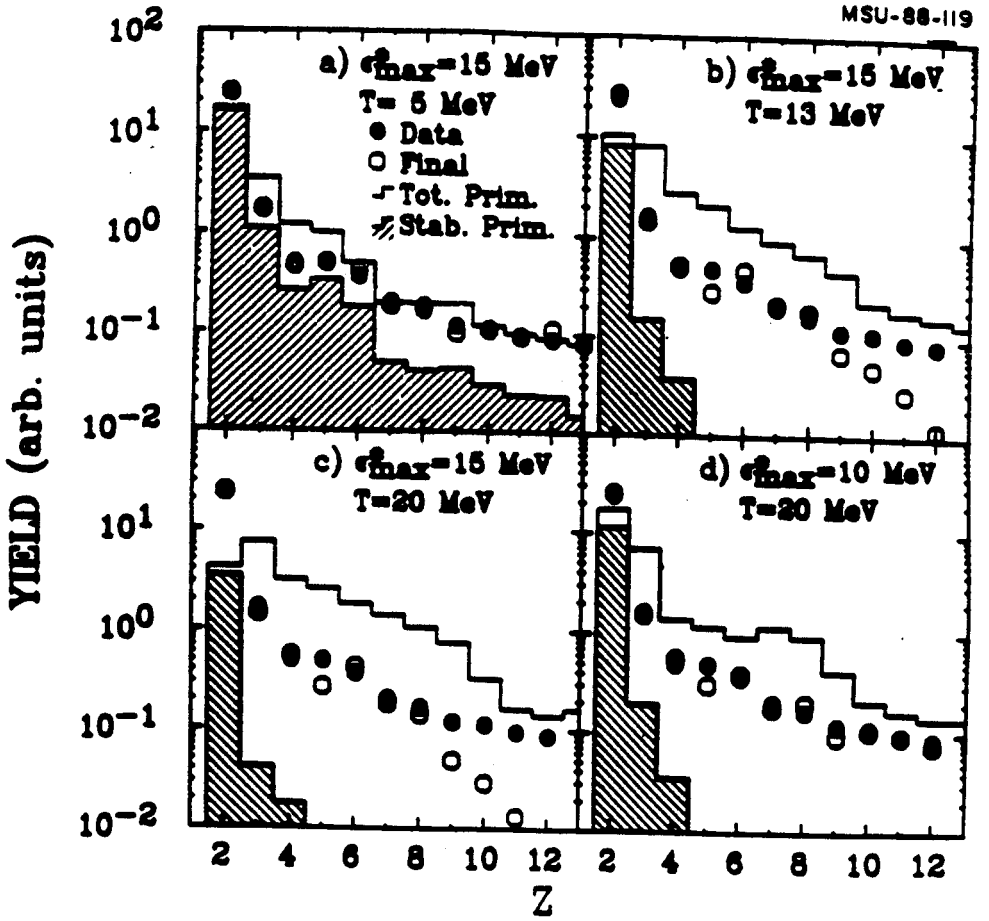

Figure IX.3 Element distributions used for: (a) T=5 MeV, ϵ^*_{max}=15 MeV; (b) T=13 MeV, ϵ^*_{max}=15 MeV; (c) T=20 MeV, ϵ^*_{max}=15 MeV; (d) T=20 MeV, ϵ^*_{max}=10 MeV. The shaded area shows the primary distribution of particle stable fragments, the histogram shows the distribution of primary fragments, integrated over all states populated, and the open points show the final distribution of particle stable fragments after the decay of particle unstable states. Solid points show the data of ref. [Troc 1986].

agreement with measured fragment distributions might be obtained by including heavier fragments (Z>20) in the primary distribution. However, we have refrained from extending the range of primary fragments because of the large amounts of computer time involved. We will show below that the incomplete knowledge of the fragment distribution at high T and ε^*_{max} does not affect our conclusion.

Figures IX.4-IX.6 show the temperature dependence of the calculated fractions, Y_{feed}/Y_{tot}, for $^4He_{g.s.}$, $^5Li_{g.s.}$, and $^8Be_{g.s.}$ nuclei produced in the decay of particle unstable primary reaction products. Here, Y_{feed} denotes the yield due to feeding from higher lying particle unbound states and Y_{tot} denotes the total fragment yield, i.e. the sum of the primary yield and Y_{feed}. Different symbols show the results for different choices of the cut-off parameter, ε^*_{max}. The diamond shaped points show the results for the decay of known discrete states for nuclei of charge $Z \leq 10$; these decays were considered in Refs. [Hahn 1987, Fiel 1987] using different primary distributions. In most cases, feeding is calculated to be important at high temperatures. The magnitude of feeding increases with ε^*_{max}. For temperatures above about 10 MeV, the calculated ^{5}Li yields are dominated by feeding from highly excited primary reaction products unless the primary population of states is truncated at a relatively low excitation energy ($\varepsilon^*_{max} \leq 5$ MeV), see Figure IX.5. For ^{4}He and ^{8}Be nuclei, feeding is calculated to be important already at significantly lower temperatures, see Figure IX.4 and IX.6. (For ^{4}He, the increase of Y_{feed}/Y_{tot} at very low temperatures may be an artifact of our constraint on the fragment yields which produces a relatively large number of ^{8}Be fragments decaying into two ^{4}He nuclei.)

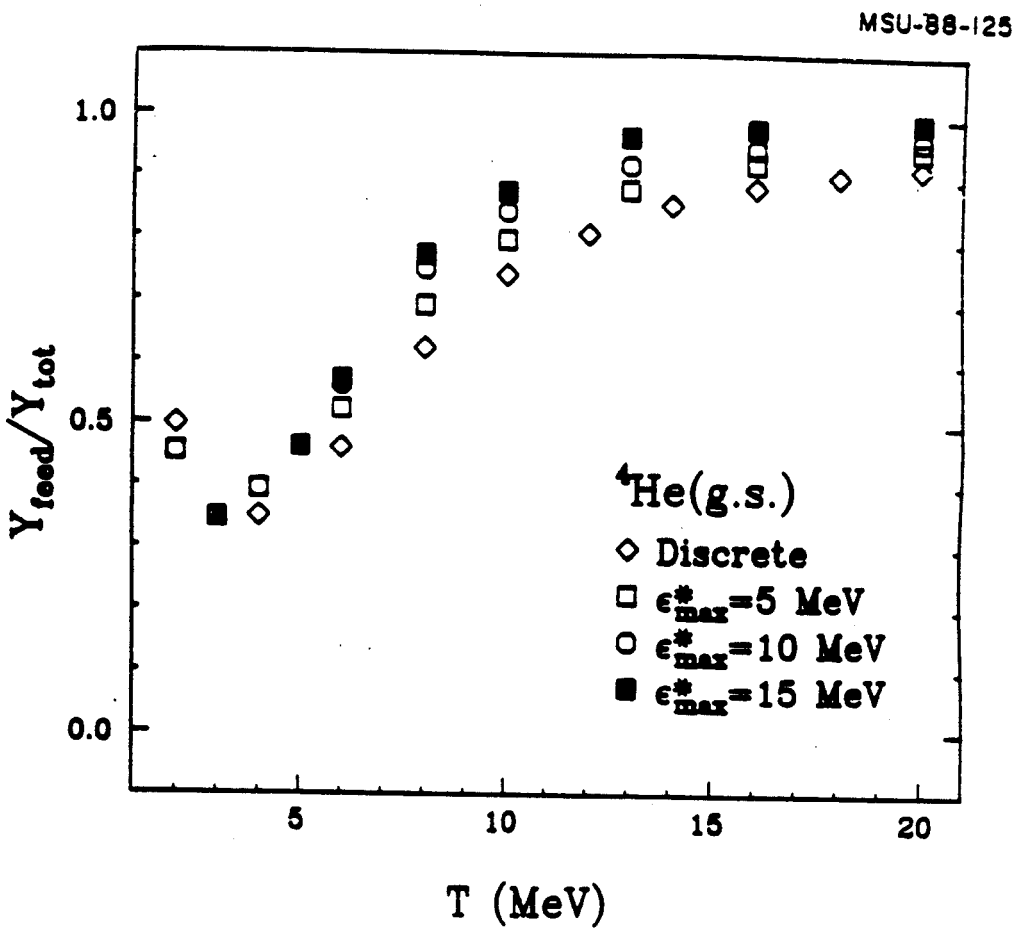

Figure IX.4 Temperature dependence of the calculated fraction, Y_{feed}/Y_{tot}, for $^4He_{g.s.}$ nuclei produced in the sequential decay of particle unstable primary fragments. Different symbols show the results for different cut-off parameters, ϵ^*_{max}. The diamond shaped points show the results of calculations in which only tabulated states of fragments with charge Z≤10 were populated initially.

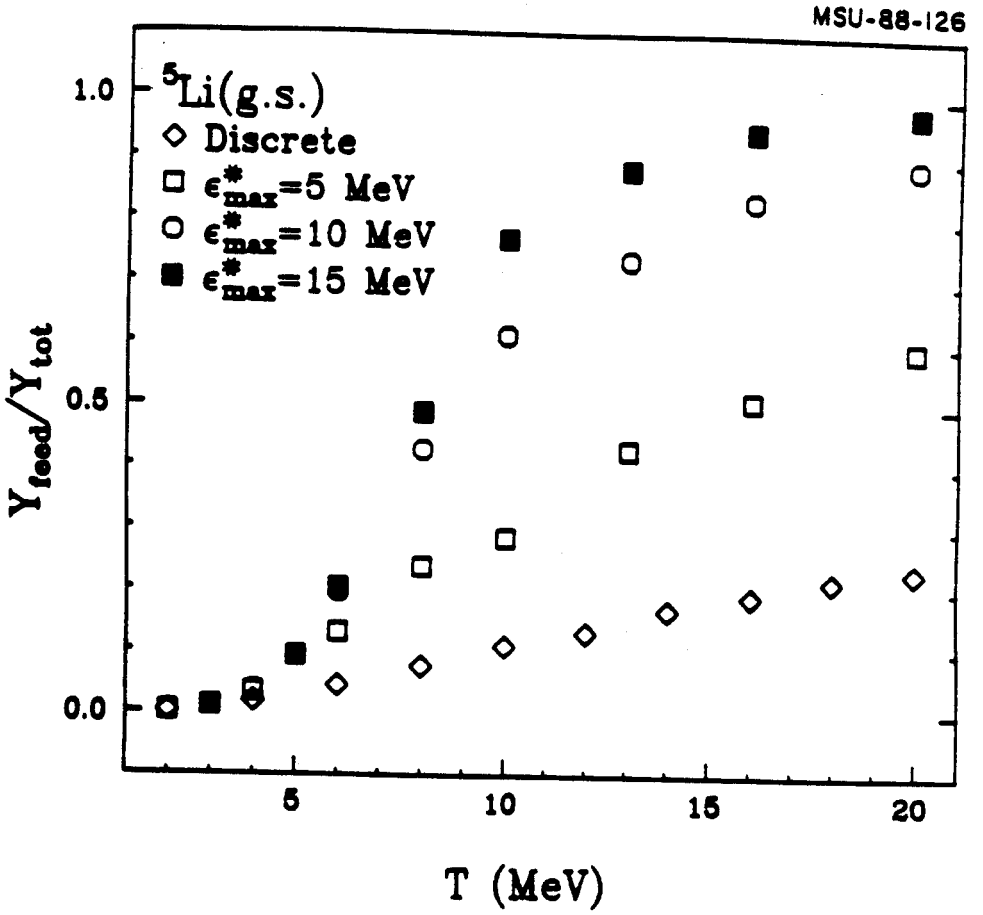

Figure IX.5 Temperature dependence of the calculated fraction, Y_{feed}/Y_{tot}, for $^5Li_{g.s.}$ nuclei produced in the sequential decay of particle unstable primary fragments. Different symbols show the results for different cut-off parameters, ϵ^*_{max}. The diamond shaped symbols show the results of calculations in which only known states of fragments with charge $Z \leq 10$ were populated initially.

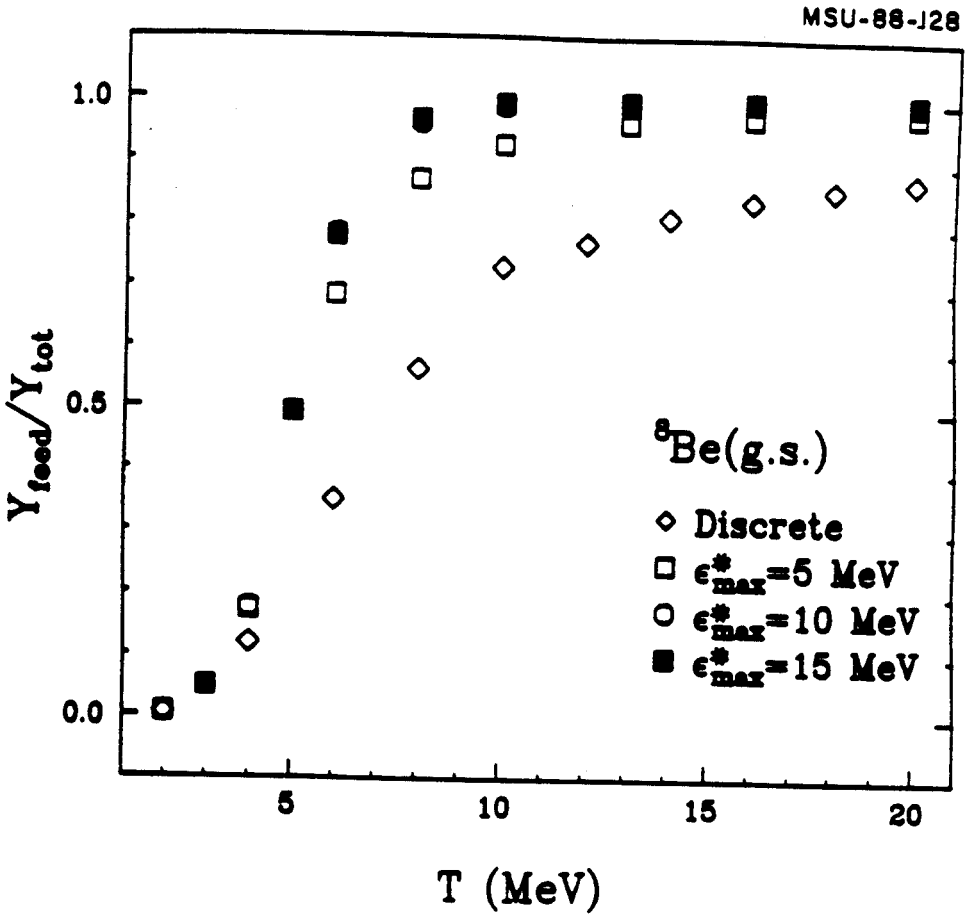

Figure IX.6 Temperature dependence of the calculated fraction, Y_{feed}/Y_{tot}, for $^8Be_{g.s.}$ nuclei produced in the sequential decay of particle unstable primary fragments. Different symbols show the results for different cut-off parameters, ϵ^*_{max}. The diamond shaped symbols show the results of calculations in which only known states of fragments with charge $Z \leq 10$ were populated initially.

Since the quantitative amount of feeding depends on the magnitude of the cut-off parameter, ϵ^*_{max}, the amount of feeding must depend on the populations of states at high excitation energies where the density of states is not well known. The resulting uncertainties for the extracted emission temperatures can be addressed by investigating the sensitivity of the calculated relative populations of states to the parameter, ϵ^*_{max}.

Figures IX.7-IX.9 show the relative yields of the states in ^{4}He, ^{5}Li, and ^{8}Be nuclei emitted in sequential decay chains originating from primary fragments of charge Z. For each figure, the three panels show calculations for T=6, 13, and 20 MeV, using the cut-off parameter ϵ^*_{max}=10 MeV. The yields are normalized with respect to the primary yields of ^{4}He, ^{5}Li, and ^{8}Be, respectively, emitted in their ground states. These primary ground state yields were set to unity in the figures. In Figures IX.7, IX.8, and IX.9, the primary populations of states in ^{4}He, ^{5}Li, and ^{8}Be are included in the yields plotted for Z=2, 3, and 4, respectively. All states are calculated to be fed via sequential decays. Moreover, feeding is not limited to the decay of light primary fragments but is calculated to occur from the entire range of primary elements. Based upon these results, the truncation of the primary fragment distribution at $Z \leq 10$ [Hahn 1986, Fiel 1987], or even at $Z \leq 20$, cannot be trivially justified. For high initial temperatures, $T \geq 10$ MeV, the measurable relative populations of states (and, therefore, the extracted emission temperatures) depend both on the absolute and relative amounts of feeding to the two states under consideration. When most final fragments are produced by sequential decays of highly excited primary fragments, the relative amount of feeding becomes more important for the extraction of emission temperatures than the absolute amount. It

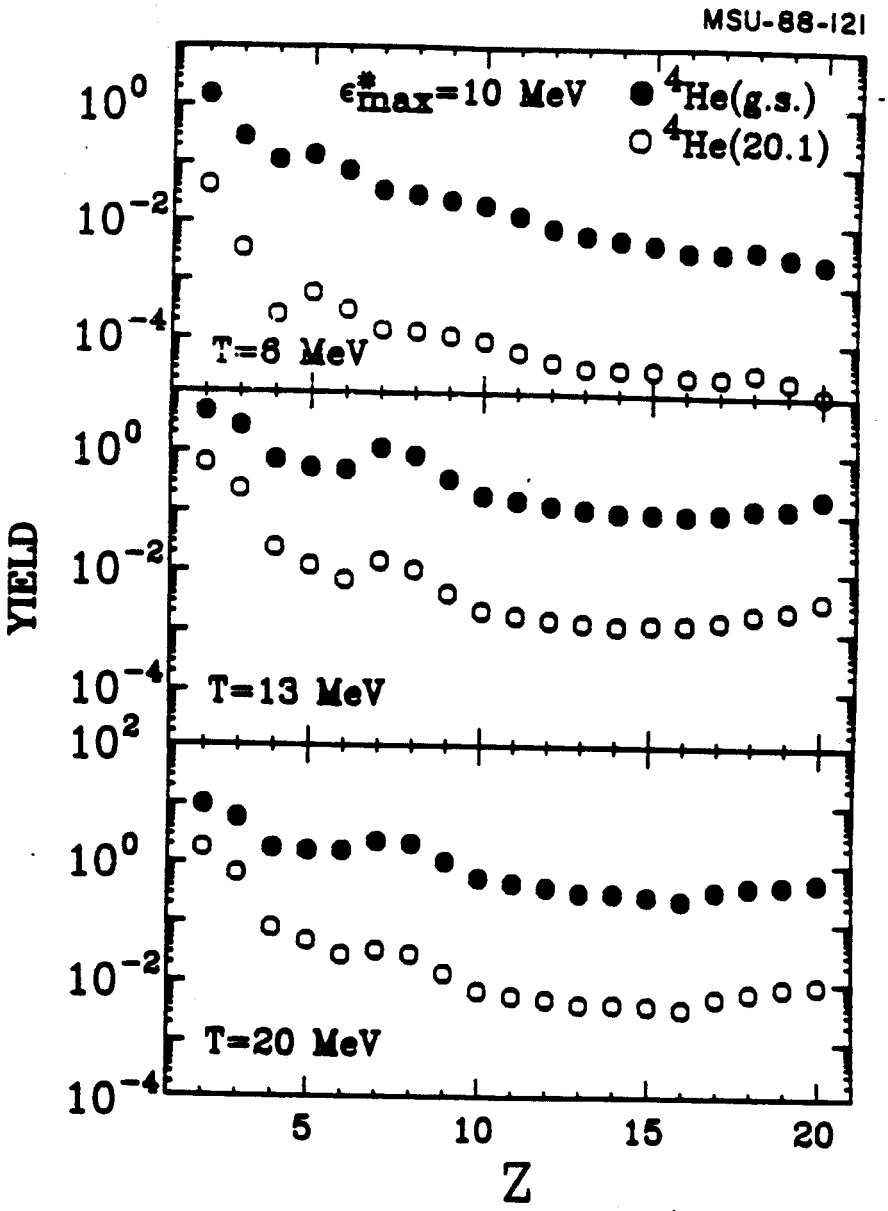

Figure IX.7 Relative yields of $^4He_{g.s.}$ and $^4He_{20.1}$ nuclei emitted in decay chains originating from primary fragments of charge Z, calculated for the parameters T=6 MeV (upper panel), T=13 MeV (center panel), and T=20 MeV (lower panel). The cut-off parameter of ϵ^*_{max}=10 MeV was used.

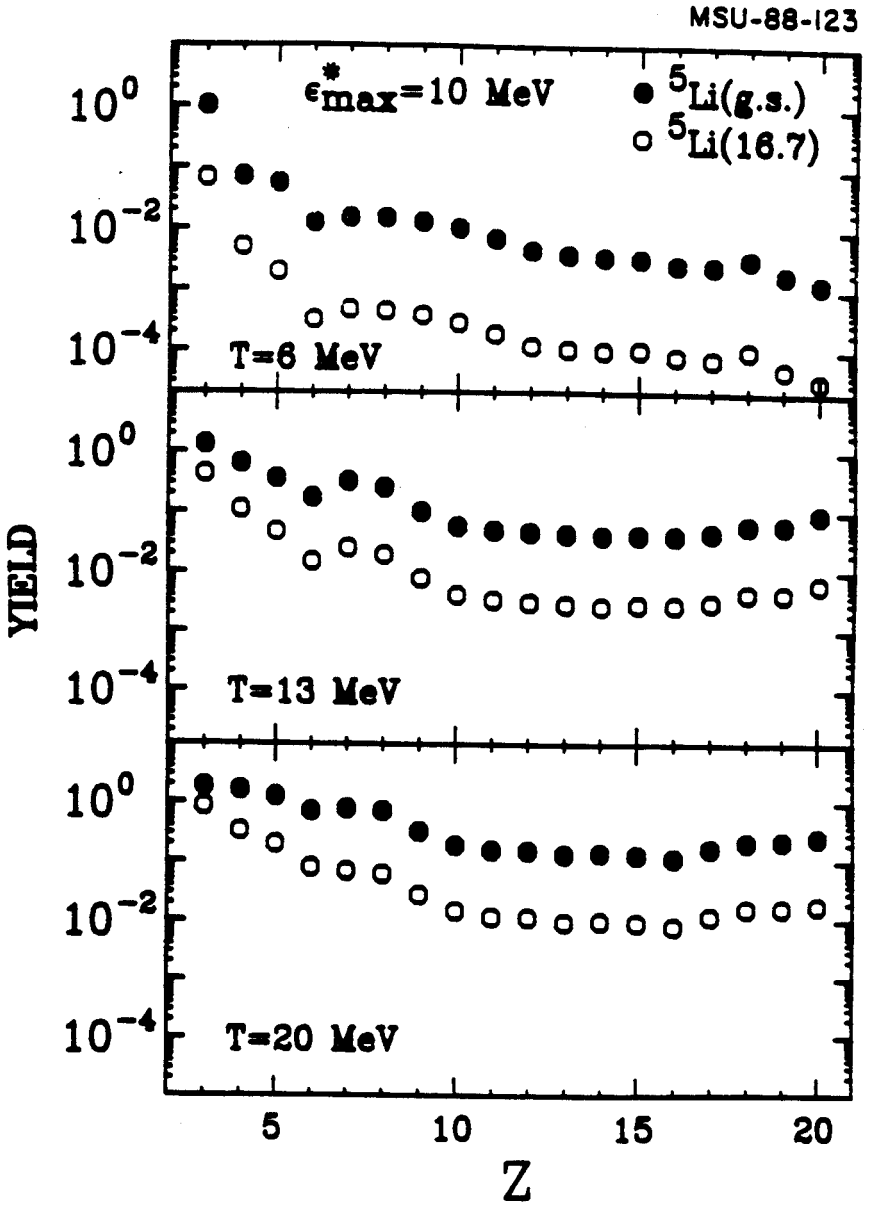

Figure IX.8 Relative yields of $^5Li_{g.s.}$ and $^5Li_{16.7}$ nuclei emitted in decay chains originating from primary fragments of charge Z, calculated for the parameters T=6 MeV (upper panel), T=13 MeV (center panel), and T=20 MeV (lower panel). The cut-off parameter of ϵ^*_{max}=10 MeV was used.

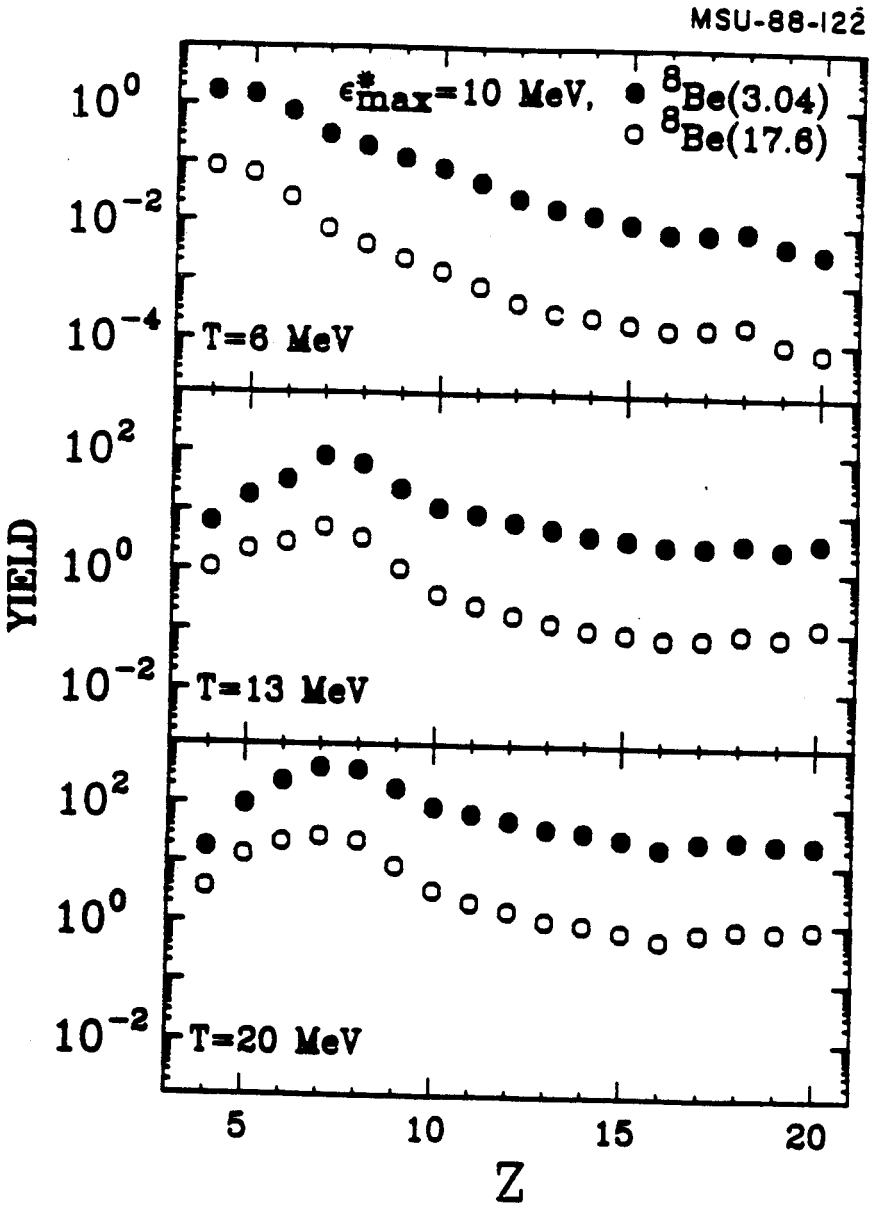

Figure IX.9 Relative yields of $^8Be_{3.04}$ and $^8Be_{17.6}$ nuclei emitted in decay chains originating from primary fragments of charge Z, calculated for the parameters T=6 MeV (upper panel), T=13 MeV (center panel), and T=20 MeV (lower panel). The cut-off parameter of ϵ^*_{max}=10 MeV was used.

is important to note that the relative amount of feeding from heavier fragments does not exhibit a strong dependence upon the charge of the primary fragment.

Figures IX.10-IX.12 show the "feeding ratios", $R_Z = Y_{Z,2}/Y_{Z,1}$, of the yields of two states, 1 and 2, produced in decay chains originating from primary fragments of charge Z. The three panels in the figures show calculations for three different temperatures, T=6, 13, and 20 MeV. The dashed and solid histograms show calculations with different choices for the cut-off parameter, ϵ^*_{max}= 10 and 15 MeV. The right hand scales express these feeding ratios in terms of an "effective feeding temperature" defined by:

$$R_Z = Y_{Z,2}/Y_{Z,1} = R_\infty \exp\left(-\Delta E/T_{eff}(Z) \right) , \qquad \text{(IX-17)}$$

where $R_\infty=(2J_2+1)/(2J_1+1)$ is the high temperature limit of the primary population ratio of two states of spins J_1 and J_2 and excitation energies E^*_1 and E^*_2, with $\Delta E=E^*_2-E^*_1$. This effective feeding temperature corresponds to the emission temperature that would be extracted experimentally if the states in ^{4}He, ^{5}Li, and ^{8}Be were produced entirely by decays of primary fragments of charge Z. The primary populations of the states in ^{4}He, ^{5}Li, and ^{8}Be are included in the definition of $R_{Z=2}$ in Figure IX.10, $R_{Z=3}$ in Figure IX.11, and $R_{Z=4}$ in Figure IX.12, respectively.

The decays of heavier, highly excited primary fragments produce relative populations of states which, to some extent, reflect the excitation energy distributions of these primary fragments. Because of the multiple chance emissions and the broad distribution of excitation

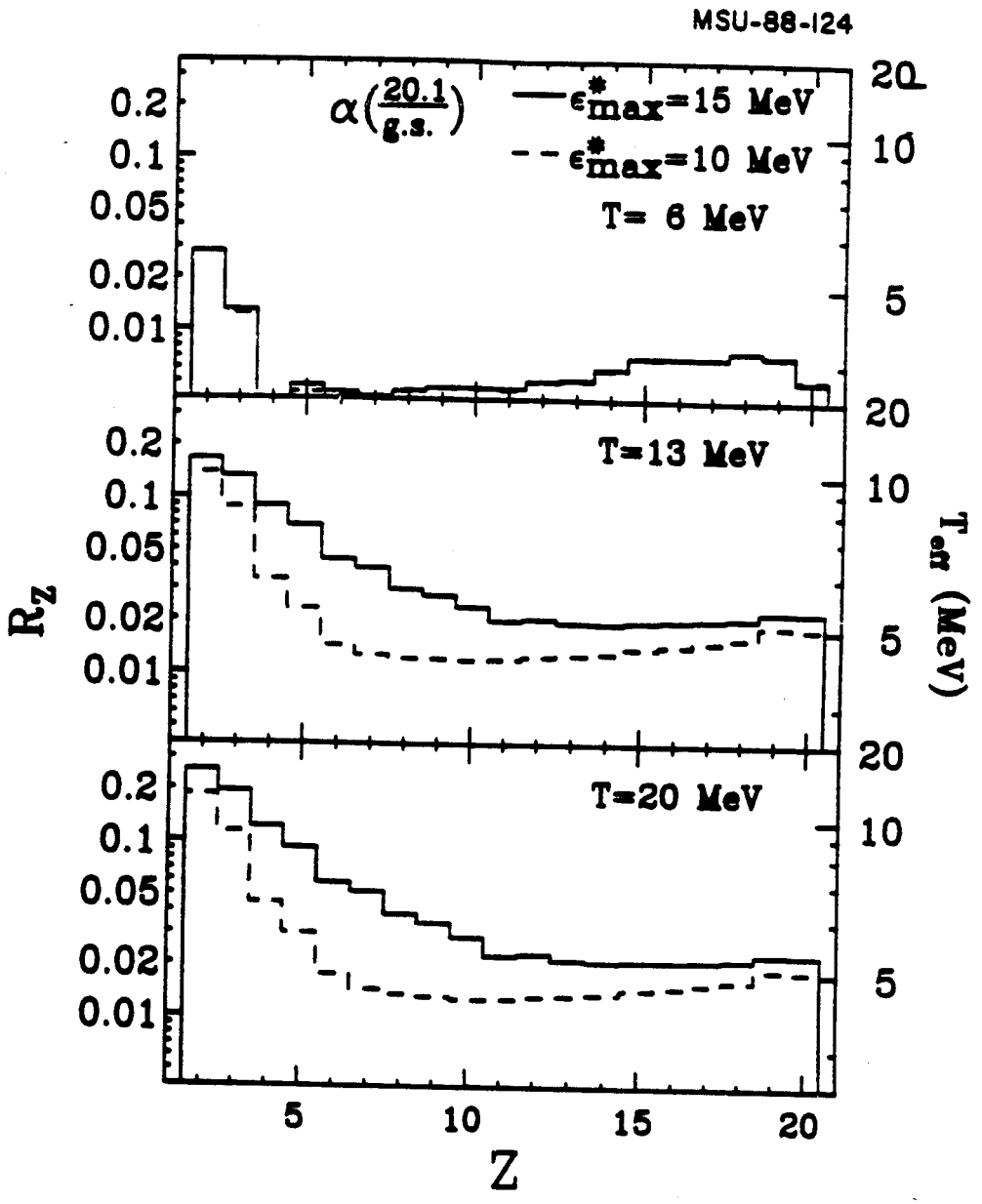

Figure IX.10 "Feeding ratio", R_Z, of $^4He_{g.s.}$ and $^4He_{20.1}$ yields produced by the sequential decay of primary fragments of charge Z. Calculations for T=6, 13, and 20 MeV are shown in the upper, center and lower panels, respectively. The dashed and solid histograms show calculations with ϵ^*_{max}=10 and 15 MeV. The right hand scale expresses these ratios in terms of the "effective feeding temperature" defined in Eq. IX.17.

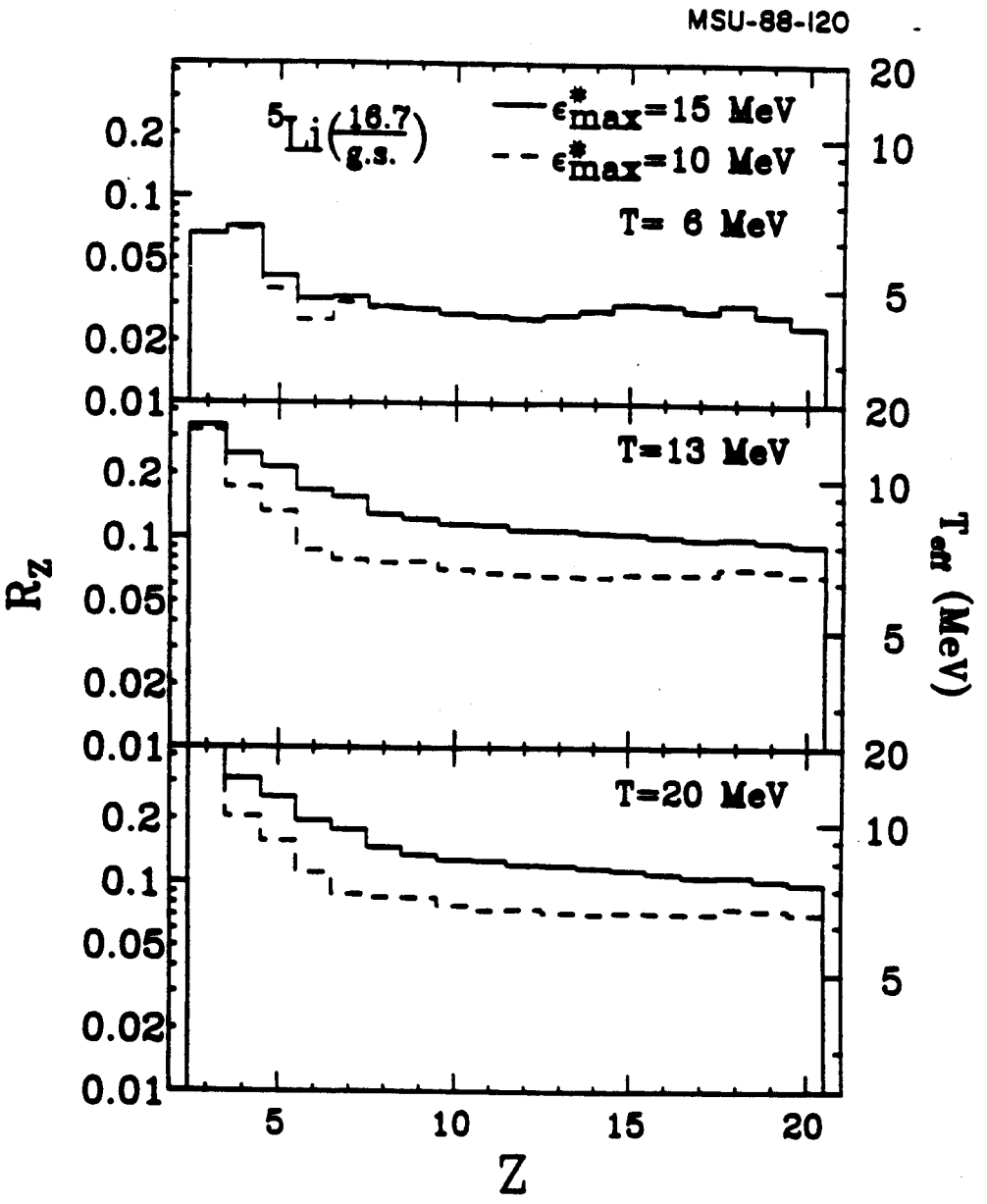

Figure IX.11 "Feeding ratio", R_Z, of $^5Li_{g.s.}$ and $^5Li_{16.7}$ yields produced by the sequential decay of primary fragments of charge Z. Calculations for T=6, 13, and 20 MeV are shown in the upper, center and lower panels, respectively. The dashed and solid histograms show calculations with ϵ^*_{max}=10 and 15 MeV. The right hand scale expresses these ratios in terms of the "effective feeding temperature" defined in Eq. IX.17.

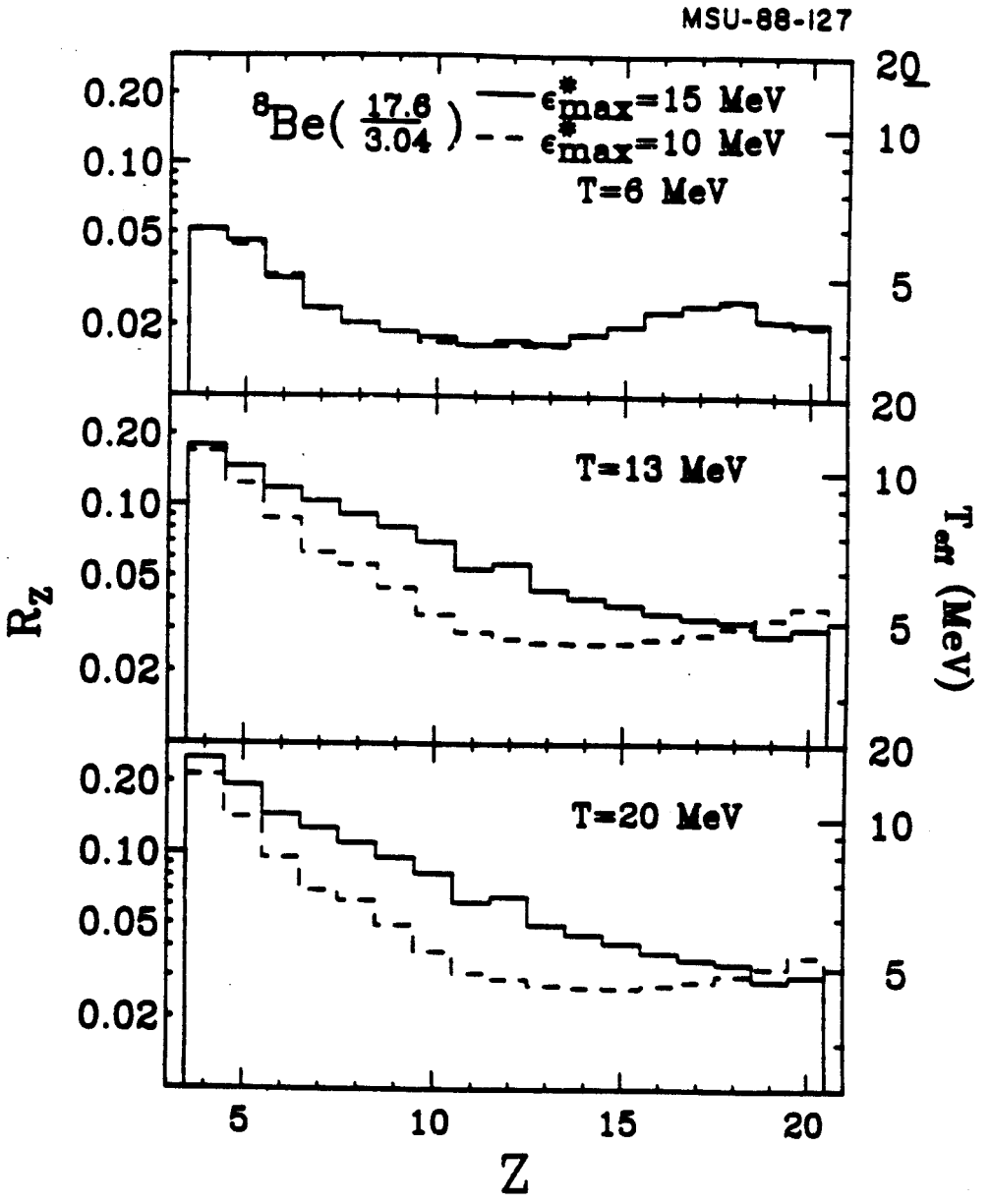

Figure IX.12 "Feeding ratio", R_Z, of $^8Be_{3.04}$ and $^8Be_{17.6}$ yields produced by the sequential decay of primary fragments of charge Z. Calculations for T=6, 13, and 20 MeV are shown in the upper, center and lower panels, respectively. The dashed and solid histograms show calculations with ϵ^*_{max}=10 and 15 MeV. The right hand scale expresses these ratios in terms of the "effective feeding temperature" defined in Eq. IX.17.

energies of the primary fragments, the effective feeding temperatures are smaller than the emission temperature which characterizes the excitation energy distribution of the primary fragments. At high source temperatures, when feeding becomes significant, the effective feeding temperatures for the states in ^{4}He and ^{5}Li do not exhibit a very strong dependence on Z, for Z≥8. For the states in ^{8}Be, the dependence on Z is more pronounced. The effective feeding temperatures increase for larger values of the cut-off parameter ϵ^{*}_{max}, since more highly excited fragments are added to the primary distribution. The effective feeding temperatures also exhibit a slight dependence on the level density parameter (not shown in the figure). For a level density parameter of $a=A/10$ MeV^{-1}, the calculated effective feeding temperatures are slightly higher than those shown in Figures IX.10-IX.12. (For a given excitation energy, a smaller level density parameter raises the temperature of the decaying fragment, according to the relation $T=(E^{*}/a)^{1/2}$.) The perturbations from feeding were calculated to be slightly less for $a=A/10$ MeV^{-1} than for $a=A/8$ MeV^{-1}.

For high emission temperatures, T≥13 MeV, the effective feeding temperatures for the states in ^{4}He and ^{8}Be, extend to lower values than those for the states in ^{5}Li. For large source temperatures and large cut-off parameters, the effective feeding temperatures for the states in ^{5}Li are larger than $T_{eff}(Z)\approx 7.5$ MeV, for all fragments considered. This value is significantly larger than the emission temperature of 5 MeV which characterizes the measured relative populations of states of the emitted ^{5}Li nuclei for the reaction ^{16}O + ^{197}Au at E/A=94 MeV. Additional feeding from heavier fragments (Z>20), feeding from fragment distributions characterized by higher emission temperatures (T≥20 MeV)

and/or from fragments excited to energies higher than ε^*_{max}=15 MeV will not modify the relative populations of states in ^{5}Li by a sufficient amount to make them consistent with these data, independent of remaining uncertainties for the primary element distributions at these extreme values of T and ε^*_{max}. Therefore, one can expect that the low experimental value of T(^{5}Li)≈4.6-5.6 MeV (see Section 7.2) is not caused by long chains of secondary decays from very hot primary fragments even if the range of primary fragment excitation energies or masses exceeded that considered here.

The integrated effects of feeding from the entire distribution of primary fragments are shown in Figure IX.13-IX.15. The figures show the temperature dependence of normalized population ratios, R_p/R_∞, predicted by our calculations. The heavy dotted curves show the population ratios for the primary distributions, $R_p/R_\infty = \exp(-\Delta E/T)$. The dashed-dotted-dotted curves show the effects of feeding from known particle unstable states of mass Z≤10. The dashed-dotted, dashed and solid curves show the calculated modifications which result from the inclusion of continuum states for primary fragments with Z≤20, truncating the level densities at ε^*_{max}= 5, 10, and 15 MeV, respectively.

For the relative populations of the widely separated particle unstable states in ^{5}Li, the calculated feeding from high lying continuum states and heavier nuclei does not introduce significant additional distortions beyond those calculated already for feeding from discrete states. For the states in ^{4}He and ^{8}Be, the sensitivity to ε^*_{max} is more pronounced; yet the measured populations of these states remain inconsistent with temperatures significantly higher than 5 MeV. The insensitivity of the relative populations of the ^{5}Li states to details

of the feeding calculations is astonishing. It is partly due to the constraint imposed upon the final fragment distributions. At low-temperatures and/or low values of ϵ^*_{max}, the absolute amount of feeding is relatively small and constrained by the final fragment distributions. At higher temperatures and larger values of ϵ^*_{max} feeding dominates the fragment yields. The states considered here are then fed with ratios which are larger than the measured values. This effect reduces the uncertainties of the temperatures extracted from the measured ratios.

The shaded horizontal bands in Figure IX.13-IX.15 represent the relative populations of states measured for the $^{16}O+Au$ reaction at E/A=94 MeV. The shaded vertical bands indicate the range of temperatures, T(^{4}He) = 4.2 - 7.0 MeV, T(^{5}Li) = 4.6 - 5.6 MeV, T(^{8}Be) = 3.9 - 4.8 MeV, which are consistent with these measurements and with the present calculations. Close inspection of the figures shows that the upper limit of the extracted emission temperature is established better from the ^{5}Li states than from the states in ^{4}He and ^{8}Be.

TABLE 11

Parameters used for the transmission coefficients defined in Eqs. IX.14-IX.16

Z_c	r_Z(fm)	δ_1	δ_2
0	1.62	0.60	0.10
1	1.62	0.25	0.09
2	1.57	0.07	0.07
3	1.57	0.08	0.06
4	1.55	0.05	0.03
5	1.53	0.04	0.02

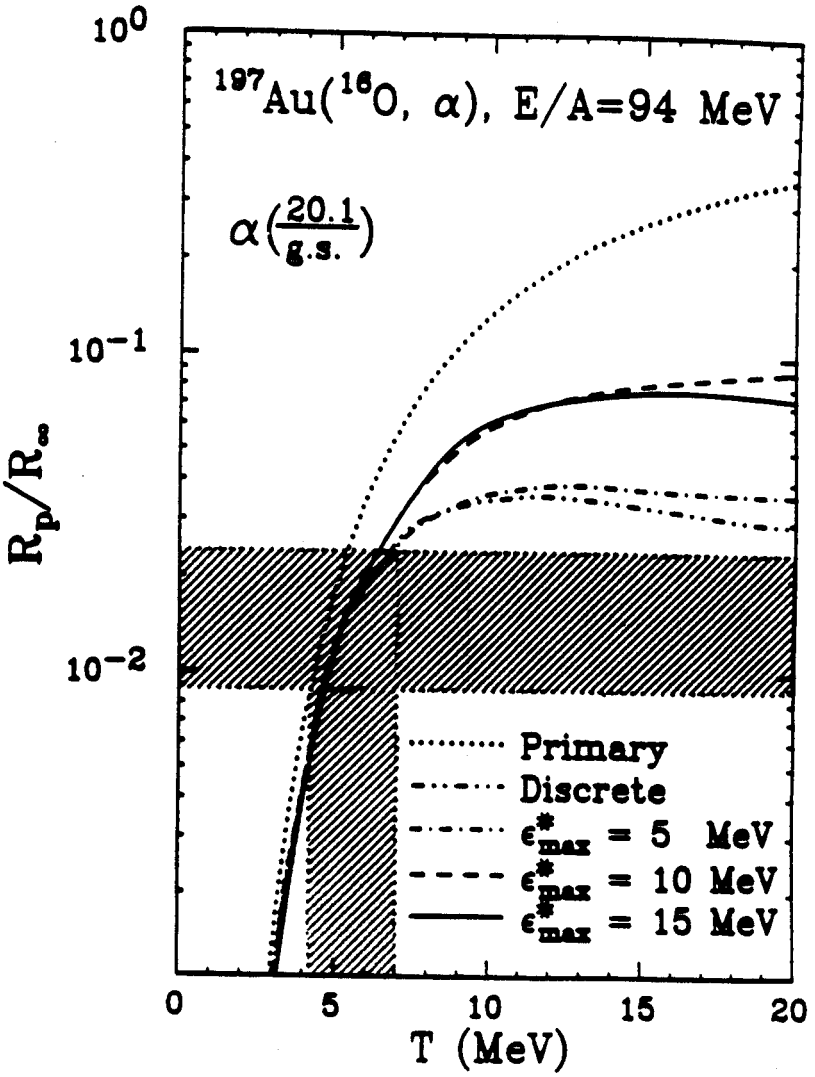

Figure IX.13 Temperature dependence of normalized population ratios, R_p/R_∞, of the ground and 20.1 MeV states in ^{4}He predicted by our calculations. The heavy dotted curve corresponds to the primary distribution; the dashed-dotted-dotted curve corresponds to feeding from known states of $Z \leq 10$ nuclei; the dashed-dotted, dashed, and the solid curves correspond to calculations using ϵ^*_{max} = 5, 10, and 15 MeV, respectively. The shaded horizontal band represents the measurement (see Chap. 7); the shaded vertical band indicates the range of emission temperatures consistent with these measurements and the present calculations.

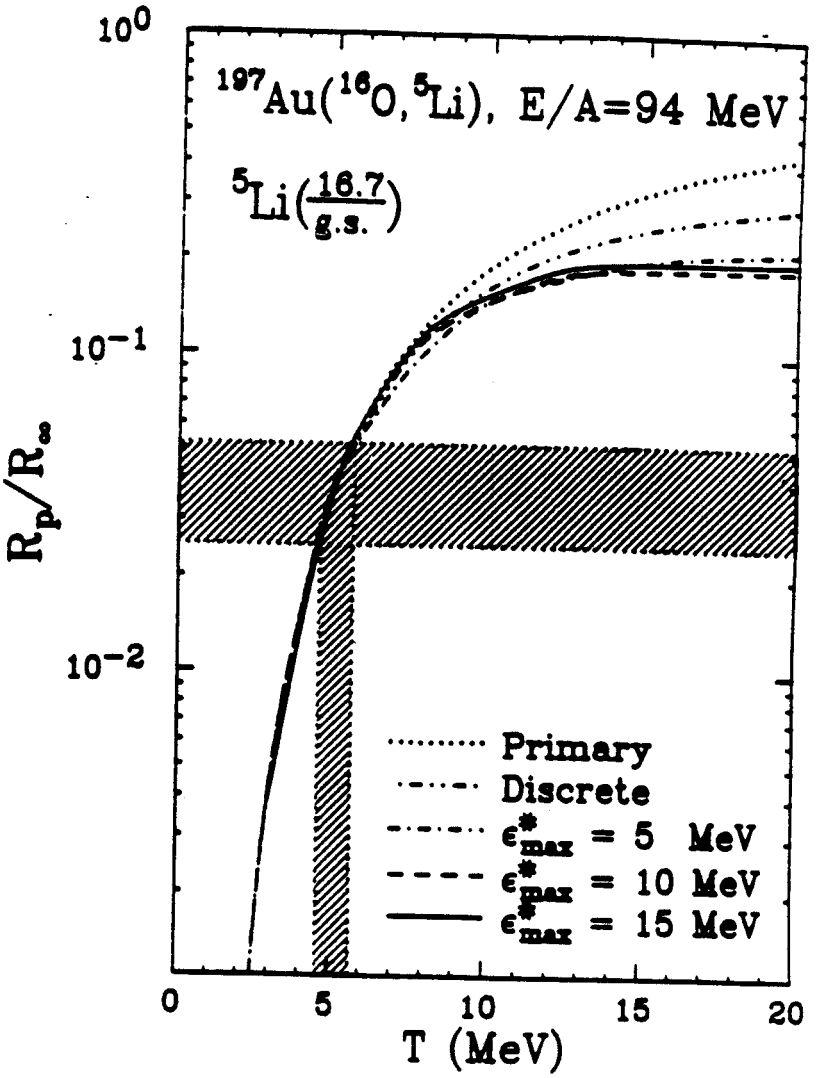

Figure IX.14 Temperature dependence of normalized population ratios, R_p/R_∞, of the ground and 16.7 MeV states in ^{5}Li predicted by our calculations. The heavy dotted curve corresponds to the primary distribution; the dashed-dotted-dotted curve corresponds to feeding from known states of $Z \leq 10$ nuclei; the dashed-dotted, dashed, and the solid curves correspond to calculations using ϵ^*_{max} = 5, 10, and 15 MeV, respectively. The shaded horizontal band represents the measurement (see Chap. 7); the shaded vertical band indicates the range of emission temperatures consistent with these measurements and the present calculations.

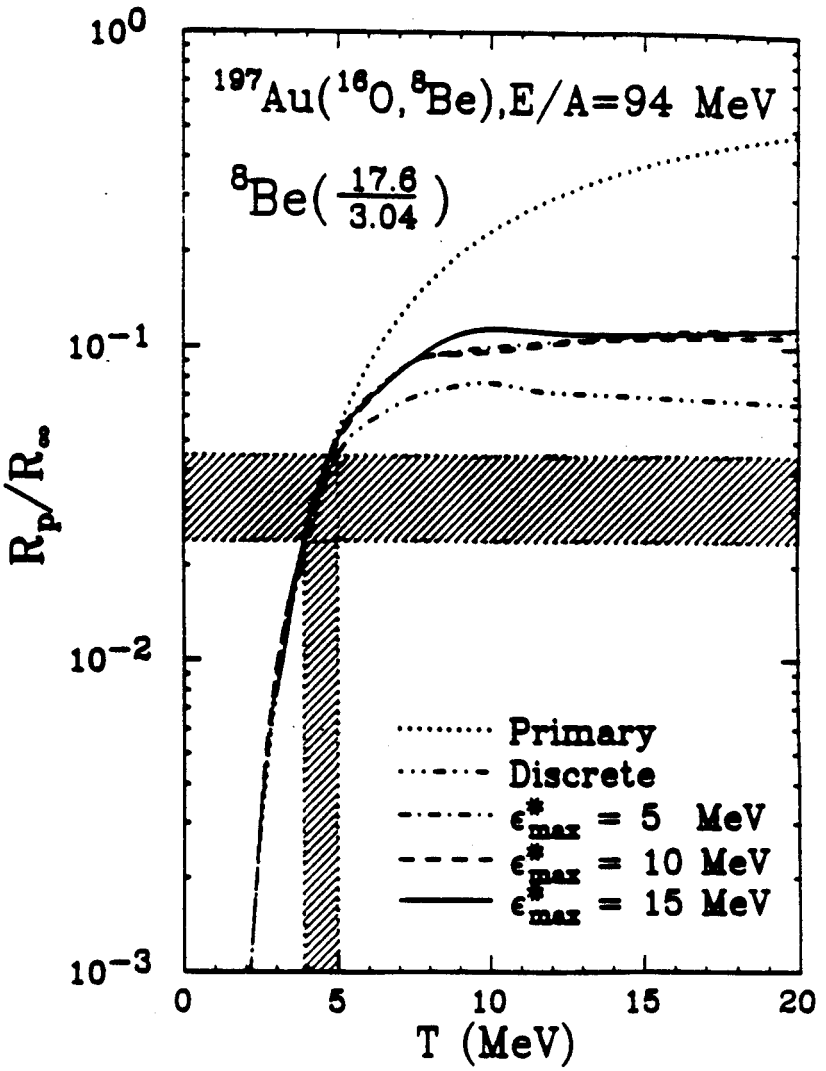

Figure IX.15 Temperature dependence of normalized population ratios, R_p/R_∞, of the 3.04 and 17.6 MeV states in ^{8}Be predicted by our calculations. The heavy dotted curve corresponds to the primary distribution; the dashed-dotted-dotted curve corresponds to feeding from known states of $Z \leq 10$ nuclei; the dashed-dotted, dashed, and the solid curves correspond to calculations using ϵ^*_{max} = 5, 10, and 15 MeV, respectively. The shaded horizontal band represents the measurement (see Chap. 7); the shaded vertical band indicates the range of emission temperatures consistent with these measurements and the present calculations.

CHAPTER 10 SUMMARY AND CONCLUSION

We have investigated single- and two-particle distributions of light nuclei emitted in the reactions $^{14}N + ^{197}Au$ at E/A=35 MeV and $^{16}O + ^{197}Au$ at E/A=94 MeV. The single particle inclusive distributions measured in these experiments can be described as a sum of three Maxwellian distributions ("moving sources"), respectively. At forward angles, the cross sections are dominated by a fast source which could be related to particle emission from projectile residues. At intermediate angles, the high energy portions of the energy spectra are dominated by an intermediate rapidity source which is generally associated with particle emission from the early nonequilibrated stages of the reaction. The kinetic temperature parameters which characterize the energy spectra of light particles emitted at intermediate rapidity, see Figure V.5, exhibit a systematic dependence upon the incident energy per nucleon of the projectile. The low energy portions of the energy spectra are dominated by a slow source related to particle emission from the later more equilibrated stages of the reaction, e.g. particle evaporation from equilibrated heavy reaction residues formed in incomplete fusion reactions.

Inclusive two-particle correlations at small relative momenta were measured at several average emission angles, Θ_{av}= 20°, 35°, and 50° for $^{14}N + ^{197}Au$ at E/A=35 MeV and at Θ_{av}=45° for $^{16}O + ^{197}Au$ at E/A=94 MeV.

For all cases investigated, the measured correlations become more pronounced at higher summed energies, E_1+E_2, of the coincident particles, indicating that more energetic particles are emitted from sources of smaller space-time extent. This energy dependence is not limited to particle emission close to the grazing angle (see Figure VIII.14) as had been surmised previously [Bond 1984]. From the zero-lifetime final state interaction model, we extracted the upper limits for the spatial dimensions of the emitting sources. For the emission of very energetic particles, the extracted source radii are smaller than the size of target nucleus, consistent with emission from the primary reaction zone. Source radii larger than the size of the target nucleus were extracted which are emitted with energies close to exit channel Coulomb barrier. These larger source dimensions could be due to increasing temporal separations between individual emission processes. Source radii extracted from the p-α, d-d, and t-t correlation functions are generally larger than those extracted from p-p or d-α correlation functions. These differences are not yet understood; they might indicate that our present understanding of two-particle correlations is still deficient.

We have compared the source radii extracted from the reactions: ^{14}N + ^{197}Au at E/A=35 MeV [Poch 1986a], ^{16}O + ^{197}Au at E/A=94 MeV, ^{40}Ar+^{197}Au at E/A=60 MeV [Poch 1987] (see Figure VI.9). For particles of a fixed total kinetic energy, the source dimensions can be ordered as $r_0(^{14}N+Au) < r_0(^{16}O+Au) < r_0(^{40}Ar+Au)$. Qualitatively, this ordering is to be expected from the relative dimensions of the geometrical regions of overlap formed for an average collision. However, it does not appear that the extracted source dimensions depend only on the size of the

initial reaction zone. Indeed, for correlations at fixed sum energy, E_1+E_2, the source dimensions also depend on the incident energy, with increasing space-time dimensions being observed at higher projectile energies. For given projectile mass, the two-proton correlations appear to primarily depend on the total kinetic energy per nucleon of the coincident particles measured in units of the projectile energy per nucleon, $(E_1+E_2)A_p/[(A_1+A_2)E_p]$, (see Figure VI.10). This suggests that scaling laws may prove useful in relating two-particle correlations measured for different reactions. However, more data are needed to establish the dependence of two-particle correlation functions on the geometrical properties of projectile and target and on incident energy. On the theoretical side, more quantitative treatments of the temporal evolution of the reaction are needed to fully exploit the information content of two-particle correlation functions.

In order to investigate dependences on specific classes of reactions, single- and two-particle distributions were measured in coincidence with two fission fragments resulting from the decay of heavy reaction residues for ^{14}N induced reaction on ^{197}Au target at E/A = 35 MeV. The coincident light particles were detected at forward angles, $\theta_{av}=20°$. Since the folding angle between two coincident fission fragments is related to the linear momentum transfer to the heavy reaction residue, one can discriminate quasi-elastic peripheral reactions from more violent fusion-like collisions by placing appropriate gates on folding angles. The effectiveness of this reaction filter was demonstrated by the rather dramatic dependence of the kinetic energy spectra on folding angle. When fission fragments are emitted with large folding angles, the energy spectra of the coincident light

particles exhibit a pronounced beam-velocity component. This component is reduced significantly when smaller folding angles (i.e. larger linear-momentum transfers to the heavy reaction residue) are selected.

Correlation functions for coincident deuterons and alpha particles exhibit a pronounced dependence on the total kinetic energy, $E_\alpha+E_d$, when they are gated by small folding angles (i.e. fusion-like collisions). This energy dependence is not observed for α-d correlation functions gated on large folding angles (i.e. quasi-elastic peripheral collisions). Furthermore, two particle correlations gated by small folding angles exhibit larger maxima than those gated by quasi-elastic peripheral collisions. Increasing contributions from the decay of excited projectile residues were argued [Bond 1984] to account for the fact that inclusive two-particle correlations become more pronounced for higher total kinetic energies of the emitted particles. Our observations show the opposite effect.

Most likely, temporal effects cannot be neglected when interpreting the magnitude of the correlation function measured in this experiment. Particles emitted from equilibrated reaction residues can be emitted at larger average time intervals than particles emitted from the early nonequilibrated stages of the reaction. Larger emission time scales will dampen the two-particle correlation functions. Particle emission from equilibrated heavy reaction residues contributes predominantly to the low energy portions of the energy spectra. Particle emission from equilibrated projectile residues can be enhanced by selecting quasi elastic peripheral reactions and detecting the emitted particles at forward angles. In both cases, reduced correlations are observed. The

selection of energetic particles emitted at larger angles or in fusion-like reactions should enhance contributions from the early-nonequilibrated stages of the reaction. For this class of reactions, the measured correlations are most pronounced and should reflect more clearly the spatial localization during the early stages of the reaction.

The relative populations of widely separated states in ^{4}He, $^{5,6}Li$, and ^{8}Be nuclei are consistent with average emission temperatures of 5 MeV, exhibiting a surprisingly small dependence on projectile energy. As shown in Figure VII.7, emission temperatures extracted in the ^{16}O+Au reaction at E/A=94 MeV are rather similar to those extracted for the reactions ^{14}N+^{197}Au at E/A=35 MeV [Chit 1986b] and ^{40}Ar+^{197}Au at E/A=60 MeV [Poch 1987]. Mean emission temperatures extracted from the relative populations of particle unbound states in ^{5}Li and ^{6}Li were found to be remarkably similar for quasi-elastic peripheral collisions and more violent fusion-like reactions.

More energetic particles could be expected to originate from the early stages of the reaction at which the excitation energy per nucleon should be highest, resulting in higher emission temperatures for parent nuclei of higher kinetic energy. For the ^{16}O+^{197}Au reaction at E/A=94 MeV, the granularity of the hodoscope was sufficient to allow the detection of the decay $^{5}Li^{*}_{16.7} \rightarrow d + {}^{3}He$ over a broad range of kinetic energies. For total kinetic energies of $E_d + E_{^3He}$ = 55-125 and 125-300 MeV, apparent emission temperatures of $T_{^5Li}$ = 4.4-5.6 and 5.0-6.0 were extracted, respectively. Thus the dependence of the emission temperature on the kinetic energy of the emitted particles is slight.

Temperatures extracted from the relative populations of states are in stark contrast to those extracted from kinetic energy spectra which exhibit a systematic dependence on projectile energy as expected for particle emission from the early reaction zone, see Figure V.5. Moreover, the distributions of relative kinetic energies between two coincident particles, detected at small relative angles in the reaction $^{16}O + ^{197}Au$ at E/A=94 MeV, indicate comparable or even higher kinetic temperatures. The relative motion of coincident particles appears, therefore, to be governed by two different "temperatures": a "chemical" emission temperature of about 5 MeV which governs the relative populations of particle unbound states and "kinetic" temperatures of $T \geq 20$ MeV which govern the distribution of kinetic energies in regions not dominated by individual resonances.

Emission temperatures extracted from the relative populations of states can have considerable uncertainties due to feeding from higher lying states. We have evaluated such uncertainties for the relative populations of widely separated states of ^{4}He, ^{5}Li, and ^{8}Be nuclei emitted in ^{16}O induced reactions on ^{197}Au at E/A=94 MeV. Previous calculations [Fiel 1987, Hahn 1987] have included the decays of known states in nuclei of charge $Z \leq 10$. In the present investigation, we have extended the range of primary fragments up to $Z \leq 20$ and included decays of high lying continuum states. Uncertainties for the unknown distribution of primary fragments were reduced by constraining the final fragment distributions (after the decays of particle unstable states) to follow the trends of element distributions measured [Troc 1986] for a similar reaction.

The predicted amount of feeding depends rather strongly upon the range of primary fragment excitation energies considered in the calculations. Yet, the relative populations of the widely separated states $^{4}He_{20.1}/^{4}He_{g.s.}$, $^{5}Li_{16.7}/^{5}Li_{g.s.}$, and $^{8}Be_{17.6}/^{8}Be_{3.04}$ are calculated to be less sensitive to details of the density of continuum states once the fragment distributions are constrained by the experimental data. Qualitatively, the present calculations confirm previous findings. The relative populations of the states in ^{4}He and ^{8}Be are predicted to be strongly perturbed by sequential feeding. For these nuclei, the relative populations of states are calculated to saturate already at rather low temperatures, $T \geq 6$ MeV. The perturbations of the two ^{5}Li states are calculated to be less severe. The relative populations of these states are predicted to saturate only at higher temperatures, $T \geq 10$ MeV. The calculated saturation values are inconsistent with the measurements for the reaction $^{16}O + ^{197}Au$ at E/A=94 MeV.

Emission temperatures of $T(^{4}He) = 4.2\text{-}7.0$ MeV, $T(^{5}Li) = 4.6\text{-}5.6$ MeV, and $T(^{8}Be) = 3.9\text{-}4.8$ MeV, extracted from the relative populations of states measured for the ^{16}O+Au reaction at E/A=94 MeV, are mutually consistent. We believe that our calculations rule out the possibility of explaining the low emission temperatures extracted from the measurements in terms of sequential feeding from primary fragments statistically emitted from a source of much higher temperature. Therefore, an explanation of these low emission temperatures will either require reaction dynamics leading to the emission of particles with large kinetic, but small internal energies or an efficient cooling by expansion of a strongly interacting source.

LIST OF REFERENCES

[AICH 1984] J. Aichelin, Phys. Rev. Lett. 52 (1984) 2340.

[AJZE 1983] F. Ajzenberg-Selove, Nucl. Phys. A392, 1 (1983).

[AJZE 1984] F. Ajzenberg-Selove, Nucl. Phys. A413, 1 (1984).

[AJZE 1985] F. Ajzenberg-Selove, Nucl. Phys. A433, 1 (1985).

[AJZE 1986a] F. Ajzenberg-Selove, Nucl. Phys. A449, 1 (1986).

[AJZE 1986b] F. Ajzenberg-Selove, Nucl. Phys. A460, 1 (1986).

[AWES 1981a] T.C. Awes, G. Poggi, C.K. Gelbke, B.B. Back, B.G. Glagola, H. Breuer, and V.E. Viola, Jr., Phys. Rev. C24 (1981) 89.

[AWES 1981b] T.C. Awes, G. Poggi, S. Saini, C.K. Gelbke, R. Legrain, and G.D. Westfall, Phys. Lett. 103B (1981) 417.

[AWES 1988] T.C. Awes, R.L. Ferguson, F.E. Obenshain, F. Plasil, G.R. Young, S.Pratt, Z. Chen, C.K. Gelbke, W.G. Lynch, J. Pochodzalla, and H.M. Xu, private communication.

[BARI 1971] I.Y. Brait and V.A. Sergeev, Soviet J. Nucl. Phys., 13 (1971) 708.

[BACK 1980] B.B. Back, K.L. Wolf, A.C. Mignerey, C.K. Gelbke, T.C. Awes, H. Breuer, V.E. Viola, Jr., and P.Dyer, Phys. Rev. C22 (1980) 1927.

[BAN 1985] S. Ban-Hao and D.H.E. Gross, Nucl. Phys. A437 (1985) 643.

[BECC 1981] F.D. Becchetti, C.A. Fields, R.S. Raymond, H.C. Bhang, and D.Overway, Phys. Rev. C24, (1981) 2401.

[BERN 1985] M.A. Bernstein, W.A. Friedman, W.G. Lynch, C.B. Chitwood, D.J. Fields, C.K. Gelbke, M.B. Tsang, T.C. Awes, R.L. Ferguson, F.E. Obenshain, F. Plasil, R.L. Robinson, and G.R. Young, Phys. Rev. Lett. 54 (1985) 402.

[BERT 1980] In D. Wilkinson (Ed.), Prog. Part. Nucl. Phys., Vol 4, Pergamon, Oxford, p. 483.

[BIRK 1983] J.R. Birkelund and J.R. Huizenga. Annu. Rev. Nucl. Sci., 33, (1983) 265.

[BOAL 1984] D.H. Boal, Phys. Rev. C30 (1984) 749.

[BOAL 1986] D.H. Boal and H. DeGuise, Phys. Rev. Lett. 57 (1986) 2901.

[BOAL 1986] D.H. Boal and J.C. Shillcock, Phys. Rev. C33 (1986) 549.

[BOND 1984] P.D. Bond and R.J. de Meijer, Phys. Rev. Lett. 52 (1984) 3201.

[BOHR 1936] N. Bohr, Nature, 137, (1936) 344.

[BROW 1956] R. Hanbury-Brown and R.Q. Twiss, Nature (London) 178 (1956) 1046.

[BROW 1984] B.A. Brown, C.R. bronk and Hodgson, J. Phys. G10 (1984) 1683.

[BLOC 1986] C.Bloch, W. Benenson, E. Kashy, D.J. Morrissey, R.A. Blue, R.M. Ronningen, and H. Utsunomiya. Phys. Rev. C34, (1986) 850.

[BLOC 1987] C. Bloch and E. Kashy, Phys. Rev. C36, (1987) 855.

[CHEN 1987a] Z. Chen, C.K. Gelbke, J. Pochodzalla, C.B. Chitwood, D.J. Fields, W.G. Lynch, and M.B. Tsang, Phys. Lett. 184, (1987)

280.

[CHEN 1987b] Z. Chen, C.K. Gelbke, J. Pochodzalla, C.B. Chitwood, D.J. Fields, W.G. Gong, W.G. Lynch, and M.B. Tsang, Nucl. Phys. A473, (1987) 564.

[CHEN 1987c] Z. Chen, C.K. Gelbke, W.G. Gong, Y.D. Kim, W.G. Lynch, M.R. Maier, J. Pochodzalla, M.B. Tsang, F. Saint-Laurent, D. Ardouin, H. Delagrange, H. Doubre, J. Kasagi, A. Kyanowski, A. Pèghaire, J. Pèter, E. Rosato, G. Bizard, F. Lefèbvres, B. Tamain, J. Quèbert, and Y.P. Viyogi, Phys. Lett. B199 (1987) 171; Phys. Rev. C36, (1987) 2297.

[CHIT 1985] C.B. Chitwood, J. Aichelin, D.H. Boal, G. Bertsch, D.J. Fields, C.K. Gelbke, W.G. Lynch, M.B. Tsang, J.C. Shillcock, T.C. Awes, R.L. Ferguson, F.E. Obenshain, F. PLasil, R.L. Robinson, and G.R. Young, Phys. Rev. Lett. 54 (1985) 302.

[CHIT 1986a] C. B. Chitwood, D.J. Fields, C.K. Gelbke, D.R. Klesch, W.G. Lynch, M.B. Tsang, T.C. Awes, R.L. Ferguson, F.E. Obenshain, F. Plasil, R.L. Robinson, and G.R. Young, Phys. Rev. C34 (1986) 858.

[CHIT 1986b] C.B. Chitwood, C.K. Gelbke, J. Pochodzalla, Z. Chen, D.J. Fields, W.G. Lynch, R. Morse, M.B. Tsang, D.H. Boal, and J.C. Shillcock, Phys. Lett. 172B (1986) 27.

[ENDT 1978] P.M. Endt and C. Van Der Leun, Nucl. Phys. A310, (1978) 1.

[EZEL 1977] C. Ezell et al. Phys. Rev. Lett. 38 (1977) 873.

[FAI 1983] G. Fai and J. Randrup, Nucl. Phys. 381, 557 (1982); Phys.

Lett., 115B, 281 (1982); Nucl. Phys. A404, (1983) 281.

[FIAR 1973] S. Fiarman and W.E. Meyerhof, Nucl. Phys. A206, (1973) 1.

[FIEL 1984] D.J. Fields, W.G. Lynch, C.B. Chitwood, C.K. Gelbke, M.B. Tsang, H. Utsunomiya, and J. Aichelin, Phys. Rev. C30 (1984) 1912.

[FIEL 1987] D.J. Fields, C.K. Gelbke, W.G. Lynch, and J. Pochodzalla, Phys. Lett. B187 (1987) 257.

[FRIE 1983] W.A. Friedman and W. G. Lynch, Phys. Rev. C28 (1983) 16, ibid. 950.

[FRIE 1988] W.A. Friedman, Phys. Rev. Lett. 60 (1988) 2125.

[GELB 1987] C.K. Gelbke and D.H. Boal, Prog. Part. and Nucl. Phys. 19, (1987) 33.

[GOLD 1960] G. Goldhaber, S. Goldhaber, W. Lee, and A. Pais, Phys. Rev. 120 (1960) 300.

[GOME 1988] J. Gomez Del Campo, private communication.

[GOSS 1979] G. Gosset, J.I. Kapusta, and G.D. Westfall, Phys. Rev. C18 (1978) 844.

[GOUL 1975] F.S. Goulding and B.G. Harvey, Annu. Rev. Nucl. Sci., 25, (1975) 167.

[GUST 1984] H.A. Gustafsson, H.H. Gutbrod, B. Kolb, H. Löhner, B. Ludewigt, A.M. Poskanzer, T. Renner, H. Riedesel, H.G. Ritter, A. Warwick, F. Weik, and H. Wieman, Phys. Rev. Lett. 53 (1984) 544.

[HAHN 1986] D. Hahn and H. Stöcker, Phys. Rev. C35, (1987) 1311.

[HAUS 1952] W. Hauser and H. Feshbach, Phys. Rev. 87, (1952) 366.

[HUAN 1963] K. Huang, Statistical Mechanics (Wiley, New York, 1963), p. 310.

[JACA 1983] B.V. Jacak, G.D. Westfall, C.K. Gelbke, L.H. Harwood, W.G. Lynch, D.K. Scott, H. Stöcker, M.B. Tsang, and T.J.M. Symons, Phys. Rev. Lett. 51 (1983) 1846.

[JENN 1986] B.K. Jennings, D.H. Boal, and J.C. Shillcock, Phys. Rev. C33 (1986) 1303.

[KAPU 1980] J.I. Kapusta, Phys. Rev. C21 (1980) 1301.

[KNOL 1979] J. Knoll, Phys. Rev. C20 (1979) 773.

[KOON 1977] S.E. Koonin, Phys. Lett. 70B (1977) 43.

[KOON 1981] S.E. Koonin and J. Randrup, Nucl. Phys. A356, (1981) 223.

[KOPY 1974a] G.I. Kopylov and M.I. Podgoretskii, Soviet J. Nucl. Phys. 18 (1974) 336.

[KOPY 1974b] G.I. Kopylov, Phys. Lett. 50B (1974) 472.

[LANE 1958] A.M. Lane and R.G. Thomas, Rev. of Mod. Phys., 30, (1958) 257.

[LENK 1986] R.J. Lenk and Pandharipande, Phys. Rev. C34, (1986) 177

[LYNC 1983] W.G. Lynch, C.B. Chitwood, M.B. Tsang, D.J. Fields, D.R. Klesch, C.K. Gelbke, G.R. Young, T.C. Awes, R.L. Ferguson, F.E. Obenshain, F. Plasil, R.L. Robinson, and A.D. Panagiotou, Phys. Rev. Lett. 51 (1983) 1850.

[MARM 1969] P. Marmier and Sheldon, Physics of Nuclei and Particles,

Vol. 1 (Academic Press, New York, 1969) p. 38.

[MEKJ 1980] A. Mekjian, Phys. Lett., B89 (1980) 177.

[MORE 1975] L.G. Morreto, Nucl. Phys. A247, (1975) 211.

[MORR 1984a] D.J. Morrissey, W. Benenson, E. Kashy, B. Sherrill, A.D. Panagiotou, R.A. Blue, R.M. Ronningen, J. van de Plicht, and H. Utsunomiya, Phys. Lett. 148B (1984) 423.

[MORR 1984b] D.J. Morrissey, W. Benenson, E. Kashy, C. Bloch, M. Lowe, R.A. Blue, R.M. Ronningen, B. Sherrill, H. Utsunomiya, and I. Kelson, Phys. Rev. C32 (1985) 877.

[MORR 1986] D.J. Morrissey, C. Bloch, W. Benenson, E. Kashy, R.A. Blue, R.M. Ronningen, and R. Aryaeinejad, Phys. Rev. C34 (1986) 761.

[MOSE 1984] U. Mosel. In A.D. Bromley (Ed.), Treatise on Heavy Ion Science, Vol.2, Plenum, New York, (1984) p. 3.

[NAGA 1984] S. Nagamiya and Gyulassy, Advances in Nuclear Physics, Vol 13, Plenum, New York, (1984) p. 201.

[POCH 1985a] J. Pochodzalla, W.A. Friedman, C.K. Gelbke, W.G. Lynch, M. Maier, D. Ardouin, H. Delagrange, H. Doubre, C. Grègoire, A. Kyanowski, W. Mittig, A. Pèghaire, J. Pèter, F. Saint-Laurent, Y.P. Viyogi, B. Zwieglinski, G. Bizard, F. Lefèbvres, B. Tamain, and J. Quèbert, Phys. Rev. Lett. 55 (1985) 177.

[POCH 1985b] J. Pochodzalla, W.A. Friedman, C.K. Gelbke, W.G. Lynch, M. Maier, D. Ardouin, H. Delagrange, H. Doubre, C. Grègoire, A. Kyanowski, W. Mittig, A. Pèghaire, J. Pèter, F. Saint-

Laurent, Y.P. Viyogi, B. Zwieglinski, G. Bizard, F. Lefèbvres, B. Tamain, and J. Quèbert, Phys. Lett. 161B (1985) 275.

[POCH 1985c] J. Pochodzalla, W.A. Friedman, C.K. Gelbke, W.G. Lynch, M. Maier, D. Ardouin, H. Delagrange, H. Doubre, C. Grègoire, A. Kyanowski, W. Mittig, A. Pèghaire, J. Pèter, F. Saint-Laurent, Y.P. Viyogi, B. Zwieglinski, G. Bizard, F. Lefèbvres, B. Tamain, J. Quèbert, Phys. Lett. 161B (1985) 256.

[POCH 1986a] J. Pochodzalla, C.B. Chitwood, D.J. Fields, C.K. Gelbke, W.G. Lynch, M.B. Tsang, D.H. Boal, and J.C. Shillcock, Phys. Lett. 174B (1986) 36.

[POCH 1986b] J. Pochodzalla, C.K. Gelbke, C.B. Chitwood, D.J. Fields, W.G. Lynch, M.B. Tsang, and W.A. Friedman, Phys. Lett. 175B (1986) 275.

[POCH 1987] J. Pochodzalla, C.K. Gelbke, W.G. Lynch, M. Maier, D. Ardouin, H. Delagrange, H. Doubre, C. Grègoire, A. Kyanowski, W. Mittig, A. Pèghaire, J. Pèter, F. Saint-Laurent, B. Zwieglinski, G. Bizard, F. Lefèbvres, B. Tamain, and J. Quèbert, Y.P. Viyogi, W.A. Friedman, and D.H. Boal, Phys. Rev. C35 (1987) 1695.

[ROPK 1982] G. Röpke, L. Münchow, and H. Schulz, Nucl. Phys. A379 (1982) 536.

[ROPK 1983] G. Röpke, Phys. Lett. 121B (1983) 223.

[ROPK 1985] G. Röpke, H. Schulz, L.N. Andronenko, A.A. Kotov, W. Neubert, and E.N. Volnin, Phys. Rev. C31 (1985) 1556.

[SAIN 1988] F. Saint-Laurent, A. Kyanowski, D. Ardouin, H. Delagrange, H. Doubre, C. Grégoire, W. Mittig, A. Péghaire, J. Péter, G. Bizard, F. Lefèbvres, B. Tamain, J. Québert, Y.P. Viyogi, J. Pochodzalla, C.K. Gelbke, W. Lynch, and M. Maier, Phys. Lett. B202, (1988) 190.

[SCHU 1982] H. Schulz, L. Münchow, G. Röpke, and M. Schmidt, Phys. Lett. 199B (1982) 12.

[SCHU 1983] H. Schulz, G. Röpke, K.K. Gudima, and V.D. Toneev, Phys. Lett. 124B (1983) 458.

[SATO 1980] H. Sato and K. Yazaki, in "High-Energy Nuclear Interactions and Properties of Dense Nuclear Matter", K. Nakai and A.S. Goldhaber, eds., p. 340.

[SCHL 1987] T.J. Schlagel, and V.R. Pandharipande, Phys. ReV. C36, (1987) 162.

[SCHR 1984] W.U. Schroder, and J.R. Huizenga (1984). In A.D. Bromley (Ed.) Treatise on Heavy Ion Science, Vol. 2, Plenum, New York, p. 115.

[SHUR 1973] E.V. Shuryak, Phys. Lett. 44B (1973) 387.

[SHYA 1984] R. Shyam and J. Knoll, Nucl. Phys. A426 (1984) 606; Phys. Lett. 136B (1984) 221; Erratum (1986), unpublished.

[SIEM 1979] P.J. Siemens, and J.O. Rasmussen, Phys. Rev. Lett. 42 (1979) 880.

[SIKK 1962] T. Sikkeland, E.L. Haines, and V.E. Viola, Jr., Phys. Rev. 125 (1962) 1350.

[STOC 1981] H. Stocker, A.A. Ogloblin, and W. Greiner, Z. Phys. A313 (1981) 259.

[STOC 1986] R. Stock, Physics Reports, 135 (1986) 259.

[STOK 1977] R.G. Stokstad, Proceedings of the Topical Conference on Heavy-Ion Collisions, held at Fall Creek Falls State Park, Tennessee, June 13-17, 1977, p. 22.

[TAYL 1951] C.J. Taylor, W.K. Jentschke, M.E. Remley, F.S. Eby, and P.G. Kruger, Phys. Rev. 84 (1951) 1034.

[TSAN 1987] M.B. Tsang, C.B. Chitwood, D.J. Fields, C.K. Gelbke, D.R. Klesch, W.G. Lynch, K. Kwiatkowski, and V.E. Viola, Jr., Phys. Rev. Lett. 52 (1984) 1967.

[TROC 1986] R. Trockel, K.D. Hildenbrand, U.Lynen, W.F.J. Müller, H.J. Rabe, H. Sann, H.Stelzer, W. Trautmann, R. Wada, N. Brummund, R. Glasow, K.H. Kampert, R. Santo, D. Plete, J. Pochodzalla, and E. Echert, Hadronic Matter in Collision, edit by P. Carruthers and D. Strottman, World Scientific, Singapore 1986, p. 291.

[WEIS 1937] V.F. Weisskopf, Phys. Rev., 52 (1937) 295.

[WEST 1979] G.D. Westfall, J. Gosset, P.J. Johansen, A.M. Poskanzer, W.G. Meyer, H.H. Gutbrod, A. Sandoval, and R. Stock, Phys. Rev. Lett. 37 (1976) 1202.

[WEST 1982] G.D. Westfall, B.V. Jacak, N. Anantaraman, M.W. Curtin, G.M. Crawley, C.K. Gelbke, B. Hasselquist, W.G. Lynch, D.K. Scott, M.B. Tsang, M.J. Murphy, T.J.M. Symons, R. Legrain, and T.J. Majors, Phys. Lett. 116B (1982) 118.

[WAPS 1985] A.H. Wapstra and G. Audi, Nucl. Phys. A432, (1985) 1.

[XU 1986] H.M. Xu, D.J. Fields, W.G. Lynch, M.B. Tsang, C.K. Gelbke, M.R. Maier, D.J. Morrissey, J. Pochodzalla, D.G. Sarantites, L.G. Sobotka, M.L. Halbert, D.C. Hensley, D.

Hahn, and H. Stöcker, Phys. Lett. 182B (1986) 155.

[YANO 1978] F.B. Yano and S.E. Koonin, Phys. Lett. 78B (1978) 556.

[ZARB 1981] F. Zarbakhsh, A.L. Sagle, F. Brochard, T.A. Mulera, V. Perez-Mendez, R. Talaga, I. Tanihata, J.B. Carroll, K.S. Ganezer, G. Igo, J. Oostens, D. Woodard, and R. Sutter, Phys. Rev. Lett. 46 (1981) 1268.